University of Crete

School of Sciences

Department of Materials Science and Technology

Master Thesis

3D Mechanical Metamaterials

Stavros Skrepetos

Supervisors: Dr. M. Farsari, Dr. A. Ranella

Co – Supervisor: Prof. K. Velonia

Heraklion, Crete

December 2023

Table of Contents

Περίληψη

Η μελέτη αυτή αναδεικνύει την ενσωμάτωση των μετα-υλικών στη μηχανολογική μηχανική, εκμεταλλευόμενη την εμπειρογνωμοσύνη από φυσικές επιστήμες, υπολογιστική μοντελοποίηση, και μηχανική βιολογία. Τα μηχανικά μετα-υλικά προσφέρουν μοναδικά πλεονεκτήματα για τον έλεγχο του μηχανικού περιβάλλοντος των κυττάρων και των ιστών, συμπεριλαμβανομένης της δημιουργίας εξειδικευμένων κυτταρικών δομών και ιδιοτήτων.

Ο κύριος στόχος ήταν η σχεδίαση σφαιρικών μηχανικών μετα-υλικών με ακρίβεια και σπάνια αυξητική συμπεριφορά, που επιτυγχάνεται μέσω της αλγοριθμικής μηχανικής με τη χρήση του λογισμικού Hyperganic. Οι σφαίρες κατασκευάστηκαν με υψηλή ακρίβεια χρησιμοποιώντας προηγμένη εκτύπωση 3D και χαρακτηρίστηκαν οπτικά μέσω σάρωσης ηλεκτρονικού μικροσκοπίου (SEM).

Η πολυ-φωτονική λιθογραφία επέτρεψε την κατασκευή περίπλοκων δομών στη μικρο-κλίμακα, ειδικά την κατασκευή σφαιρικών δομών διαμέτρου 400 μm. Αυτοί τα ικριώματα υπόσχονται να υποστηρίξουν την ανάπτυξη κυττάρων χωρίς να θέτουν σε κίνδυνο την ζωτικότητά τους, καθιστώντας τα χρήσιμα για τη μηχανολογική μηχανική.

Ο χαρακτηρισμός περιλάμβανε αριθμητικές προσομοιώσεις χρησιμοποιώντας τα ANSYS και SolidWorks, καθώς και μηχανικές δοκιμές με το MicroTester LT για τον υπολογισμό βασικών ιδιοτήτων. Τα μεσεγχυματικά βλαστοκύτταρα καλλιεργήθηκαν στα ικριώματα και αξιολογήθηκαν κατά τη διάρκεια πολλαπλών ημερών. Η ακριβής 3D ανάλυση έγινε δυνατή μέσω ενός συνεστιακού μικροσκοπίου, επιτρέποντας μια βαθιά κατανόηση αυτών των καινοτόμων λύσεων στη μηχανολογική μηχανική βασισμένες σε μετα-υλικά για τη μηχανική ιστών.

Abstract

This study highlights the integration of metamaterials into tissue engineering, leveraging expertise from physical sciences, computational modeling, and mechanical biology. Mechanical metamaterials offer unique advantages for controlling the mechanical environment of cells and tissues, including the creation of specialized cellular structures and properties.

The primary objective was to design precise spherical mechanical metamaterials with rare auxetic behavior, achieved through algorithmic engineering facilitated by the Hyperganic software. The spheres were fabricated with high precision using advanced 3D printing and optically characterized through scanning electron microscopy (SEM).

Multi – Photon lithography enabled the construction of intricate microscale structures, particularly the fabrication of 400 μm-diameter spherical scaffolds. These scaffolds are promising for supporting cell growth without compromising viability, making them valuable for tissue engineering.

Characterization involved numerical simulations using ANSYS and SolidWorks and mechanical testing with the MicroTester LT to calculate key properties. Mesenchymal stem cells were seeded on the scaffolds and assessed over multiple days. Precise 3D analysis was made possible through a confocal microscope, allowing a deep understanding of these innovative metamaterial-based tissue engineering solutions.

1. Introduction

1.1 Motivation

The term "metamaterials" is derived from the Greek word "μετα," meaning "beyond," and the word "materials." Metamaterials are synthetic materials that go beyond the properties of natural materials. They can be engineered and tuned in various ways to achieve specific and desired results. The most frequently explored categories of metamaterials include mechanical, electromagnetic and acoustic metamaterials. These are used to manipulate mechanical properties light and sound, respectively, in innovative ways [1]. While metamaterials drive innovation in materials science, it is worth noting that their applications extend beyond this field. Mechanical metamaterials find valuable applications in the medical field.

In 2014, a study found that with approximately 20,400 practicing orthopedists, the annual expenditure on orthopedic surgery in the United States was estimated to be $8.2 billion. Orthopedic spending constitutes a substantial portion of the nation's healthcare expenditure [2].

Following surgery, rehabilitation is often required to help patients gradually return to their preoperative daily life. However, the cost of rehabilitation is not the sole financial burden for the

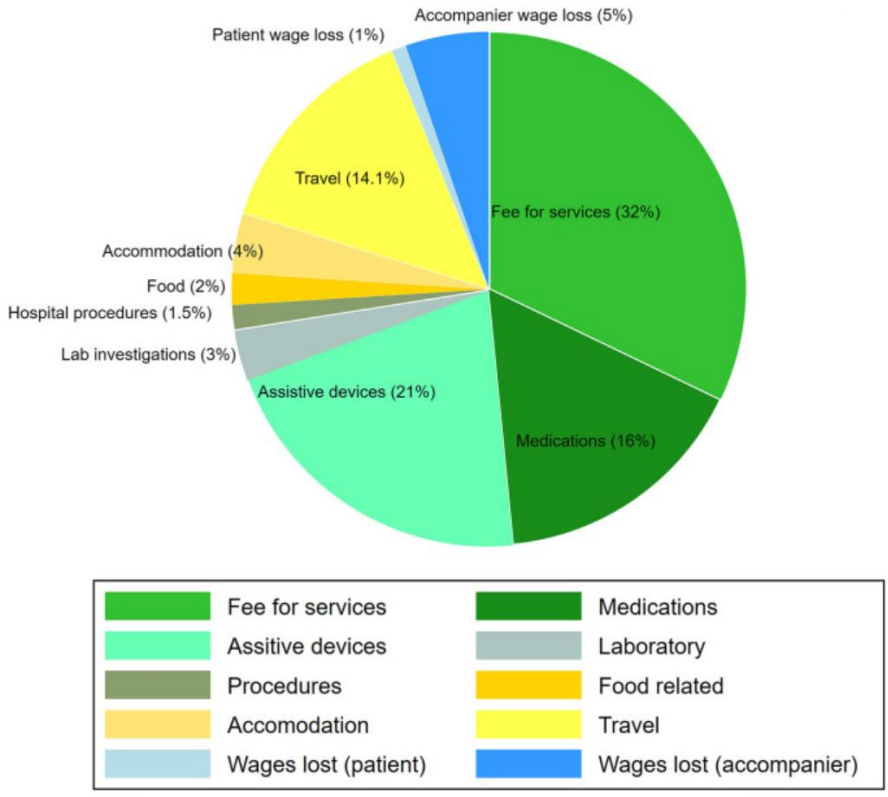

Figure 1: A pie chart of the expenses of a rehabilitation[3].

patient. A study conducted by Malik et al. [3] indicates that the true cost of knee arthroplasty rehabilitation impacts not only the patient but also their entire family. This financial impact extends to expenses such as medications, assistive devices, travel costs, wage loss for accompanying family members, and other related expenditures.

In recent decades, mechanical metamaterials have gained increasing popularity as a promising avenue for addressing challenges in tissue engineering applications, primarily due to their unique mechanical properties. The growing research interest and the pressing demands from the medical field have contributed to the rising fame of mechanical metamaterials. While there are already some metamaterials utilized in medical procedures, there remains a substantial demand for injectable mechanical metamaterials that could serve as complementary solutions to existing methods. This gap in the field represents an opportunity for the development of novel mechanical metamaterials that can enhance and expand the range of available medical interventions.

1.2 State of the art

Metamaterials, like everyday materials, are assembled from the fundamental constituents known as atoms. However, in common materials, the specific arrangement of these atoms gives rise to the material's inherent characteristics and properties. In the case of metamaterials, the design of individual meta-atoms and their specific geometric arrangement can impart extraordinary and unique properties to the complex system, properties that are typically impossible to find in naturally occurring materials. This is achieved through the periodic alignment of meta-atoms, which results in novel behaviors. A similar principle applies to mechanical metamaterials.

Mechanical metamaterials provide an exciting avenue for extending the range of mechanical signals that cells experience in a highly reproducible manner. As a result, they can be harnessed to create advanced scaffolds that allow for precise control over the biological responses of cells and tissues. This has given rise to a novel concept known as "meta-biomaterials," which denotes mechanical metamaterials with biomimetic properties seldom encountered in traditional porous biomaterials [4]. These meta-biomaterials open up exciting possibilities for tissue engineering and other biomedical applications.

These special metamaterials have been intentionally designed to exhibit paradoxical physical phenomena [5]. Notably, some of them possess a negative Poisson's ratio, as demonstrated by Wagener et al. using a technique called two-photon polymerization [6]. This class of materials, known as metamaterials, was first introduced in 1998 by Harris et al. as porous implants [7]. Metamaterials encompass biomimetic materials inspired by natural structures.

Mechanical metamaterials have revolutionized the design of functional tissue scaffolds, showing great potential in the fields of bone tissue regeneration and orthopedic implants [8]. They are also

characterized by having a high surface-to-volume ratio [9]. Achieving auxetic properties, which are unusual in nature, is made possible by designing specific microstructured architectures and manufacturing them using various methods such as Additive Manufacturing (AM). This innovative approach was initially proposed by Critchley et al. [10], leading to the creation of auxetic foams that could be customized and fabricated with stability and homogeneity, eliminating random cell orientation.

One such structure, known as the "bowtie" auxetic scaffold, evolved from the hexagonal honeycomb design by altering the internal angles of the unit cell to produce negative values of Poisson's Ratio. The underlying microstructure plays a crucial role in shaping the physical properties of these meta-biomaterials. For instance, natural materials like wood have been used as inspiration to create substitutes for hard tissues [11]. Although metamaterials have been suggested to enhance implants and tissue scaffolds for various organs, the scalability of current production methods has limited the application of innovative microarchitectures in practical prototypes [12].

The development of the shuriken, a star-inspired structure, represents a novel approach to auxetic mechanical metamaterials[13]. This innovative structure has spurred further research and exploration into its properties. Various designs have created by altering the inner angles of this 4-point star-based structure to investigate the extent to which these angle variations can influence and modify its auxetic properties. This experimentation is essential for a deeper understanding of how the shuriken and similar structures can be tailored to meet specific engineering or biomedical requirements.

Injectable meta-biomaterials represent an innovative approach to metamaterials, particularly in the field of regenerative medicine. Their primary aim is to facilitate in vivo shaping, followed by the induction of three-dimensional (3D) tissue formation. What makes these materials particularly exciting is their ability to reversibly change stiffness during deformation, effectively matching the mechanical properties of native tissues over a wide range of deformation amplitudes. This property holds significant promise for a variety of applications, especially in tissue engineering and the development of biomedical implants[14].

Indeed, there has been considerable research and development in the realms of spherical metamaterials, auxetic mechanical metamaterials and injectable metamaterials. However, the focus of this work is to introduce a novel concept: the creation of injectable auxetic mechanical metamaterials. This innovative approach aims to bring together multiple classifications of metamaterials, totaling more than three, with the ultimate goal of advancing tissue engineering applications. By combining these different metamaterial properties, this work aspires to open new avenues for tissue engineering and regenerative medicine, potentially leading to groundbreaking applications and solutions in the field.

1.3 Thesis Outline

- Chapter 1 introduces the motivation behind this work. Additionally, it outlines the structure and content of this thesis.
- Chapter 2 delves into the theoretical foundations of Multi – Photon lithography, exploring the theory of multi-photon absorption. Additionally, it provides insight into mechanical metamaterials, prior work related to auxetic and spherical metamaterials, and discusses light-based fabrication techniques for mechanical metamaterials. The chapter also features a brief discussion on Tissue Engineering, Regenerative Medicine, Immunoengineering, and biomaterials.
- Chapter 3 outlines the materials and methods used to carry out this work. This includes details about the hybrid materials, the homemade Multi – Photon polymerization setup, the SLA printer and its operating procedures, the design and theoretical, mechanical, and optical characterization of the spheres, as well as the techniques employed in cell studies.
- Chapter 4 will encompass the presentation of results obtained from theoretical simulations, scaffold design, SLA and Two-Photon Polymerization fabrication, as well as mechanical testing. Furthermore, it will incorporate results obtained from the spheres cultured with cells.
- Chapter 5 will serve as the concluding section of this work, providing a summary of the findings and proposing directions for future research.
- In Chapter 6, you will find a comprehensive list of all the references that were utilized in this work.

2. Theoretical Background

2.1 Light Based Fabrication Methods

One of the most effective approaches to producing intricate mechanical metamaterials involves employing various light-assisted methods. These methods operate by solidifying photopolymerizable materials using precise beams of focused light while these materials retain a liquid-like state. The specific procedures can vary based on factors such as the wavelength of light, the method of light excitation, and the process of material application. To achieve this, tools like galvanometers or micro-mirror devices are harnessed to concentrate and direct the generated light, with options ranging from laser beams to collimated light sources for light generation.

The fabrication process of these materials is then initiated through techniques like vat polymerization, powder-bed fusion, or directed energy deposition. For polymers and plastics, advanced manufacturing technologies such as Stereolithography (SLA) and Digital Light Processing (DLP)-based SLA have been proposed. The cutting-edge methodologies currently in use are comprehensively summarized in Figure 2[15–19].

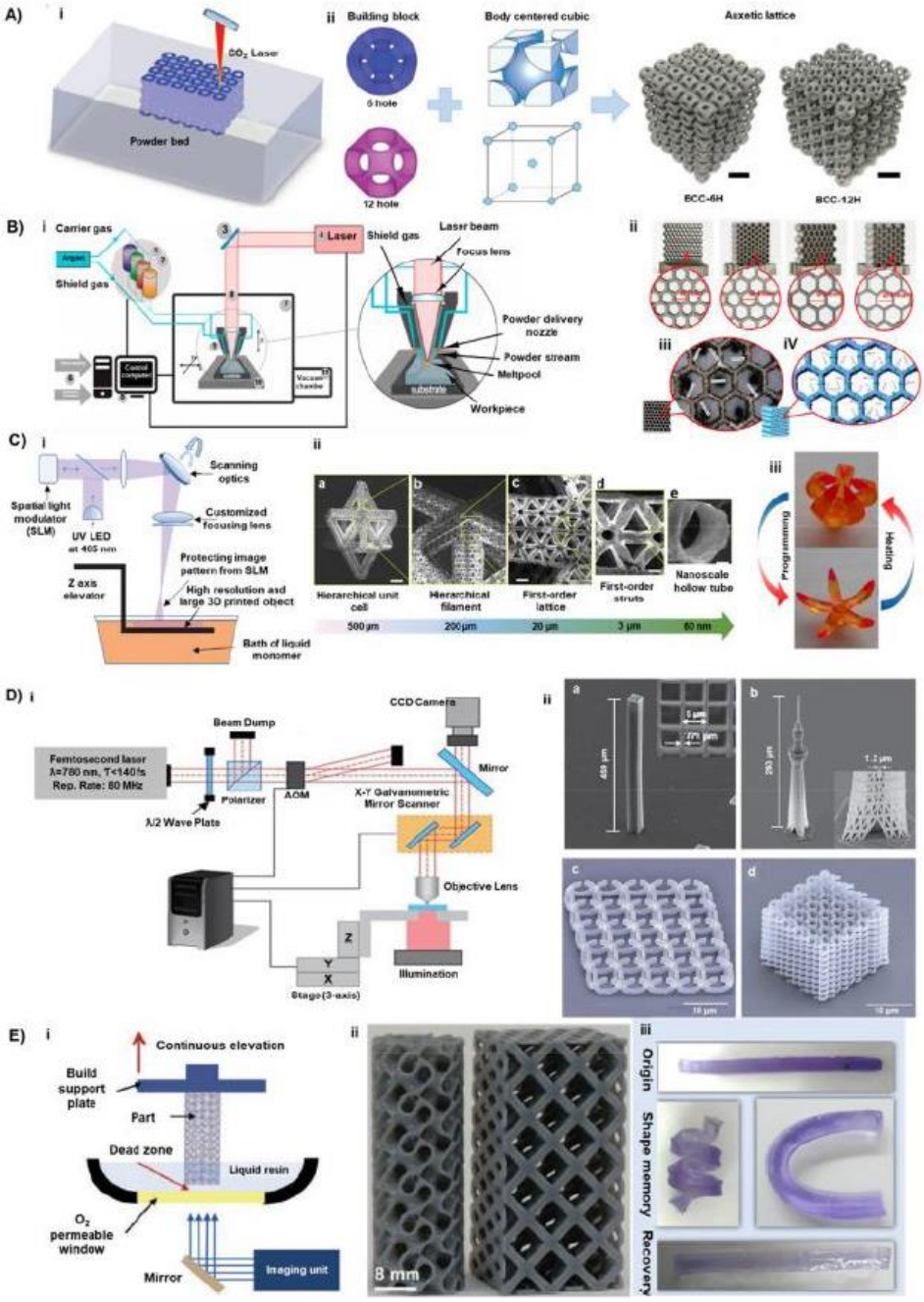

Figure 2: A visual depiction of the current utilization of light-assisted additive manufacturing methods in the creation of metamaterials. A) Demonstrates the customary construction platform for Selective Laser Sintering (SLS) and portrays the design concepts of BCC-6H and BCC-12H scaffolds[87]. B) Offers an insight into the LENS system, including (ii) distinct variants of thin-walled honeycomb structures made from Ti6Al4V with varying unit cell sizes, (iii) showcasing the utilization of optical microscopy, and (iv) representing a 3D model. C) Provides a schematic representation of large area projection micro-stereolithography, with (ii) displaying scanning electron microscopy images that elucidate the cross-sectional breakdown of the multi-scale metamaterial unit cell's structural hierarchy [61], and (iii) demonstrating the transformation between the printed shape and the temporary shape of multi-material shape memory grippers [88]. D) (i) Depicts the schematic illustration of the Two Photon Absorption (TPA) technique, and (ii) presents scanning electron micrographs of a 6 × 6 grid structure known as "Tokyo Skytree," generated through TPA using a 100× microscope objective [89], (c,d) showcases a 3D split-ring metamaterial structure manufactured using a metal-binding hybrid polymer composite. The figure has been adapted from the source[89].

2.1.1 Single Photon Polymerisation

Single – Photon Polymerization (SPP) is a cutting-edge 3D printing technique used in advanced additive manufacturing. Unlike traditional 3D printing methods that use lasers or other light sources to create 3D structures, SPP relies on the precise control of a single focused laser beam, typically operating in the UV or visible light spectrum. The process involves the photoinitiation of a liquid resin using a focused photon beam, causing the resin to solidify and form a 3D object layer by layer. SPP offers advantages such as high precision, sub-micron resolution, and the ability to produce intricate, complex structures[20,21].

2.1.2 Multi – Photon Lithography

Multi – photon lithography (MPL), also known as direct laser lithography or direct laser writing, is a 3D printing technique which enables the direct writing of computer aided designed (CAD) structures. The final result is achieved by irradiating a photosensitive material [22–24]. Essentially, it is a method for producing elements on a microscale or nanoscale that does not require the use of a complex optical system or photomask. The primary feature of MPL lies in its capability to generate 3D structures in a single step, a distinct advantage not shared by other lithography methods. This approach is based on the process of multiphoton absorption in the laser's wavelength. This technique was first demonstrated in 1997 [25], and it was used by the photonics community for the fabrication of 3D photonic crystals and nano – photonic devices [26–29]. Today, it is used in many different fields such as microfluidics [30], biomedical implants [31,32], complex 3D scaffolds for cell cultures and tissue engineering [33–38], micro – optical components [39,40].

2.1.3 Multi – Photon Absorption

Two – photon polymerization (TPP), which is a result of two – photon absorption (TPA), can occur when a femtosecond laser beam with an ultrashort pulse duration is focused within a photosensitive material. The simultaneous absorption of two photons by the same molecule was first theoretically analyzed in the 1930s by Göppert-Mayer [41]. The difference between two – photon and single – photon absorption is that the same electronic excitation can be achieved by absorbing two photons instead of one[42]. In this case, the sum of the energies of these two photons is equal to the energy of one photon. This first excited state has a well-defined lifetime and is populated by the first absorbed photon. Subsequently, a second photon is absorbed, as illustrated in Figure 3, and in the other mechanism. In this alternative mechanism, there is no real intermediate state, but rather a virtual intermediate state is formed through the interaction of the absorbing species with the first

photon. In the case of single-photon absorption (Figure 3.a), the absorbing species undergoes a transition from the ground state (S0) to an excited state (S1) when it absorbs the energy of a single photon. In contrast, in the case of Two – Photon Absorption (TPA), two photons, each carrying half the energy required to bridge the gap between the two energy levels (i.e., hv/2), collectively facilitate the electron transition. Usually, the energy difference between the initial and excited states corresponds to ultraviolet (UV) radiation energy. The required energy can be achieved by summing up the energies of two photons, typically in the near – infrared (NIR) range.

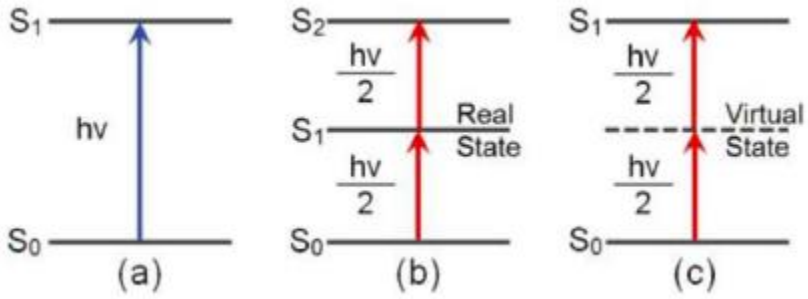

Figure 3: Schematic representation of the various excitation methods: a) Single photon excitation, b) Two – photon sequential excitation, and c) Two – photon simultaneous excitation.

2.1.4 Radical Polymerisation

In the initial stage of initiation, the initiator decomposes and yields two radicals. In the second stage, the free radicals react with monomer molecules, initiating polymerization. We add a monomer molecule to the initial radical, creating a radical chain.

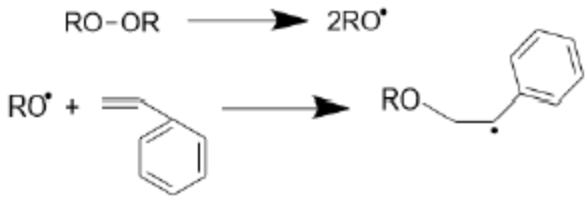

Figure 4: Initiation of free radical polymerisation.

As the process progresses, the polymer chain grows through successive addition of monomer molecules to the active center.

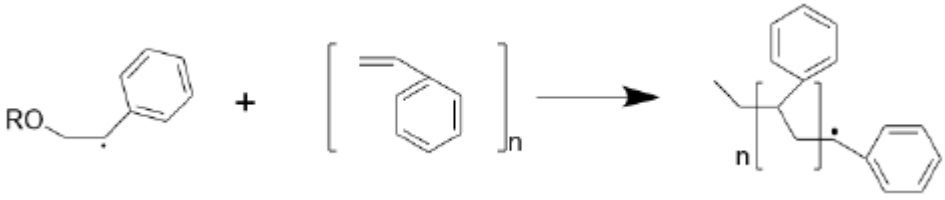

Figure 5: Propagation of free radical polymerisation.

Polymer chain growth stops at termination. This can occur in two ways. In termination by coupling, two growing polymer chains combine to form a polymer molecule.

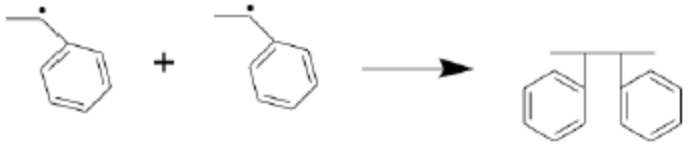

Figure 6: Termination by combination.

In termination by disproportionation, a hydrogen atom is removed from one growing polymer chain and attaches to another.

Figure 7: Termination by differentiation.

2.1.5 Materials employed

Over the years, numerous materials have been employed globally by various research groups for Multi-Photon Lithography (MPL). Some of these materials are specifically tailored for this purpose. While there may be variations, the fundamental constituents of these materials remain consistent: (i) a blend of monomers and oligomers that cross-link to enable the creation of intricate 3D structures, and (ii) a photoinitiator, a molecule designed to simultaneously absorb two photons from incident light, triggering the formation of active species and eventually promoting polymerization[43,44]. Broadly, two major categories find use in MPL. The first category encompasses organic photopolymers, such as acrylates, hydrogels, and epoxy, among others. The second category encompasses hybrid materials, which can be adapted for diverse applications, ranging from metallic-containing materials to inorganic dielectric materials and light-emitting materials. Hybrid materials are favored for their synthesis. In particular, the organic component allows for the tuning of mechanical properties, the control of porosity, and the introduction of additional physical or biological characteristics to the material. Meanwhile, the inorganic component enhances the material's thermal and mechanical stability[45].

2.2 Metamaterials

Metamaterials are artificial materials that possess specific mechanical properties that are not commonly found in nature [46]. The term "mechanical meta-materials" refers to materials whose mechanical properties are more influenced by their geometry rather than their composition [47].

Similar to conventional materials, which are periodic arrangements of atoms, meta-materials exhibit the same characteristic but with meta – atoms. The shape, geometry, size, and orientation define the properties of meta-materials. Mechanical meta-materials can be utilized in a wide range of applications, including medicine, biology [48–51], electronics [52–58]infrastructure projects, and aerospace engineering [59]. They are ideal for structural reinforcement of buildings and seismic applications [60], thanks to their high strength and ability to absorb vibrations [61]. Due to their fragile and intricate architecture, often resembling bones or other body parts, they are suitable for applications in orthopedics and tissue engineering [62,63]. Some of the characteristics of the structures that make up the mechanical metamaterials include the elimination of shear modulus (pentamode) [64–66], negative compressibility [67–69], negative Poisson's ratio (auxetic), and finally, strong-lightweight materials [19,70,71].

2.2.1 Auxetic Metamaterials

Evans created the term Auxetic in 1991 [72], taken from the Greek word 'Auxetikos' (that which tends to increase) for materials that exceed negative Poisson's Ratio. When subjected to a force, they become denser perpendicular to that force. This behavior is a result of their specific internal structure and the way they deform when a force of magnitude N is applied along a single axis.

Auxetic materials can be molecules, crystals, or specific macroscopic structures. Such materials and structures are expected to possess mechanical properties such as high energy absorption and fracture resistance. Auxetics could find applications as body protectors, protective packaging materials, protective gear for joints and knees, and materials for absorbing strong vibrations [73–77]. Due to their negative Poisson's ratios, they are also used as stents [78–82].

2.2.2 Spherical Metamaterials

A spherical metamaterial can be designed by any already known metamaterial by reproducing its unit cell in a spherical orientation.

In engineering, there is a growing interest in spherical metamaterials due to their promising potential in various applications, such as drug delivery [83], material synthesis [84], optical devices [85], and sensors [86]. Subsequently, several studies have expanded the understanding of Jitterbug-like motion (rotations at the vertices) using polyhedral transformations [87–90]. Jitterbug-like motion

refers to a type of movement or oscillation that resembles the jittery, irregular, and unpredictable motion of a jitterbug dance. This term is often used to describe erratic or chaotic movements in various contexts, such as in physics or biology.

However, a limitation for practical use in these configurations is the localized deformation at the vertices of the polyhedra, which necessitates a significant number of hinges and rotating elements to achieve the desired motion[91].

Furthermore, spherical metamaterials has been used also in phononic crystals [92], phononic bandgaps [93,94] and self–assembled superclusters [95].

Motivated by the possibilities of enhanced motion and deformation of structures, has been investigated buckling as a potential gating mechanism for structured spherical shells. The shells are designed with two patterns: a well-known re-entrant design called "Bowtie" and a novel design called "Shuriken".

2.3 Tissue Engineering, Regenerative Medicine and Immunoengineering

Tissue engineering is an interdisciplinary field governed by the principles of both engineering and the life sciences. Its goal is to produce biological substitutes that replace, support, or enhance the functionality of biological tissues or entire organs. It is an application of biomedical engineering that combines cells, mechanics, material fabrication methods, and suitable biochemical and physicochemical variables to preserve, support, enhance, or replace various types of biological tissues. Tissue engineering also encompasses the use of cells loaded onto structures to cultivate sustainable tissue varieties for medical applications. The possibilities of applications that involve cells and structures to host their growth are boundless.

Furthermore, tissue engineering can be described as "understanding tissue regeneration principles and applying functional tissue replacements to clinical applications" [96]. Regenerative medicine, a sector within mainstream medicine, develops techniques for regenerating, repairing, or replacing damaged or deceased cells, organs, or tissues. Regenerative medicine encompasses the development and use of therapeutic stem cells, immunology, tissue engineering, and the production of artificial organs [97].

The immune system comprises organs, tissues, and biological mechanisms responsible for the body's defense. The most crucial are the bone marrow and the thymus gland, as they are where immune cells are generated and developed. Notable among these cells are B and T lymphocytes, monocytes/macrophages, dendritic cells, neutrophils, eosinophils, and basophils [98,99].

Immunoengineering is an emerging branch that applies engineering practices and principles to explore and shape the immune system. It could revolutionize applications in tissue engineering, drug delivery, and even medical devices. Immunoengineering introduces new tools to biomedicine, discovering and creating novel safe approaches to treat various diseases, from cancer to type 1 diabetes and autoimmune disorders [100,101]. A part of Immunoengineering experiments involves the use of scaffolds and cells to study their responses.

2.3.1 Biomaterials

All living organisms possess the inherent capability of regeneration, which is orchestrated by molecular processes under the guidance of gene expression, governing renewal, restoration, and growth. The strategy that combines the body's regenerative potential with engineered biomaterials is known as in situ tissue regeneration, initially proposed by Langer and Vacanti in 1993 [102]. To enhance cell growth, novel protocols have been devised for isolating and culturing cells in vitro, seeding them onto a synthetic scaffold, and subsequently reintroducing them into the body.

Two fundamental techniques for tissue regeneration exist: ex vivo and in situ. The ex vivo approach employs a scaffold to introduce cells and biomolecules that will eventually be transplanted into the body. However, this method presents drawbacks like challenging culture conditions, limited grafting efficiency, donor site complications, and notably, a high risk of immune response. Conversely, the in situ technique capitalizes on the body's innate regenerative abilities, bypassing the need for ex vivo cell manipulation.

In the realm of in situ tissue regeneration, a spectrum of scaffold types is employed, including monolithic, microporous, nanoparticles, fibrous, hydrogels, and 3D-printed scaffolds. These scaffolds are crafted from diverse biomaterials such as polymers, ceramics, metals, and composites. The biophysical attributes of biomaterials, encompassing stiffness, structure, topography, and degradation, can modulate local tissue microenvironments through intercellular and intracellular signaling [103]. These changes in microenvironment include temperature or pH fluctuations, regulation of enzymes, ions, radical species, and cells.

The stiffness of the matrix influences stem cell adhesion, distribution, and fate [104,105]. For instance, stiffer surfaces prompt bone marrow cells to adhere and spread, directing stem cells toward osteogenic differentiation, whereas a softer matrix induces round-shaped cell morphology, promoting chondrogenic differentiation. Scaffold porosity is equally critical, dictating cellular infiltration; interconnected pore networks expedite the transport of oxygen, nutrients, and waste products. Porosity has also been linked to scaffold vascularization, promoting angiogenesis [106]. Similarly, surface topologies, such as patterned surfaces, can either encourage or inhibit cell adhesion and fate [107]. In most cases, in situ degradation of biomaterials is preferred for tissue

regeneration, with degradation rates aligning closely with tissue generation rates to facilitate optimal tissue growth. Many biomaterials can be degraded by cell enzymes like collagen or gelatin, facilitating tissue remodeling and deposition. Importantly, scaffold biophysical cues must closely match those of native tissue to avoid suboptimal healing, reduced functionality of regenerated tissue, implant instability, and tissue loss.

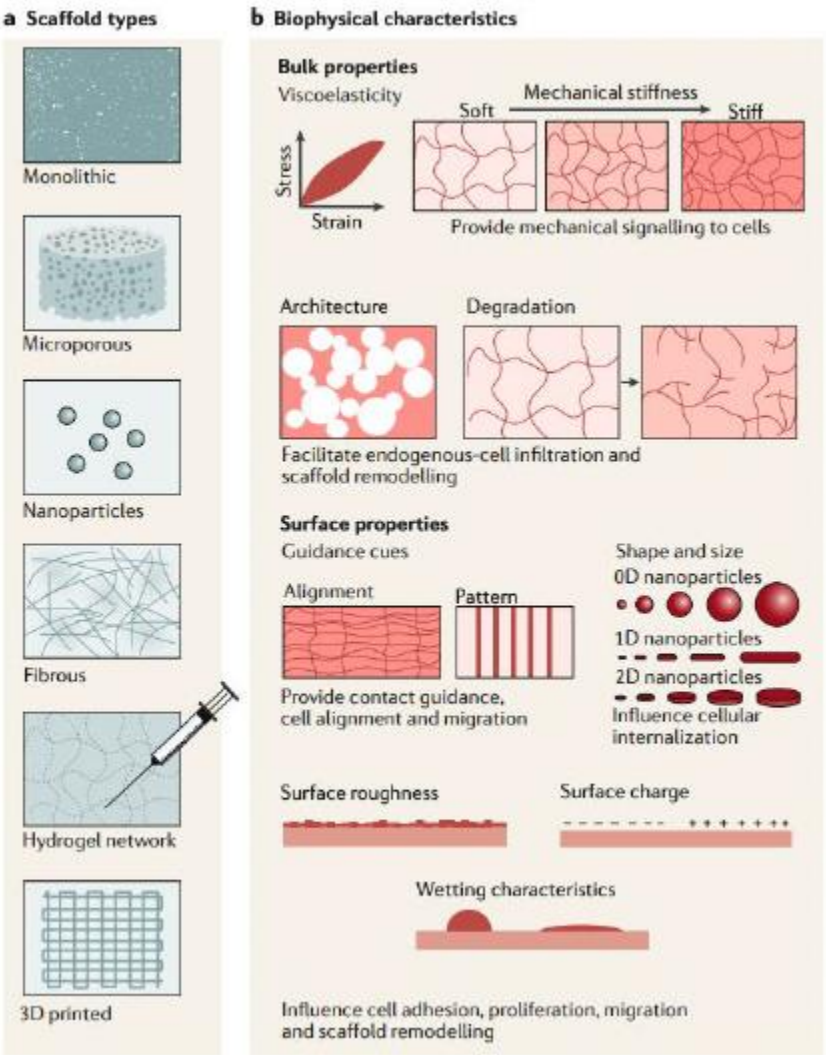

Figure 8: Methods for designing engineered biomaterials in tissue regeneration: a) Various scaffold types have been created, including monolithic, microporous, nanoparticle-based, fibrous hydrogel networks, and 3D printed structures. These aim to replicate the unique attributes of diverse tissues in the body. b) Depending on their specific biophysical traits, scaffolds have the potential to influence a wide array of cellular reactions, encompassing adhesion, migration, proliferation, and differentiation.

3. Materials and Methods

3.1 Hybrid Materials

A prevalent category of materials utilized in Multi – Photon Lithography (MPL) is the hybrid organic-inorganic photoresists. These materials possess a distinct advantage in the competitive realm of TPL due to the fusion of seemingly opposing characteristics from both the organic and inorganic constituents. Specifically, the organic component enables the manipulation of mechanical properties, control over porosity, and infusion of supplementary physical or biological attributes into the material. On the other hand, the inorganic portion bestows thermal and mechanical stability upon the material. It also facilitates the adjustment of the refractive index (RI) of the hybrid material, contributing to electronic, electrochemical, or active photonic attributes.

3.1.1 Material Synthesis

This study introduces a hybrid organic-inorganic photoresist named SZ2080^{TM} [108], synthesized and utilized in the present work. The synthesis process, known as sol-gel, is summarized in Figure 9[45,109]. Central to the material are methacryloxypropyl trimethoxysilane (MAPTMS) and Zirconium Propoxide (ZPO), which, by altering the molar ratio, lead to distinct properties like varying refractive indices or mechanical traits. To elaborate, the initial hydrolysis reaction involves the replacement of three methyl groups in the silicate molecule with hydroxyls from the hydrolyzed MAPTMS. Subsequently, ZPO forms a complex with Methacrylic Acid (MAA) and undergoes hydrolysis. The two reactants are then combined, resulting in the creation of an organic-inorganic network through a condensation step, modifying the silicate organic component with the Zirconium-based inorganic aspect. Lastly, the addition of a photoinitiator molecule, responsible for photon absorption and initiating free radical polymerization (FRP), completes the process, following a well-defined mechanism [110].

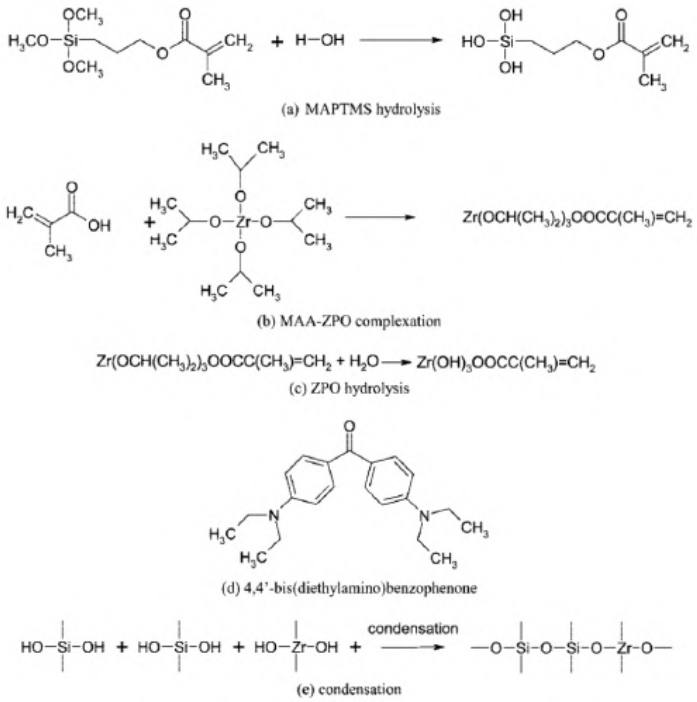

Figure 9: Structural representation of the constituents involved in the sol-gel process, guiding the creation of the organic-inorganic resin SZ2080. The image has been referenced from [108].

In summary, methacryloxypropyl trimethoxysilane (MAPTMS, 99%, sourced from Polysciences Inc.) underwent hydrolysis using diluted HCl. In a separate process, methacrylic acid (MAA, 98%, obtained from Sigma-Aldrich) and zirconium n-propoxide (ZPO, 70% in propanol, from Sigma-Aldrich) were combined in a 1:1 molar ratio and stirred for half an hour. Subsequently, this second mixture was gradually introduced into the first. This study employed two distinct photoinitiators: Sudan Black B (SBB) (Sigma-Aldrich, 0.04% relative to the monomers) for treating 3D structures with low autofluorescence, and 4,4′-bis(diethylamino) benzophenone (Michler's ketone, Sigma-Aldrich, 1% relative to the monomers). Notably, Michler's ketone was directly incorporated within the material, while SBB was initially blended with isopropanol at a concentration of 0.3% w/v. Subsequently, a 1:10 dilution was performed before adding it to the material (resulting in a final concentration of 0.04% concerning the monomers). Following the addition of the photoinitiator, all materials underwent filtration using a 0.2µm pore filter.

3.1.2 Sample Treatment

Following the construction of the structures, the samples are rinsed in a mixture of 4-methyl-2-pentanone and isopropanol (1:1) for 1 hour, followed by an additional five minutes in isopropanol/deionized water (1:1) solution. This process aims to remove any non-polymerized material. Subsequently, the samples are allowed to air dry.

3.1.3 SBB Treatment

To eradicate any residual autofluorescence, all thin films and structures underwent a treatment with SBB. In essence, the specimens were submerged in a newly prepared solution containing 0.3% w/v SBB dissolved in 70% EtOH for a duration of 48 hours. Subsequently, they were subjected to multiple rinses with EtOH until no trace of the dye was discernible.

3.2 Two – Photon Polymerisation Setup

The light source employed for the Two-Photon Polymerization (2PP) process is a Femto-second Fiber Laser (FemtoFiber pro NIR, Toptica Photonics AG) emitting at 780 nm with a pulse duration of 150 fs, an average output power of 500 mW, and a repetition rate of 80 MHz [111]. The beam is divided by a beam splitter into two setups using different beam-guiding principles, with a 70:30 ratio. The main approach employed in this thesis utilizes a galvo-scanner to deflect the beam according to the specific geometry of each layer, enabling the rapid fabrication of expansive areas. Another setup relies solely on stage movement to print the layer geometry, yielding ultra-high-resolution structures with a spatial resolution in the nanometer range.

The beam traverses an acousto-optic shutter that functions as a high-frequency Q switch, allowing or blocking the beam through the crystal; adjusting the crystal's rotation modifies the laser beam power using electrical signals [112]. Subsequently, the beam enters the Galvo scanner equipped with galvanometric mirrors, which scan the laser beam in the XY plane during fabrication. Increasing mirror movement speed enhances scanning speed and reduces fabrication time. Following this, the beam passes through a telescopic lens, expanding it to illuminate the full back aperture of the microscope objective lens to ensure optimal focusing.

The beam is then reflected by a dichroic mirror, with a Charged Coupled Device (CCD) camera positioned behind it to monitor the fabrication process and locate the focal point for initiation. The majority of the laser beam is directed to a microscope objective lens with high numerical aperture (NA), variable based on the lens, magnifying the beam and focusing it onto the sample. Higher

NA leads to enhanced resolution and working distance, while field of view is determined by microscope lens magnification. The sample is positioned on a high-precision three-axis linear translation stage with an accuracy of 100 nm.

Since this is a layer-by-layer printing technique aligned with the CAD design, the Galvo setup structures can fabricate with a layer distance of 100 nm. The stage's XY movement facilitates the creation of large areas through a stitching process, particularly valuable for metamaterials and metasurfaces fabrication. To observe the material's fluorescence during the fabrication process, a green LED beneath the stage is used, enabling visualization through the CCD camera.

The fabrication process commences by designing the structure in CAD software, followed by uploading the STL file to a custom software controlling the printing procedure, developed at FORTH. Proper alignment of the beam is crucial to ensure that it passes vertically through the microscope objective lens. Misalignment results in angled layer-by-layer printing and reduced structural quality. Once aligned, the sample is placed on the stage, and the material's photosensitivity assists in identifying the interface.

When the beam focuses within the material's volume, it generates bright spots due to polymerization. If the interface lies within the material, polymerized material will flow off the substrate during development. Adjusting the scanning speed and laser beam power becomes crucial to initiating the polymerization process without damaging the material due to high power.

Upon completing the printing, the previously mentioned development protocol is followed to achieve the final structure. A simplified depiction of the optical path is presented in Figure 10 below[113].

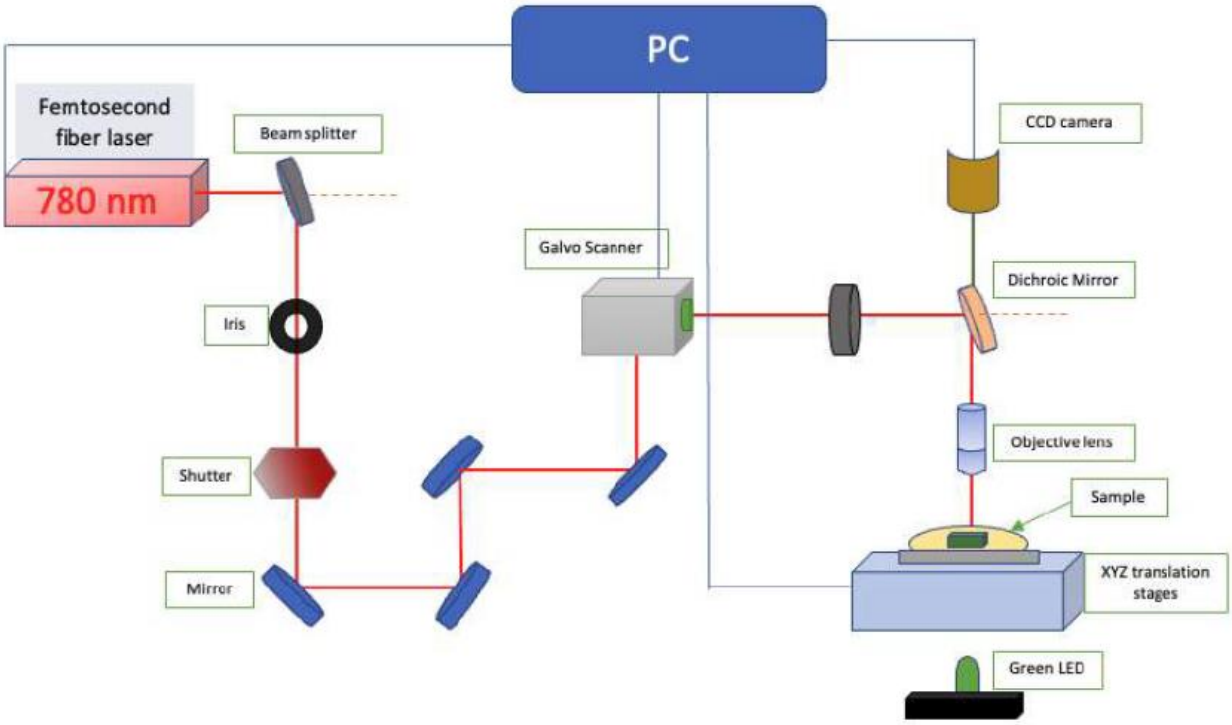

Figure 10: The Two – Photon set up[113].

3.3 One – Photon printer and Resin

In this research, an LCD 3D printing system (Anycubic, PHOTOTN MONO 4K) was employed, along with UV-sensitive resin sourced from the same manufacturer. The resin is a blend consisting of polyurethane acrylate (30-60%), isooctyl acrylate (10-40%), and the photoinitiator Irgacure 127 (2-hydroxy-1-(4-(4-(2-hydroxy-2-methylpropionyl) benzyl) phenyl)-2-methylpropan-1-one) at a concentration of 5%, referred to as "clear."

The 3D printing system comprises an LCD screen for projecting segmented images, a vat with a non-adhesive treatment to accommodate uncured resins, and a motorized metal build plate to secure the printed samples. The LCD printing method follows a bottom-up approach, utilizing smaller resin volumes during fabrication. This method enables a heightened vertical resolution and shorter curing time compared to alternative techniques. The bottom of the resin is shielded from an oxygen-rich environment, which impedes the photocuring process.

Following 3D printing, the scaffolds were immersed in bulk ethanol and placed within an ultrasonic bath for a duration of 15 minutes. Subsequently, the ethanol was substituted with ultrapure water, undergoing another 15-minute sonication. This process was iterated multiple times until all unpolymerized resin was completely eliminated. Ultimately, the structures were immersed in water until the seeding phase. Given their notable hydrophobic nature, the structures were never

allowed to dry, as this would prevent cells from penetrating the pores during the initial seeding stage.

3.4 Hyperganic

Hyperganic is a trailblazing software company leading the charge in the burgeoning domain of algorithmic engineering. This transformative approach places digital algorithms at the forefront of design and manufacturing, revolutionizing how complex and customized products are conceived and realized. Hyperganic's software platform is purpose-built to empower engineers, designers, and manufacturers, providing them with the essential tools to harness the power of algorithmic engineering in shaping the next generation of products.

At the core of Hyperganic's methodology lies the notion that algorithms can serve as the architects of design, capable of generating and optimizing intricate blueprints, thus enabling unparalleled levels of customization and intricacy. Hyperganic's software suite empowers users to define design parameters, constraints, and objectives, harnessing algorithms to craft and enhance designs based on these inputs. This dynamic process facilitates swift iterations and design optimization, dramatically curtailing the time and costs typically associated with product development. Additionally, it breaks through the limitations of conventional methods, making it feasible to manufacture designs previously deemed too intricate or costly to produce.

Furthermore, Hyperganic's software is poised to facilitate the fusion of advanced manufacturing techniques such as 3D printing and additive manufacturing. By marrying algorithmic design with these cutting-edge manufacturing methods.

Algorithmic engineering signifies a transformative paradigm shift within the engineering domain, where the strategic application of advanced algorithms and computational methodologies takes center stage in the design and optimization of intricate systems and products. This burgeoning discipline has garnered substantial attention in recent times, primarily owing to its capacity to potentially reshape diverse industries. It empowers engineers and designers to harness algorithmic processes to address complex challenges that were hitherto considered impractical or time-prohibitive. In practical terms, consider the aerospace industry, where algorithmic engineering is instrumental in the fine-tuning of aircraft component shapes and structures, ultimately leading to improved aerodynamics and fuel efficiency. Additionally, within the healthcare sector, it assumes a pivotal role in crafting patient-specific medical implants and prosthetics, offering bespoke solutions that enhance patient well-being.

A striking facet of algorithmic engineering is its profound impact on refining manufacturing processes. This approach results in reduced production durations and costs, coupled with elevated component quality. Furthermore, algorithmic engineering finds itself at the forefront of developing

autonomous systems, exemplified by self-driving vehicles, where algorithms steer real-time decision-making and navigation. In essence, algorithmic engineering emerges as a transformative discipline with the capacity to catalyze innovation and operational efficiency across an extensive spectrum of industries.

Hyperganic has been used to create the scaffold's design through its algorithmic engineering technique. The designing takes place via code while at the same time you can control different parameters such as the thickness of the beams, the ratio of the imported unit cell file, the size of the scaffolds etc.

3.5 Theoretical Analysis

In this study, we employed two distinct software applications for our theoretical analysis: ANSYS Student R1 and SolidWorks. Both unit cells were designed prior using Fusion360 and saved as DXF files. ANSYS was utilized to compute the Poisson ratio of the scaffold's unit cell, while our colleague at UC Berkeley employed SolidWorks 2022 for a similar analysis of the scaffold's Poisson ratio.

These DXF files were subsequently imported into ANSYS Workbench. Within the Workbench environment, specific parameters were defined for the Static Structural analysis. These parameters included specifying the material properties, identifying the locations and magnitudes of applied forces on the unit cell, defining fixed supports, and specifying the type of analysis to be performed.

3.6 Mechanical Analysis

The mechanical analysis of the scaffolds was conducted using CellScale's MicroTester LT 4.5. This system offers the capability to record scaffold deformation while it is subjected to stress. It also provides simultaneous data acquisition for various parameters, including time, force, tip displacement, base displacement, current size, and temperature. Additionally, the software enables the generation of graphical representations such as Force-Time, Displacement-Time, and Force-Displacement curves.

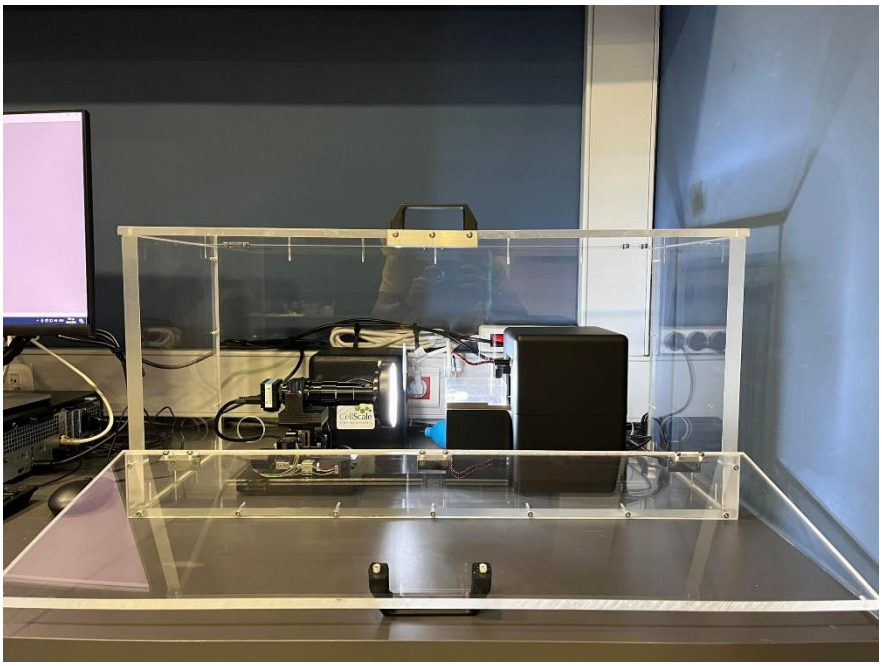

Figure 11: The MicroTester LT 4.5.

3.7 Mesenchymal Stem Cells

Mesenchymal stem cells (MSCs) stand as a remarkable category of multipotent stem cells with profound implications in the realms of regenerative medicine and tissue engineering. Derived from diverse sources including bone marrow, adipose tissue, and umbilical cord blood, MSCs exhibit an exceptional capacity to differentiate into multiple cell types, encompassing osteoblasts, adipocytes, and chondrocytes. Their immunomodulatory attributes render them promising contenders for the treatment of autoimmune and inflammatory disorders. Additionally, their low immunogenicity heightens their therapeutic appeal by reducing the likelihood of immune rejection upon transplantation. MSCs, renowned for their regenerative potential, immune-modulating capabilities, and adaptability, have spurred extensive research endeavors aimed at unlocking their potential in tissue restoration, organ rejuvenation, and disease intervention [114,115].

Notably, MSCs are distinguished by their capacity to release an array of bioactive molecules collectively referred to as the "secretome." This repertoire includes growth factors, cytokines, and extracellular vesicles, all playing pivotal roles in orchestrating tissue repair and regeneration. MSC-secreted factors have been documented to stimulate angiogenesis, fine-tune immune responses, and foster the proliferation and differentiation of resident tissue cells. This paracrine activity has spurred investigations into harnessing the therapeutic prowess of the MSC secretome, not only as an alternative to cell-based therapies but also as a potential remedy for conditions such

as myocardial infarction, stroke, and degenerative joint ailments. The multifaceted attributes of MSCs and their secretome continue to be actively explored in both preclinical and clinical studies, paving the way for innovative regenerative and immunomodulatory interventions [116,117].

3.8 Cell Culturing

For all experiments, Mouse Bone Marrow Mesenchymal Stem Cells (BM-MSCs) from Cyagen in California, USA, were utilized, as they are widely recognized as the gold standard in tissue engineering and regenerative medicine. These cells were incubated at a temperature of 37°C within an atmosphere consisting of 5% CO_2. This was achieved by using Low-glucose Dulbecco's Modified Eagle's Medium (DMEM) from Gibco, Invitrogen, Karlsruhe, Germany, supplemented with 10% heat-inactivated Fetal Bovine Serum (FBS) from Gibco, Invitrogen, Karlsruhe, Germany, and 1% penicillin/streptomycin also from Gibco, Invitrogen, Karlsruhe, Germany.

To prepare the 3D scaffolds, the coverslips were sterilized through immersion in 70% ethanol, followed by UV light exposure for a duration of 1 hour. Subsequently, these sterilized scaffolds were positioned within a 24-well plate from Sarstedt, Numbrecht, Germany. A seeding density of 10^4 cells/mL was introduced into the scaffolds, resulting in a total volume of 1 mL. The seeded scaffolds were then incubated at 37°C for a period of 5 and 7 days using the same medium as described earlier. The seeding process was initiated when a confluent flask reached 90% confluence.

3.9 Scanning Electron Microscopy

To prepare samples for scanning electron microscopy (SEM) imaging, a seeding density of 10^4 cells/well was used, and the cells were cultured for a period of 5 and 7 days. Following this timeframe, the cells underwent fixation using a protocol specifically designed for SEM analysis. In summary, the culture medium was first removed, and the cover slips were then subjected to two washes with a 0.1 M sodium cacodylate buffer (SCB). Subsequently, a solution containing 4% w/v glutaraldehyde (GDA) in SCB was applied, followed by two additional washes with SCB. The specimen was then carefully dehydrated through a series of ethanol solutions, ranging from 30% to 100%. Subsequently, the specimens were air-dried through the evaporation of hexamethyldisilazane (HMDS[118]. Initially, the samples were immersed in a 2:1 solution of EtOH-HMDS, followed by consecutive immersion in a 1:1 ratio, a 1:2 ratio and ultimately, three successive washes with pure HMDS. Subsequently, the specimens were left to air-dry overnight. Lastly, a 10 nm gold sputter coat was applied using the same equipment (Baltec CPD 030).

3.10 Live/Dead assay & DAPI

In order to evaluate the influence of the scaffold design on cells, prior to conducting a live/dead assessment, they were subjected to a treatment with SBB (0.3% w/v in EtOH). A live/dead assay was conducted on a culture of Mesenchymal Stem Cells (MSCs). Initially, a total of 10^4 cells were seeded onto the scaffolds and then cultivated within an incubator at 37°C with 5% CO_2 for a span of 5 and 7 days.

To evaluate cell viability, a Live/Dead kit from Life Technologies in Carlsbad, CA, USA, was employed. This entailed labeling live and deceased cells using specific markers. Specifically, the cells were subjected to an incubation in LG – DMEM containing ethidium homodimer-1 (EthD-1, 2 μM) and calcein AM (0.5 μM) for a duration of 10 minutes at room temperature. During this process, live cells were labeled with calcein AM (green), while dead cells were labeled using ethidium homodimer-1 (red). Subsequently, the coverslips were inverted and mounted onto a glass slide using a slow fade mounting medium that included 4',6-diamidino-2-phenylindole (DAPI) from Life Technologies in Carlsbad, CA, USA. Ultimately, the labeled cells were visualized using a confocal microscope, specifically the Leica SP8 inverted confocal, Leica Microsystems.

3.11 Confocal Microscopy

Confocal microscopy was a pivotal technique employed in this study for the assessment of live and dead cells. This cutting-edge imaging method allowed for the precise visualization and discrimination of living and deceased cellular entities within the samples. By utilizing distinct channels to represent live/dead cells and DAPI employing advanced image processing procedures, confocal microscopy facilitated a detailed and accurate analysis of cell viability, contributing valuable insights to the research conducted in this work.

3.12 Confocal Images Analysis

To perform the confocal image analysis, we employed the ImageJ™ software. Initially, we applied separate thresholding to the various z scans of the images, ensuring that all cells were distinctly visible. In the context of live/dead analysis, we utilized the red channel to represent deceased cells and the green channel to depict living cells. This distinction was achieved through the AND procedure within the image calculator tool. Finally, we computed the intensities of each image slice and created graphs using either Microsoft Excel or Origin™ software.

4. Results & Discussion

4.1 Design of the Auxetic Metamaterials

There are two designs: one is the widely recognized reentrant auxetic design known as "Bowtie," and the other is a novel design inspired by the well-known auxetic star, referred to as "Shuriken." The configuration of these auxetic mechanical metamaterials is based on varying angles and ratios within their shapes. To provide more details, in the Shuriken design, variations are achieved by adjusting the inner radius angle of beams, ranging from 20° to 60° with a step size of 5°. Meanwhile, in the Bowtie design, variations are introduced by altering the ratios between parallel and reentrant beams, ranging from 1:1 to 1:2 with a step size of 0.25.

The design of the scaffolds was accomplished through Hyperganic, particularly using the Recipe Viewer application. This tool provides us with the flexibility to modify numerous parameters, as previously mentioned, using a specialized code developed by the company.

Using a code and various DXF files, some of these designs were ultimately generated. All the designs and the code can be found in Appendix A.

The aim of these designs was to investigate how varying the inner angles in Shuriken and the different ratios in Bowtie can impact their mechanical properties and the extent of this impact.

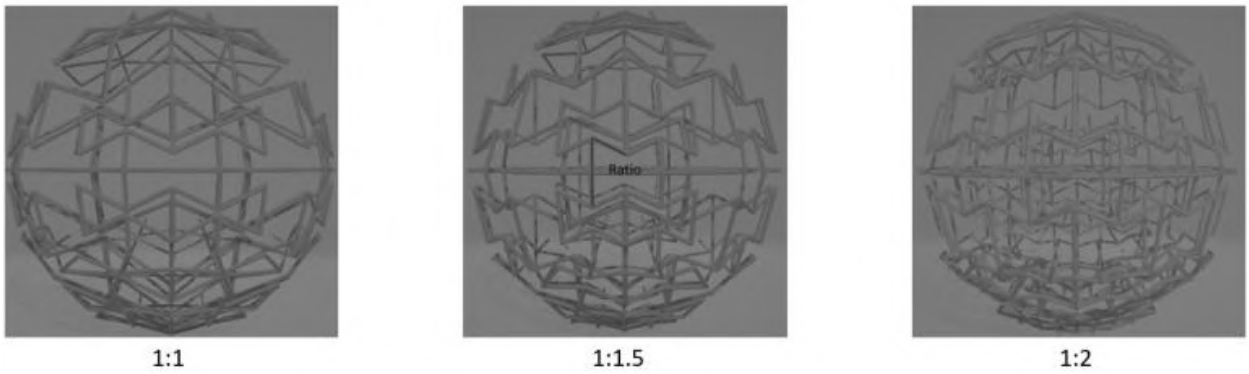

Figure 12: The differences in Bowtie spheres by changing the ratio.

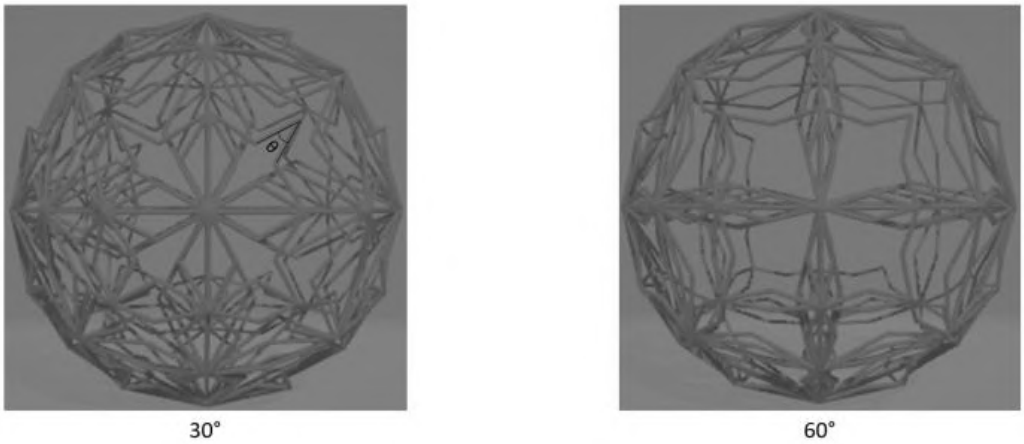

Figure 13: The differences in Shuriken spheres by changing the inner angle of the unit cell.

It is evident that increasing the inner angle in Shuriken results in a more open unit cell geometry, along with the spaces within the sphere where cells are intended to grow. In contrast, in Bowtie, when the ratio increases, the sphere exhibits fewer open geometries. This presents a positive aspect, as the increased open geometry can facilitate nutrient exchange between cells and the culture medium. On the downside, the greater openness of the unit cells can hinder cell migration on the scaffold. This issue can be addressed either by adjusting the code to reduce the unit cell size or by decreasing the diameter of the sphere.

4.2 One – Photon Fabrication

Following the design of the spheres, they were initially fabricated using our commercially available One – Photon printer, as previously mentioned. The STL files were sliced using Anycubic's software known as Photon Workshop. The fabrication was accomplished using a 20 μm step and an exposure time of 30 seconds per layer. These spheres have a diameter of 1 cm and were subsequently examined under a scanning electron microscope (SEM).

A different orientation was employed in the printing of Bowtie sphere to achieve a more vertical directionality.

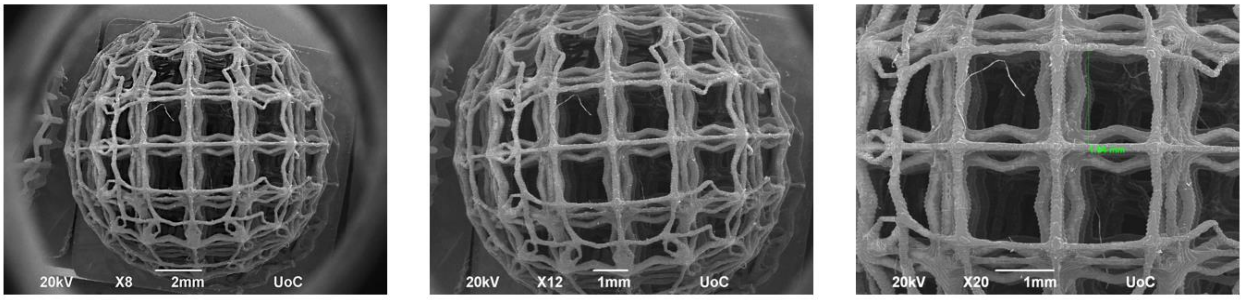

Figure 14: SEM pictures of Shuriken spheres with 1 cm diameter.

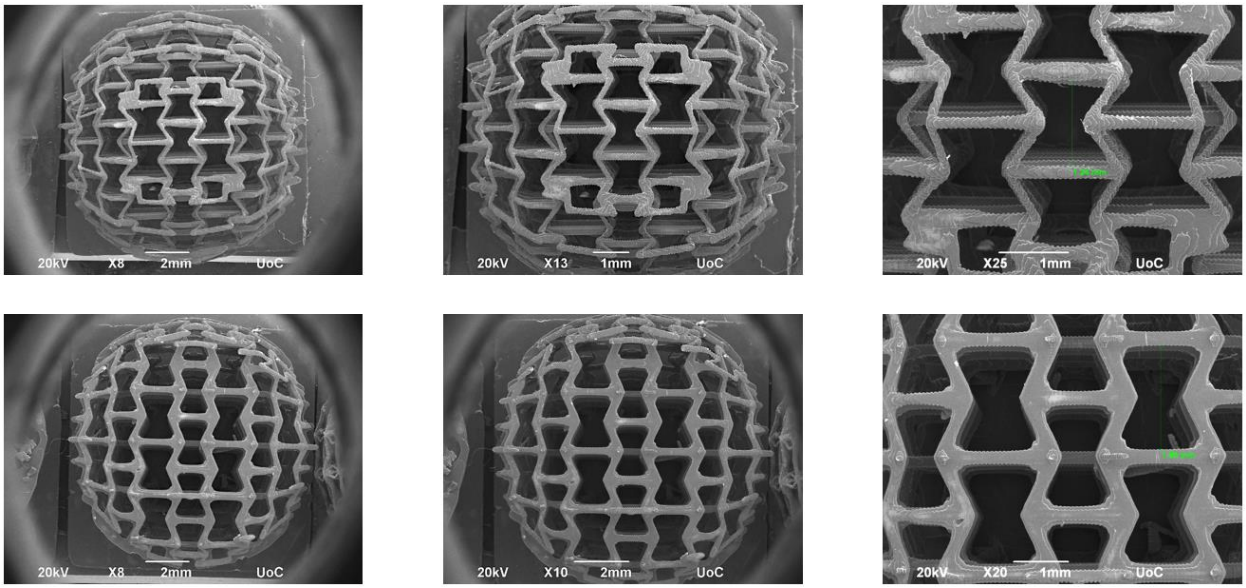

Figure 15: SEM pictures of Bowtie spheres with 1 cm diameter and two different orientations.

4.3 Multi – Photon Lithography

The next step, following the fabrication of the spheres via the SLA printer, involved downscaling. It was necessary to determine parameters such as the beam speed and power. For this purpose, the spheres initially created using the custom made "Galvo" setup were designed to have dimensions of 100 μm for reasons related to both time efficiency and structural considerations. The power settings were tested in the range of 20 to 120 mW with increments of 10 mW, while the fabrication speed was varied from 500 to 5000 μm/s with increments of 500 μm. Additional photos for this chapter are located in Appendix C.

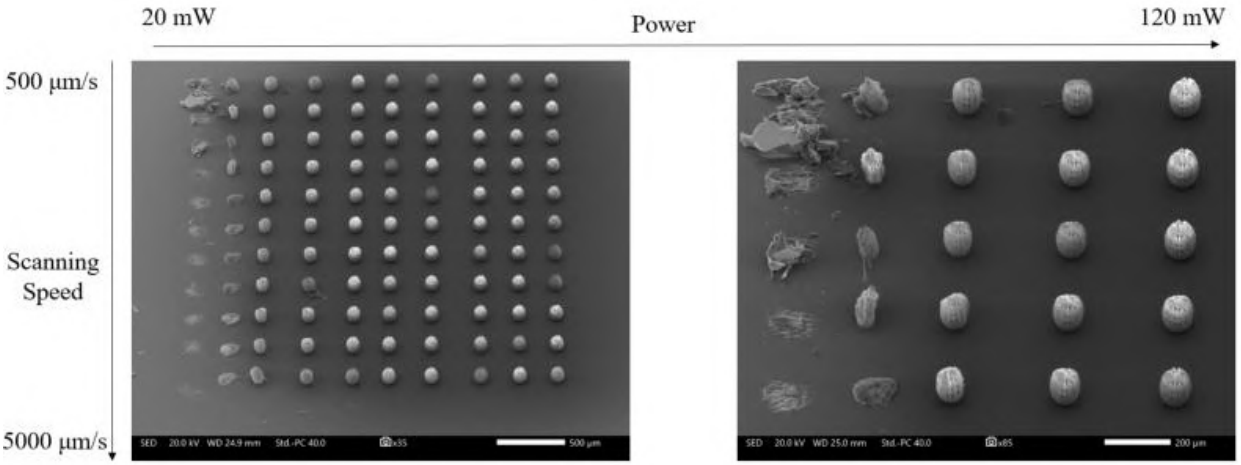

Figure 16: Parameters for spheres with a diameter of 100 μm. On the right is a magnified image of the top-left section of the left photo.

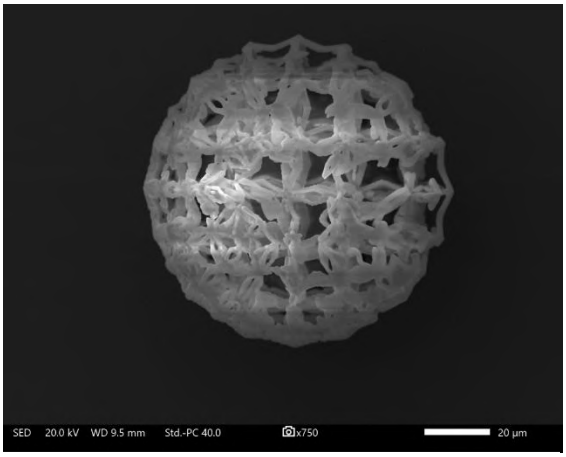

Figure 17: A top view of a sphere that was fabricated.

To allow cells to penetrate the sphere, it was necessary to increase the unit cell size progressively, which led to the continued fabrication of spheres with a diameter of 200 μm.

At a diameter of 200 μm, we encountered a distinct challenge. Due to the insufficient height of the droplet, spheres could not be fabricated. To overcome this issue, we needed to increase the height

of the droplet on the fused silica substrate because the desired fabrication could not be achieved initially. At this stage, various slicing parameters were also tested. Specifically, slicing thicknesses were evaluated in the range from 0.3 to 0.5 μm, with increments of 0.1 μm. This presented a structural challenge as larger spheres posed additional complexities in their fabrication.

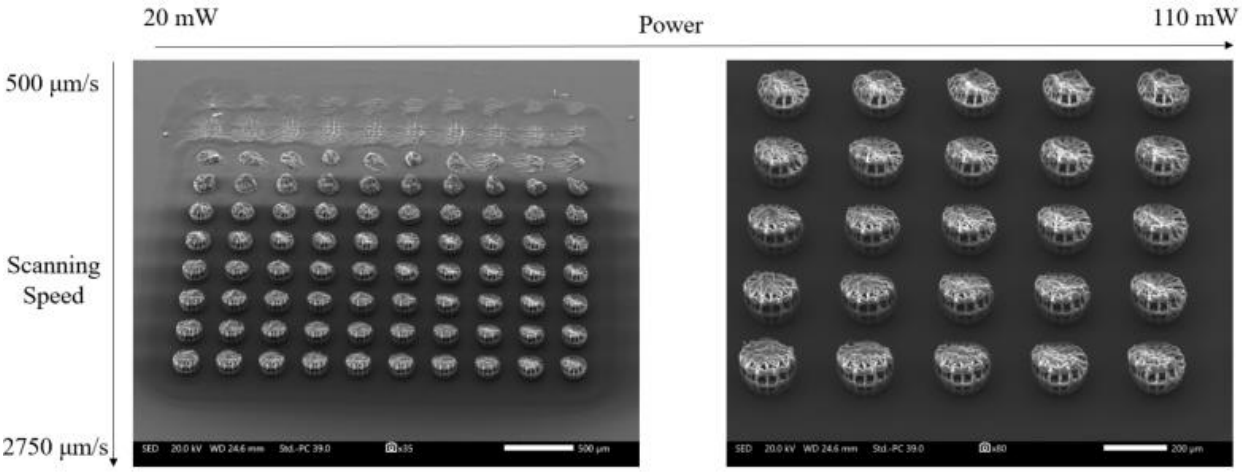

Figure 18: Parameters for spheres with a diameter of 200 μm. On the right is a magnified image of the bottom-right section of the left photo.

After the droplet's height was adjusted accordingly, we were finally able to successfully complete the fabrication process. It was determined that the optimal parameters for this process were a power setting of 80 mW and a speed of 1000 μm/s.

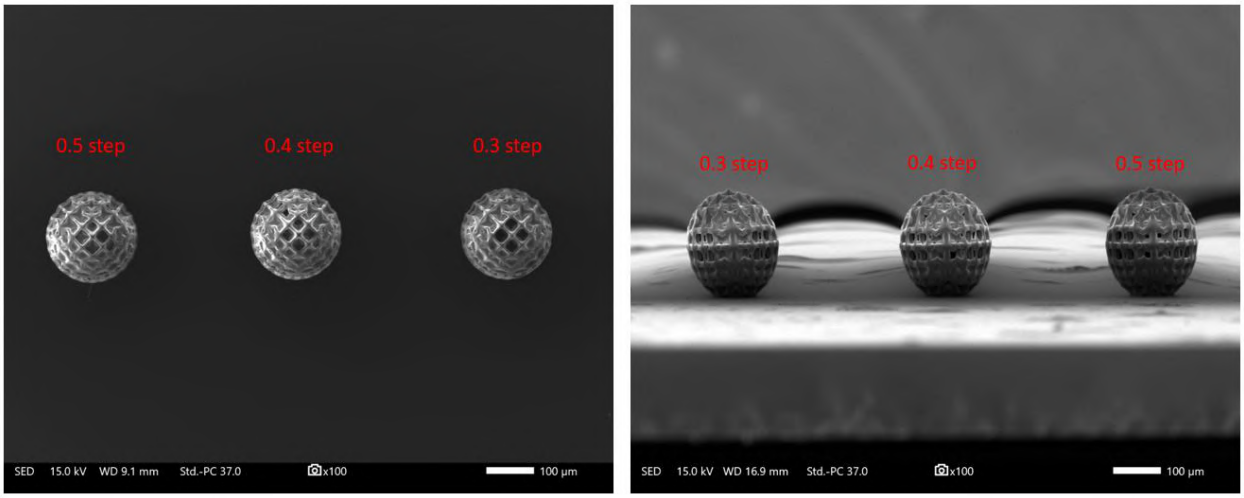

Figure 19: 200 μm in diameter spheres with different slicing steps.

To achieve the barrier of 400 μm, it was determined that a slicing step of 0.3 μm would be more suitable. This choice was based on the expectation that it would provide both improved resolution and enhanced structural stability for the fabrication process.

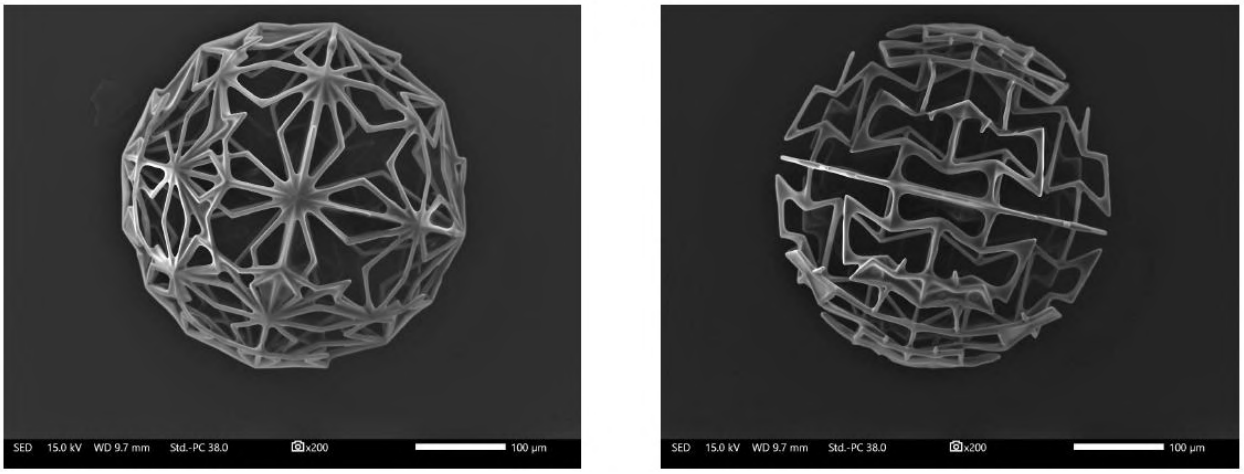

Figure 20: Top view of the spheres. On the left is the Shuriken and on the right is the Bowtie.

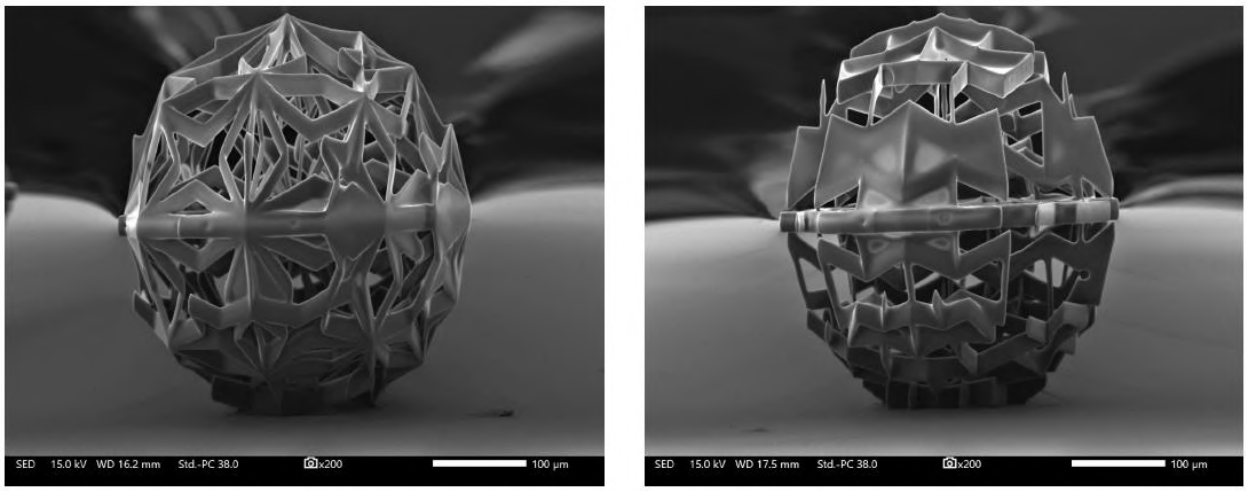

Figure 21: Side view of the spheres. On the left is the Shuriken and on the right is the Bowtie.

Despite some unit cells not being well-developed, the conclusion has been reached that a high-resolution print of a sphere was successfully achieved. With a diameter of 400 μm, there is sufficient space for the scaffold to be penetrated by cells and for growth to be facilitated within it, as opposed to just on the surface. The central unit cells, sized at 100 μm, play a crucial role in creating an environment conducive to cell growth and integration within the scaffold.

4.4 Theoretical Calculations

The Poisson's Ratio results were obtained from ANSYS 2023 R1 Student license, and it's essential to note that these calculations were conducted under conditions of elastic behavior. The chosen material for the analysis was Resin Epoxy, and its properties were directly incorporated into the software. The material properties include a density of 1160 kg/m³, a Young's Modulus of 3.78 x 10^9 Pa, a Poisson's Ratio of 0.35, a bulk modulus of 4.2 x 10^9 Pa, a shear modulus of 1.4 x 10^9 Pa, and a tensile yield strength of 5.46 x 10^7 Pa. They can be found in detail in Appendix C. The experiment was conducted using a vertical force of 0.2 N applied perpendicular to the orientation of the scaffold, which had a diameter of 1 mm. Both of their bases were employed as fixed points. The results revealed a negative Poisson's ratio of -0.11 for Shuriken 30 and -0.06 for Bowtie 1:15.

It is worth mentioning that these values were determined while both structures were exhibiting elastic behavior.

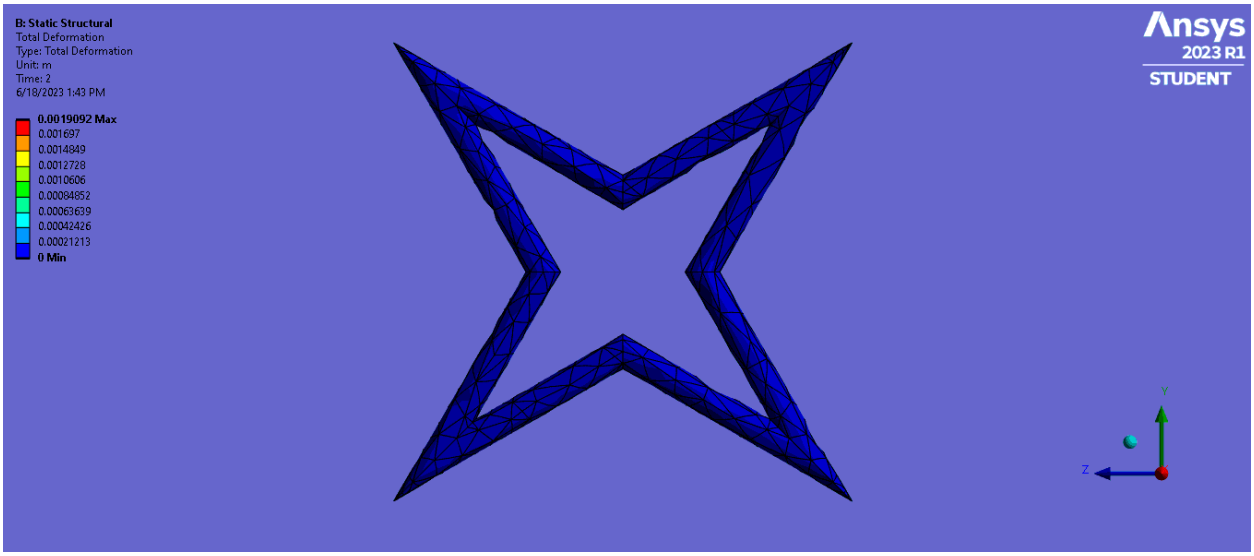

Figure 22: Shuriken30 simulation in ANSYS Workbench.

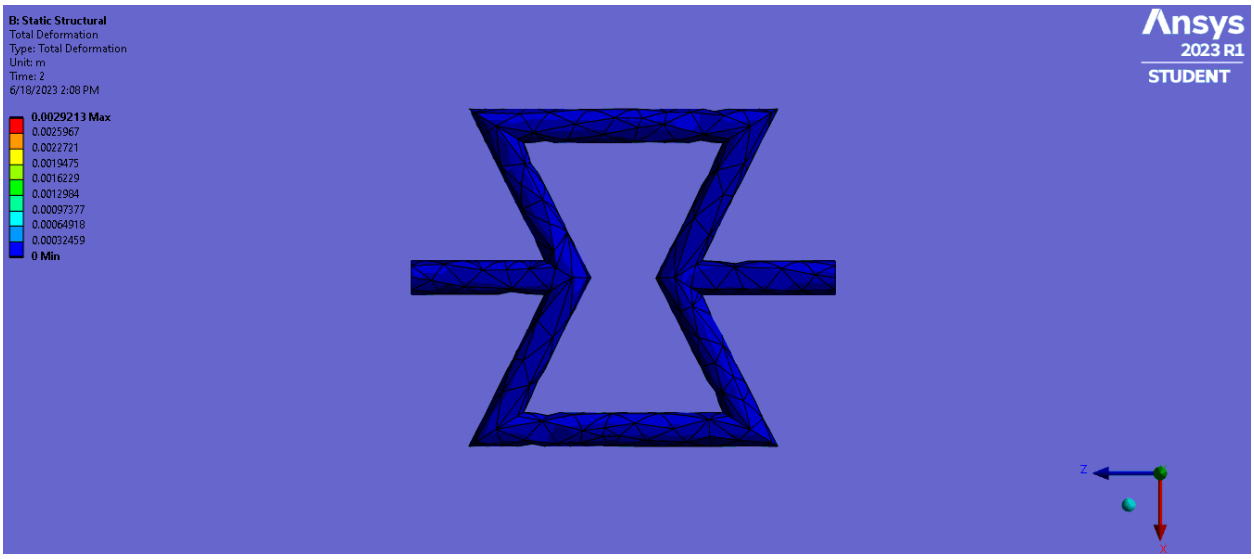

Figure 23: Bowtie 1:1.5 simulation in ANSYS Workbench.

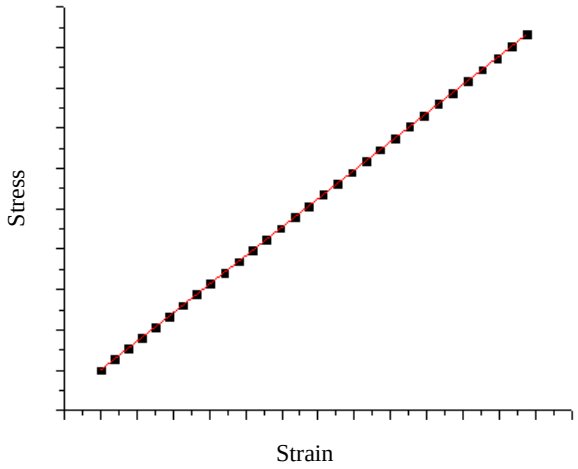

Figure 24: Elastic behavior

To facilitate the results, our colleague at UC Berkeley, performed the Finite Element (FEM) analysis by importing the data into the commercial software SolidWorks2022 and recreating the 3D trusses. We extracted the coordinates of the beams and the junction points where they intersect and we provided to them in order to rebuilt and extract the experiment. These images can be found in Appendix C.

Thanks to the multiple symmetry planes of the trusses, only the mechanical behavior of a part of the whole structure was simulated in order for the computation cost to be decreased. Specially, for the shuriken truss, the 1/16 of the whole sphere was used in the simulation and, for the bowtie truss, the 1/8 of the whole sphere was used. The symmetry planes were replaced by roller supports

(e.g., for a joint that is located on a symmetry plane, only its translation motion on the plane and its rotation around the vertical axis of the plane are allowed) .

As the simulation should be limited to the elastic region, in both cases a test load of 100 μN was applied. For Shuriken and Bowtie, 553 and 609 elements were used respectively.

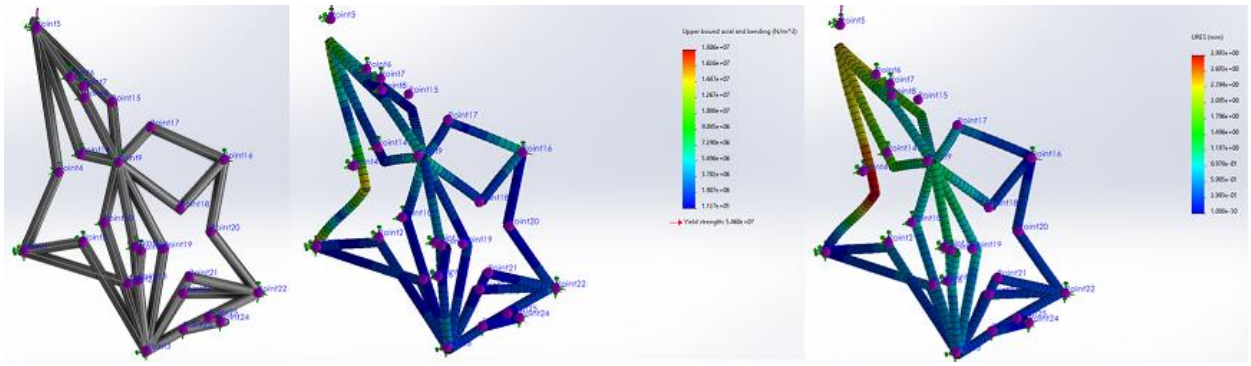

Figure 25: Shuriken30 simulation. Left; the 3D truss that was employed for the simulation, Middle; stress simulation of the truss, Right; displacement simulation of the truss.

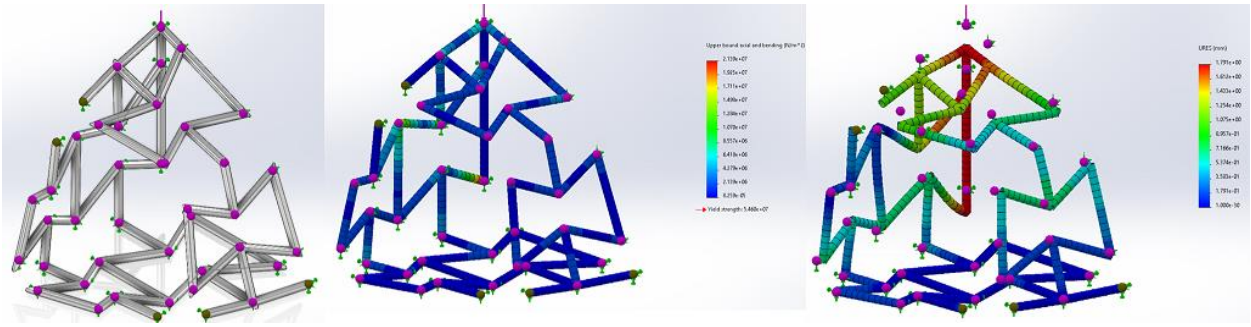

Figure 26: Bowtie1:15 simulation. Left; the 3D truss that was employed for the simulation, Middle; stress simulation of the truss, Right; displacement simulation of the truss.

For the Bowtie truss, the findings indicate a displacement of -1.791 μm at joint 16 and -0.08 μm at joint 30, resulting in a negative Poisson's ratio of -0.045. Conversely, for the Shuriken truss, there is a displacement of -2.552 μm at joint 5 and 0.451 μm at joint 3, resulting in a positive Poisson's ratio of 0.178. This displacements were utilized to calculate the Poisson's Ratio. In comparison, the theoretical Poisson's ratio of a solid sphere is 0.333.

4.5 Micro Indentation

Micro-indentation tests were performed to validate whether the spherical scaffolds exhibit auxetic characteristics. This method serves as an additional means of characterization and can either confirm or refute the theoretical calculations. These experiments were carried out using the same machine mentioned in Chapter 3.6.

The experimental procedure involved a 10-second compression, followed by a 1-second hold, a 10-second recovery, and a 5-second rest period. This cycle was repeated twice for each sample. The second cycle was employed to facilitate plastic deformation.

The MicroTester LT allowed us to obtain data for Force-Time, Displacement-Time, and Force-Displacement charts, all of which were graphed for each sample. These charts can be found in Appendix D.

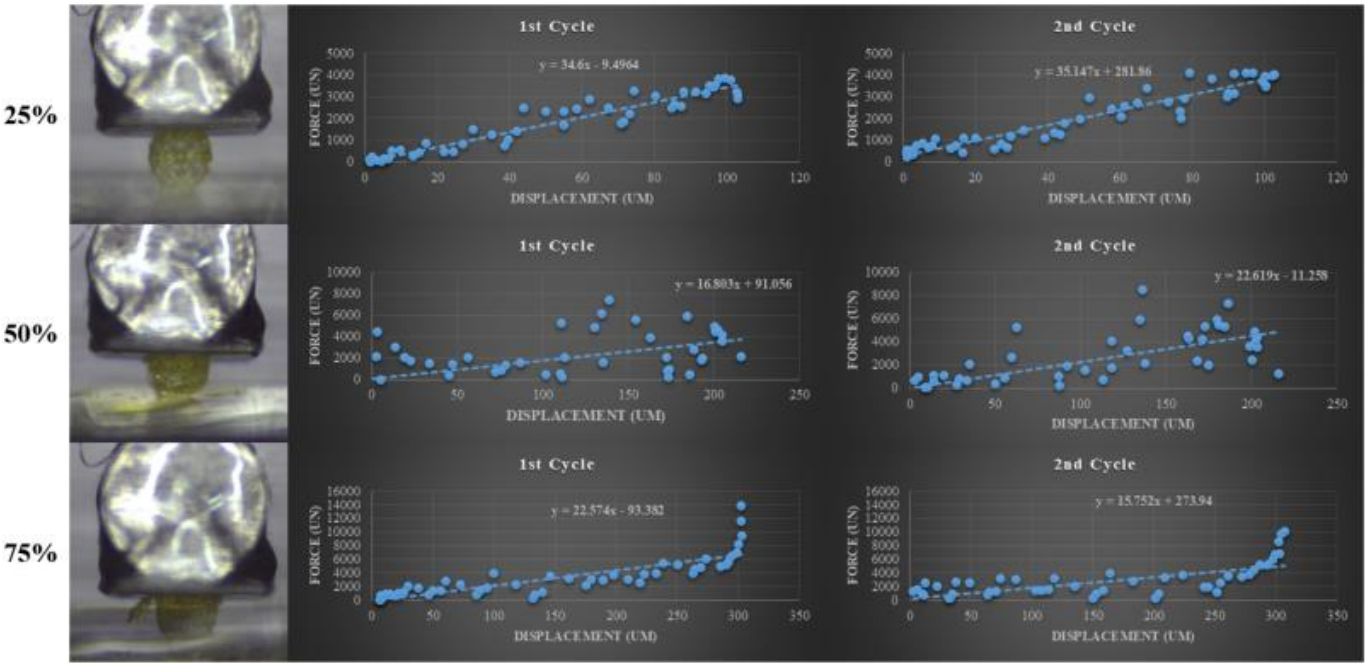

Figure 27: Comparison between 25%, 50%, 75% compression and 1st and 2nd cycle for each compression. The slope of the line on the plot represent the stiffness in MPa.

Based on the ImageJ analysis, the Shuriken sphere displayed an auxetic characteristic, with recorded Poisson's Ratios of -0.081 for 25%, -0.078 for 50%, and -0.076 for 75%.

Upon comparing the plot analysis between the first and second cycles, it becomes evident that we can draw two potential conclusions: either the material exhibits elastic behavior, or there might be signs of plastic deformation or failure within a particular region of the sphere. Typically, in many cases, the second cycle tends to exhibit lower values of stiffness because the plastic deformation

or failure has already occurred during the first cycle. This pattern is often observed when analyzing the mechanical behavior of materials or structures subjected to cyclic loading.

For the 25% displacement (100µm), it was interesting to note that the slope values were quite similar, differing by only approximately 0.5. This observation suggests that the scaffold's stiffness is approximately 34.9 MPa. Moreover, the consistent linear behavior of these values and the constant slope indicated that the deformation occurred within the elastic region.

However, at a 50% displacement (200µm), the noticeable disparity in slope values between the first and second cycles raises a flag for a potential failure or plastic deformation within the scaffold's structure. Such variations in stiffness can serve as a crucial indicator of structural changes or evolving material behavior. Further investigation may be necessary to comprehensively grasp the underlying causes of this behavior.

In the case of 75% displacement (300µm), it appears that the second cycle plot provides less informative data due to the presence of a previous failure and plastic deformation during the first cycle. The initial cycle induced significant changes in the material or structure, rendering the data from the second cycle less valuable for analysis. This underscores the importance of interpreting data within the context of the entire experiment and understanding how earlier cycles can influence subsequent ones.

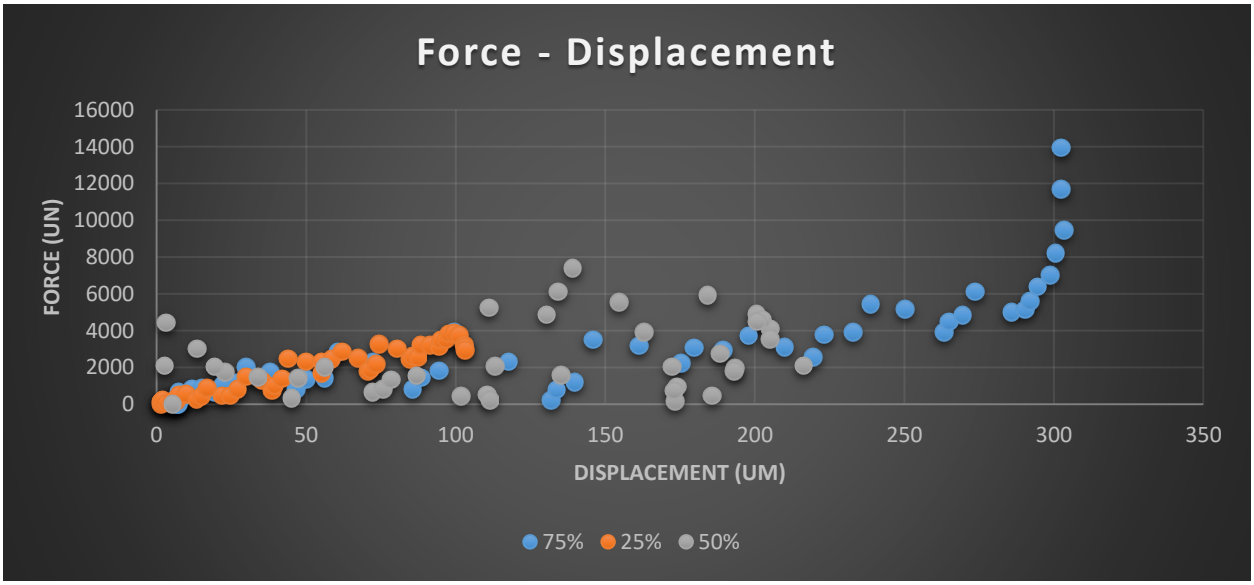

Figure 28: A Force-Displacement plot is provided for all three compression levels (25% in orange, 50% in gray, and 75% in blue) for the first cycle only.

The provided plot serves the purpose of comparing the variations among the three documented displacements during the initial cycle. It's evident that as the compression increases, the force

required to achieve that compression also rises. This trend indicates that the stiffness of the scaffolds increases as the level of compression intensifies, which aligns with our expectations.

To delve into specifics, at a 25% displacement, the maximum force value is approximately 4mN, and this value increases to 8mN for the 50% displacement. For the 75% displacement, which goes slightly beyond 14mN, the force requirement is even higher. This progression in force requirements correlates with the growing compression, demonstrating the scaffold's increased stiffness under these conditions.

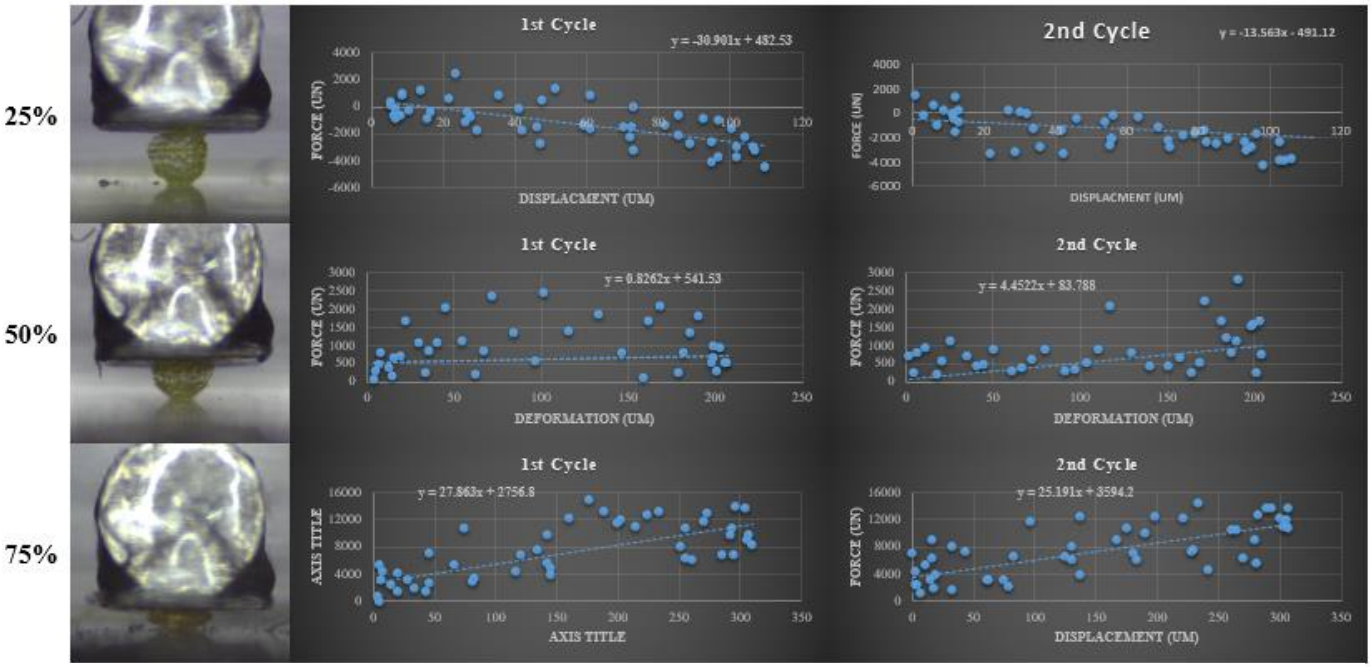

Figure 29: Comparison between 25%, 50%, 75% compression and 1st and 2nd cycle for each compression. The slope of the line on the plot represent the stiffness in MPa.

According to the ImageJ analysis, the sphere displays an auxetic characteristic, as evident from the calculated Poisson's Ratios of -0.167 for the 25% displacement, -0.023 for the 50% displacement, and -0.009 for the 75% displacement.

At the 25% displacement (100μm), the measurements indeed suggest the presence of negative stiffness, potentially indicating that the scaffold behaves like a mechanism. However, the substantial difference in the negative stiffness values between the first and second cycles strongly implies that an element within the truss structure experienced either a failure or plastic deformation following the first cycle. This observation highlights the need for a more in-depth examination of the scaffold's structural integrity and the possible effects of cyclic loading on its components.

For the 50% displacement (200μm), both cycles exhibit positive stiffness values, suggesting that there may have been changes in the scaffold's structural behavior. The disparity between the

stiffness values in the two cycles indicates that some elements of the scaffold have experienced failure and/or plastic deformation, contributing to this variation. Additionally, the scattered data points on the plot imply that the measurements may not be as precise or consistent, potentially due to instrument limitations. Further analysis and a closer examination of specific elements and their responses may provide insights into the causes of these variations.

In the case of the 75% displacement (300μm), both graphs indicate positive stiffness values, with the values being quite similar. The fact that the second cycle displays a smaller stiffness value aligns with expectations, considering the presence of failure and plastic deformation in the truss elements from the first cycle. This observation suggests that the material or structure may have been altered during the initial cycle, leading to the differences in stiffness between the two cycles.

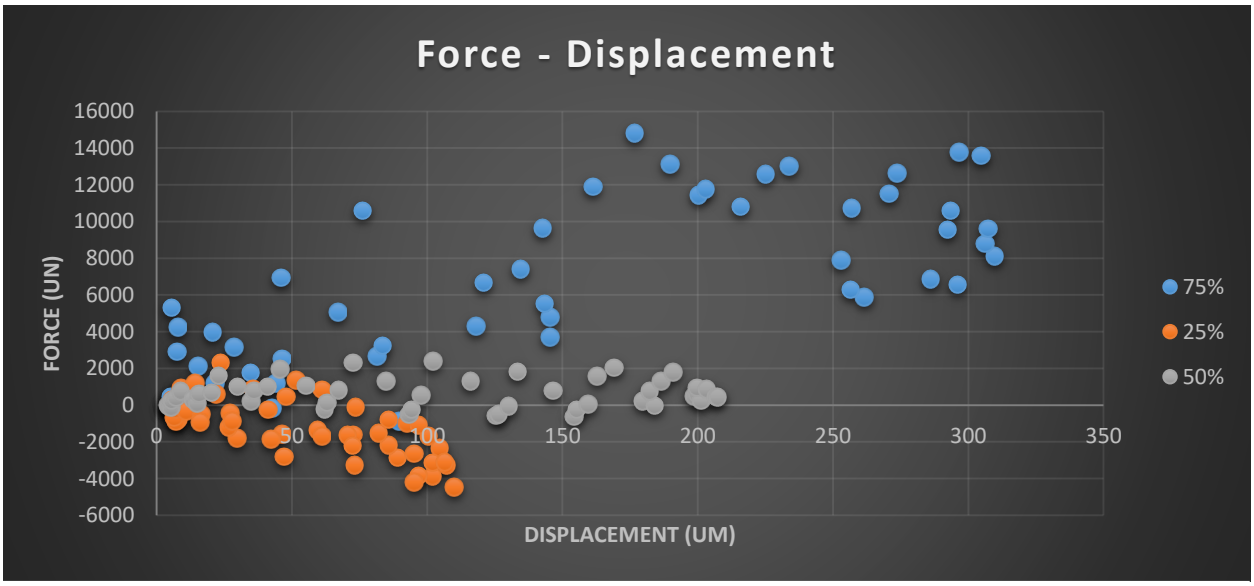

Figure 30: A Force-Displacement plot is provided for all three compression levels (25% in orange, 50% in gray, and 75% in blue) for the first cycle only.

The plot depicting Bowtie spheres similarly illustrates a consistent trend of increasing force in conjunction with an increasing displacement. Notably, despite the presence of negative force values at the 25% displacement, attributed to instrument inaccuracies, the overall pattern remains consistent. To provide more specific details, the negative values at the 25% displacement transition to just above 2mN at the 50% displacement, and they further rise to approximately 14mN at the 75% displacement. This progression highlights the proportional relationship between displacement and the force required, indicating a noticeable increase in stiffness as the compression intensifies.

4.6 SEM – Cell Seeded Scaffolds

The subsequent results illustrate the scaffolds that were seeded with 30,000 MSCs/mL for a duration of 7 days. Regrettably, the Bowtie sphere experienced a structural failure during the cell seeding procedure. Nevertheless, this setback did not significantly impact our experiment, as its primary aim was to explore the required cell density (cells/mL) and the duration (in days) needed for the investigation.

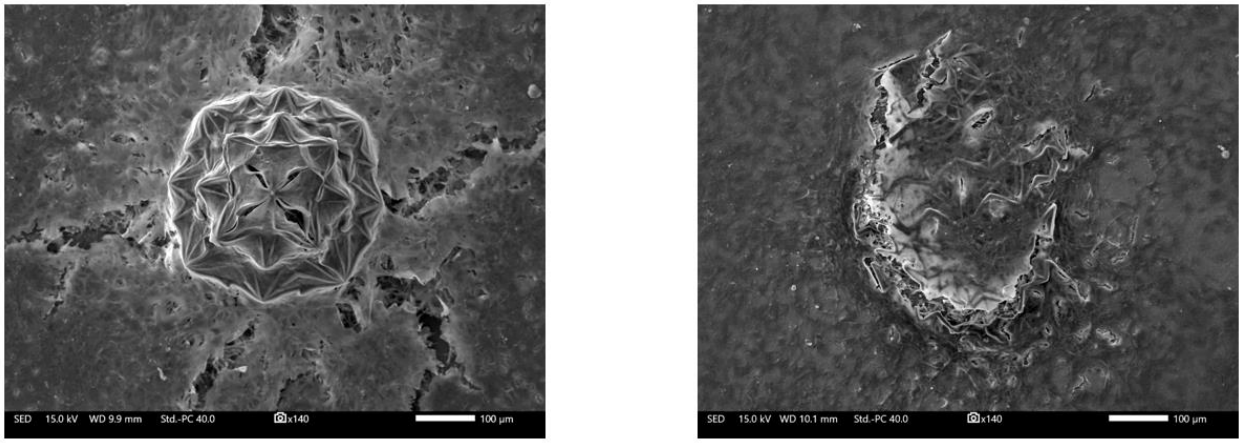

Figure 31: Top view of the seeded scaffolds.

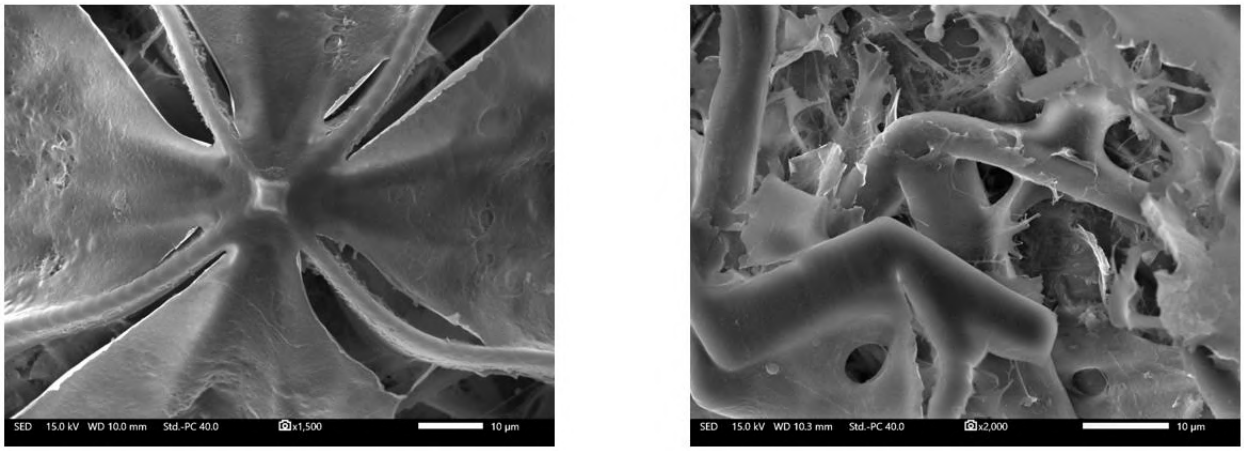

Figure 32: Closer top view.

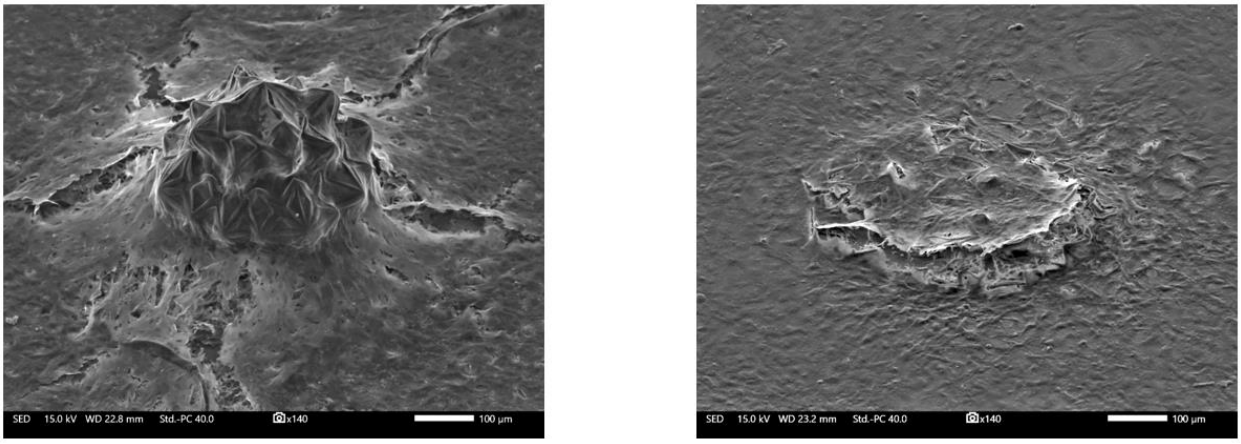

Figure 33: Tilted view of the seeded scaffolds.

Despite the appearance of cell growth within the scaffold in the images, we couldn't confidently interpret the results due to the high cell density. Therefore, we made the decision to introduce a 5-day time point and reduce the cell density to 10,000 cells/mL to obtain more reliable data.

The subsequent results are derived from three distinct time points: one at 3 days, one at 5 days, and the other at 7 days after seeding with a cell density of 10,000 cells/mL at day 0. Additional pictures can be found in Appendix E.

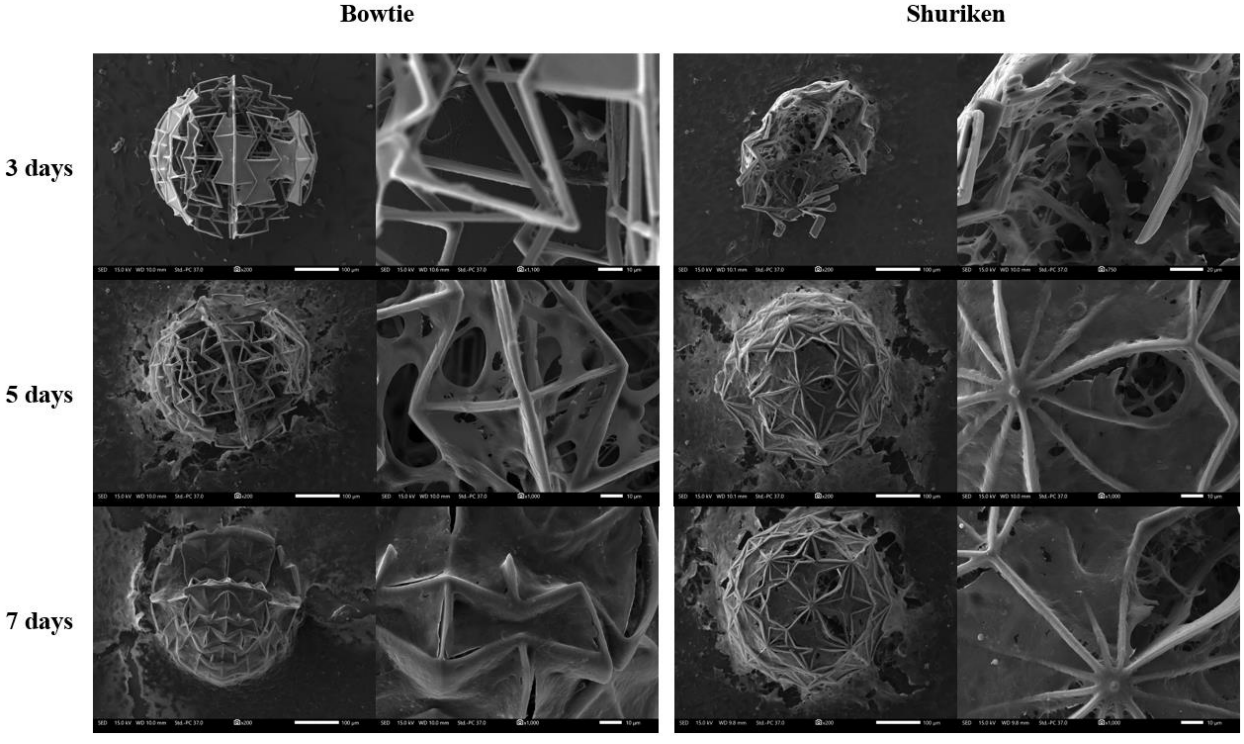

Figure 34: Images of Bowtie and Shuriken at 3, 5, and 7-day time points, captured from both a top view and a zoomed top view.

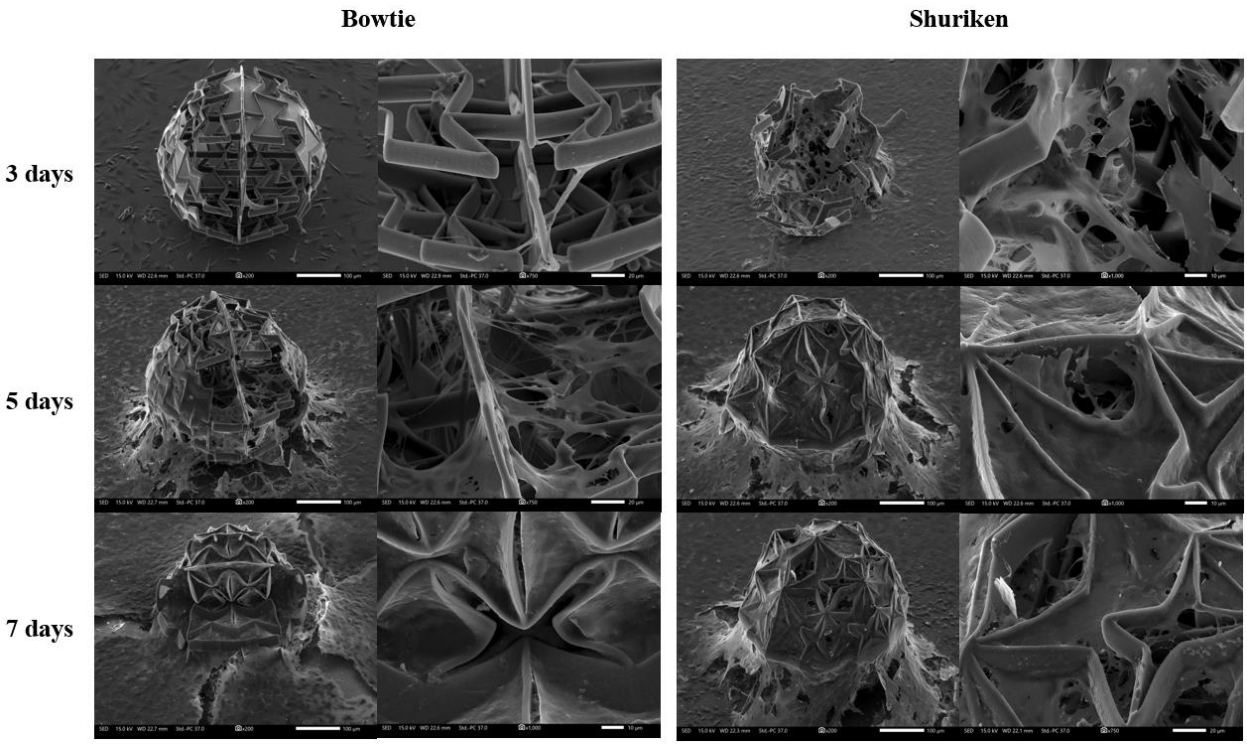

Figure 35: Images of Bowtie and Shuriken at 3, 5, and 7-day time points, captured from both a tilted view and a zoomed tilted view.

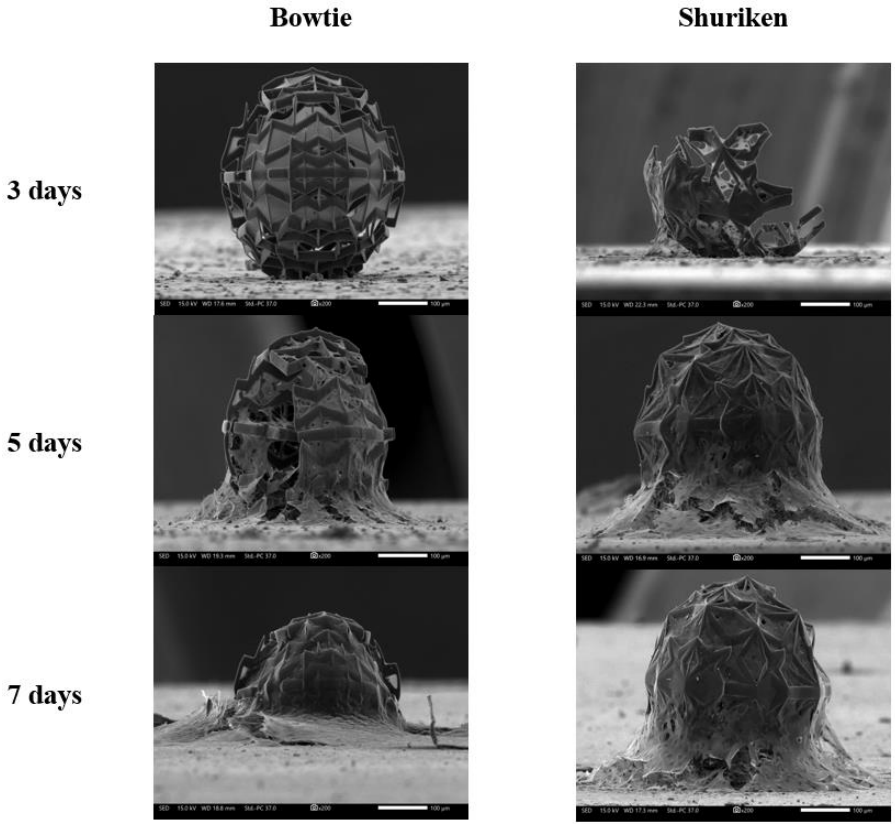

Figure 36: Images of Bowtie and Shuriken at 3, 5, and 7-day time points, captured from both a side view.

Even though the Shuriken scaffold was destroyed during the cell seeding process, the results at the 3-day time point indicate that this duration was insufficient for cells to migrate onto the scaffolds. Consequently, it has become evident that cells are capable of penetrating and migrating onto the scaffolds. The observations at the 5 and 7-day time points have yielded valuable insights and information, specifically indicating that cells can proliferate and migrate on the scaffold. This, in turn, underscores the scaffold's ability to facilitate the exchange of nutrients between the cells and the culture medium.

4.7 Live/Dead assay & DAPI

Through the live/dead assay, we were able to demonstrate that not only can cells penetrate the scaffolds, but they can also survive, exchange nutrients, and multiply within the scaffold, behaving in a manner consistent with their normal behavior.

By using DAPI, we were able to stain the cell nuclei. The blue channel corresponds to the DAPI-stained nuclei, the green channel represents the living cells, and the red channel represents the dead cells.

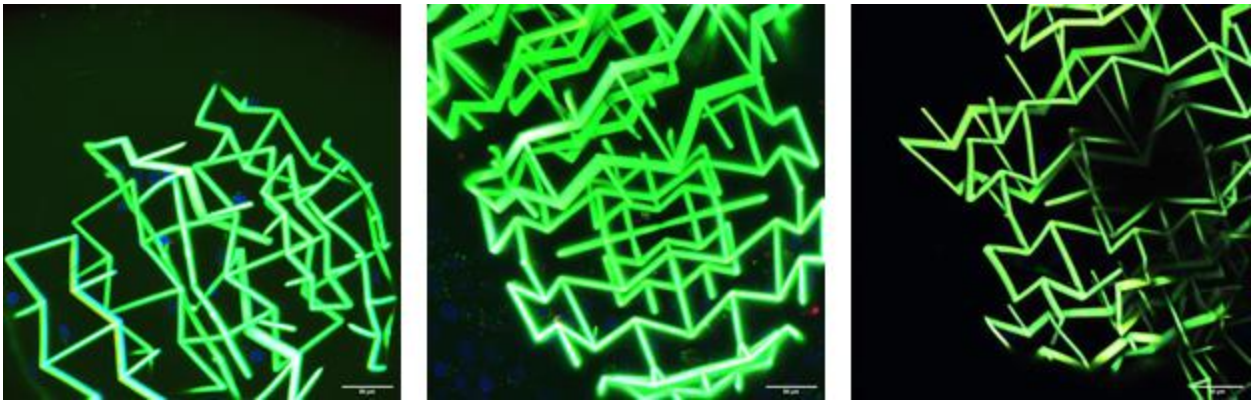

Figure 37: Confocal images of Bowtie sphere after 5 days of culture.

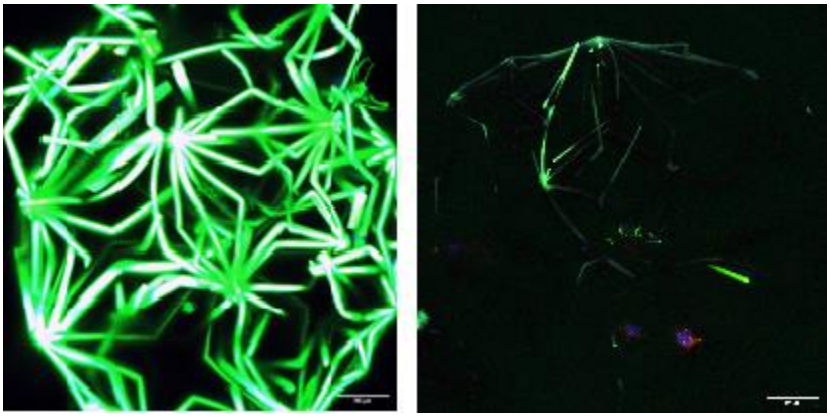

Figure 38: Confocal images of Shuriken sphere after 5 days of culture.

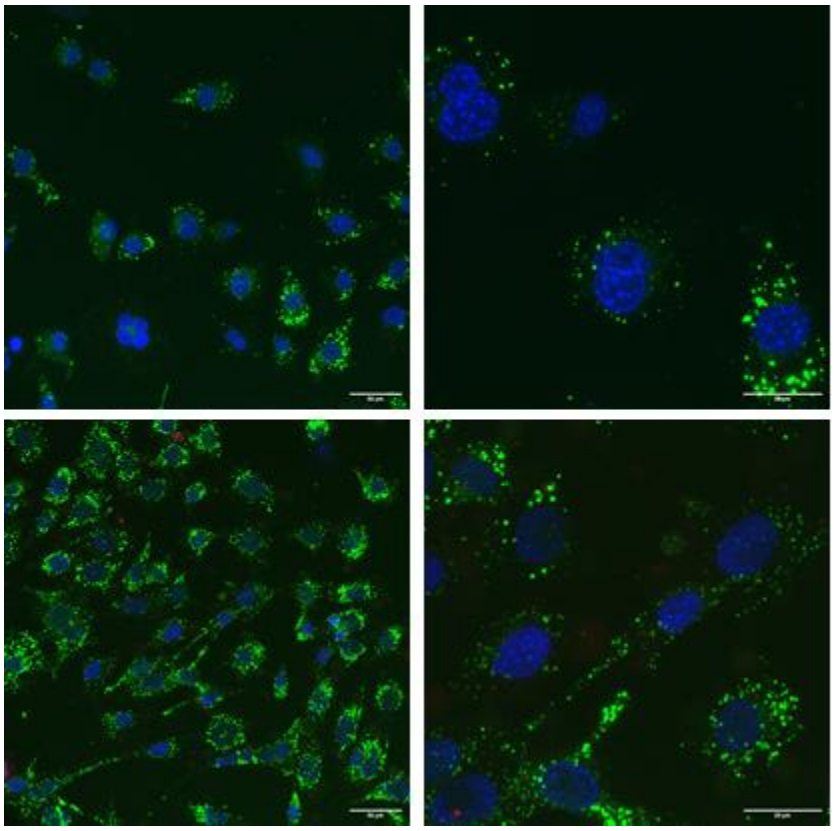

Figure 39: Confocal images of cells on glass substrate after 5 days of culture.

Figure 40: Confocal images of Bowtie sphere after 7 days of culture.

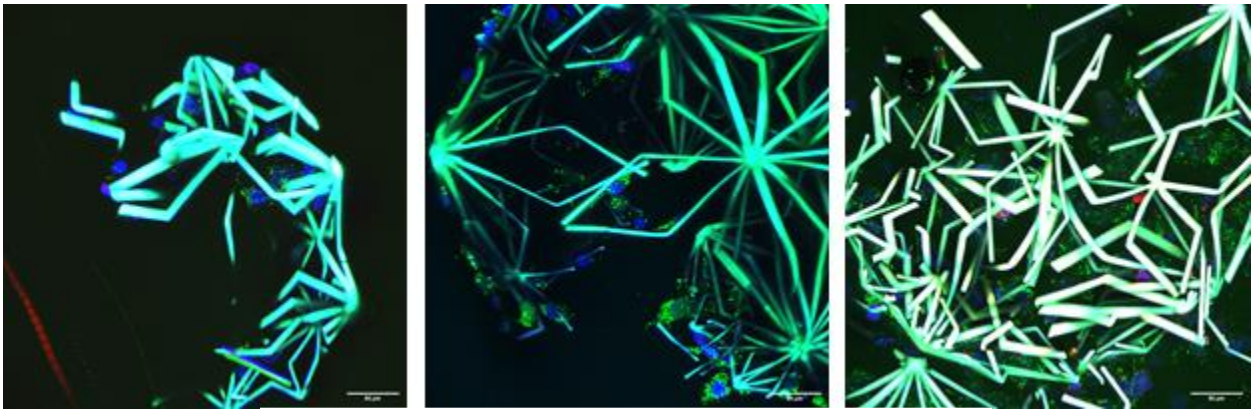

Figure 41: Confocal images of Shuriken sphere after 7 days of culture.

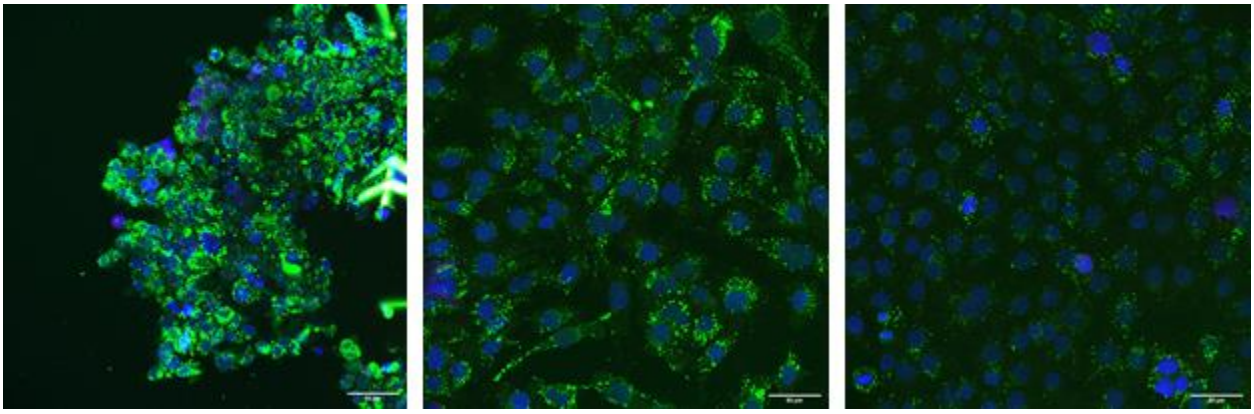

Figure 42: Confocal images of cells on glass substrate after 7 days of culture.

It was observed that the scaffold's autofluorescence in all channels was quite high, making it challenging to distinguish cells within it. However, with some minor image adjustments, we managed to identify cells at the top and middle of the scaffold. This is primarily because the scaffold has a diameter of 400μm, and it was not feasible to capture images throughout the entire structure. After 5 days, we notice a scarcity of cells in the center of the scaffold. However, at the 7-day mark, in comparison to the 5-day observation, we observe a significant increase in cell population and their migration towards the top of the scaffold. This leads to the conclusion that these scaffolds are indeed viable for tissue engineering applications, as they allow for effective nutrient exchange between the cells and the culture medium. Nevertheless, this finding demonstrates the cells' ability to effectively utilize their 3D microenvironment.

5. Conclusion

5.1 Synopsis of the thesis

The integration of metamaterials into tissue engineering is a prime example of a multidisciplinary approach, combining knowledge from physical sciences, computational modeling, and mechanical biology. Mechanical metamaterials offer distinct advantages over traditional scaffolds when it comes to exerting control over the mechanical environment of cells and tissues. This includes the ability to create enhanced cellular geometries and previously unattainable mechanical characteristics.

Poisson's ratio, for instance, has found applications in the biomedical field both in vitro and in vivo, showcasing the potential of metamaterials in biological contexts. Additionally, various remarkable mechanical properties of metamaterials, such as negative compressibility, have yet to be fully harnessed within the realm of biological sciences. This highlights the ongoing potential for innovative and transformative applications of metamaterials in the field of tissue engineering and beyond.

The central goal of this project was to create functional spherical mechanical metamaterials with the capability to demonstrate auxetic behavior, a property not commonly found in natural materials. The design process was accomplished through algorithmic engineering, which was made accessible through the use of Hyperganic's software. Hyperganic is a software platform that empowers designers and engineers to explore algorithmic engineering for the creation of advanced and customizable unit cells within metamaterials. Algorithmic engineering in unit cells involves the application of mathematical algorithms to design intricate, precisely structured building blocks that form the basis of complex metamaterials with tailored properties. This approach allowed for the development of innovative and custom-designed metamaterials with unique mechanical characteristics.

The next step involved the fabrication of these spheres using the commercially available One-Photon printer ANYCUBICTM MONO 4K. Subsequently, the fabricated spheres were subjected to optical characterization through scanning electron microscopy (SEM).

Two-photon lithography has established the foundation for constructing highly intricate microscale structures. In this study, the fabrication of spherical scaffolds has laid the groundwork for a novel category of auxetic scaffolds. Commencing at a size of 100 μm and surmounting the challenge of creating droplets with a height of 200 μm, we ultimately succeeded in fabricating spheres with a diameter of 400 μm with remarkable precision. These scaffolds have the potential to support cell growth without jeopardizing their viability due to their unique design, making them

promising candidates for various tissue engineering applications. Additionally, optical characterization of the spheres was accomplished through SEM.

Characterization techniques included an analysis of the unit cell using ANSYS 2023 R1 Student license and simulations on the mechanical behavior of 3D trusses performed by our colleague at UC Berkeley, using SolidWorks 2022. Subsequently, the spheres underwent testing using the MicroTester LT from CellScale, where two cycles were conducted to evaluate their mechanical properties. This phase allowed us to calculate the Poisson Ratio and the stiffness of the spheres.

Finally, mesenchymal stem cells (MSCs) were employed for cell seeding onto the scaffolds, and their behavior was observed at 3, 5, and 7-day intervals. At the 5 and 7-day time points, a live/dead cell evaluation was conducted simultaneously with nuclear staining. One of the fundamental challenges in this work was ensuring accurate and robust analysis of the results, given the complexity of a 3D environment. To address this challenge, a confocal microscope was utilized, enabling precise analysis by penetrating the sample to a specific depth and imaging cells through fluorescent molecules. By capturing z-stacks, these images could be combined to represent the scaffold in a 3D computer environment.

5.2 Future plans

One of my significant future plans involves the fabrication and comprehensive characterization of all the previously presented designs. This characterization will encompass not only theoretical assessments but also mechanical and optical evaluations. The goal is to investigate whether variations in the angles of Shuriken and the ratios of Bowtie can influence the Poisson ratio, potentially enhancing the negative Poisson ratio (auxetic behavior) or having a different effect.

Following that, I would like to culture the spheres with cells to reaffirm that cells can indeed thrive and grow within the scaffolds. Various staining techniques could be employed to gather additional information about the cells and how the mechanical environment might influence them. Subsequently, experiments could be conducted with differentiated cells to assess how they interact with these scaffolds. For instance, we could explore whether these scaffolds have the potential to enhance cell differentiation.

A side project involved free-standing mechanical metamaterials cultured with cells to investigate whether cells are capable of deforming the scaffolds and to calculate the cellular forces applied to them. This experiment could also be conducted with the spheres.

I would also like to explore various methods for enhancing the elasticity of the existing designs and, if successful, compare their performance.

Lastly, a microfluidic test could be conducted to further investigate how spheres behave inside microfluidic channels. This experiment could be highly intriguing and may serve as a strong proof of concept for injectable spherical mechanical metamaterials.

6. References

1. Pendry, J. B. *Ci, 42.30.Wb, 73.20.Mf, 78*. vol. 66 (2000).
2. Vasanth Sathiyakumar, A Alex Jahangir, Hassan R Mir, William T Obremskey, Young M Lee, Rachel V Thakore, M. K. S. Patterns of costs and spending among orthopedic surgeons across the United States: a national survey - PubMed. https://pubmed.ncbi.nlm.nih.gov/24490192/.
3. Malik, I. V *et al.* Estimation of Expenditure and Challenges Related to Rehabilitation After Knee Arthroplasty: A Hospital-Based Cross-Sectional Study. *Indian J. Orthop.* **55**, 1317–1325 (2021).
4. Zadpoor Meta-biomaterials, A. A. & Zadpoor, A. A. Biomaterials Science REVIEW Meta-biomaterials. *Cite this Biomater. Sci* **8**, 18 (2020).
5. Wegener, M. Metamaterials Beyond Optics. *Science (80-.).* **342**, 939–940 (2013).
6. Bückmann, T. *et al.* Tailored 3D Mechanical Metamaterials Made by Dip-in Direct-Laser-Writing Optical Lithography. *Adv. Mater* **24**, 2710–2714 (2012).
7. Harris, L. D., Kim, B.-S. & Mooney, D. J. Open pore biodegradable matrices formed with gas foaming. (1998) doi:10.1002/(SICI)1097-4636(19981205)42:3<396::AID-JBM7>3.0.CO;2-E.
8. Yu Lin, C., Kikuchi, N. & Hollister, S. J. A novel method for biomaterial scaffold internal architecture design to match bone elastic properties with desired porosity. *J. Biomech.* **37**, 623–636 (2004).
9. Chen, V. J. & Ma, P. X. Nano-fibrous poly(l-lactic acid) scaffolds with interconnected spherical macropores. *Biomaterials* **25**, 2065–2073 (2004).
10. Critchley, R. *et al.* The preparation of auxetic foams by three-dimensional printing and their characteristics. *Adv. Eng. Mater.* **15**, 980–985 (2013).
11. Amin Yavari, S. *et al.* Relationship between unit cell type and porosity and the fatigue behavior of selective laser melted meta-biomaterials. *J. Mech. Behav. Biomed. Mater.* **43**, 91–100 (2015).
12. Zheng, X. *et al.* Multiscale metallic metamaterials. *Nat. Mater. 2016 1510* **15**, 1100–1106 (2016).
13. Martínez, J. *et al.* Star-shaped metrics for mechanical metamaterial design. *ACM Trans. Graph.* **38**, (2019).
14. Béduer, A. *et al.* An Injectable Meta-Biomaterial: From Design and Simulation to In Vivo Shaping and Tissue Induction. *Adv. Mater.* **33**, (2021).

15. Yuan, B. *et al.* Machine-Learning-Based Monitoring of Laser Powder Bed Fusion. *Adv. Mater. Technol.* **3**, (2018).

16. Obata, K., El-Tamer, A., Koch, L., Hinze, U. & Chichkov, B. N. High-aspect 3D two-photon polymerization structuring with widened objective working range (WOW-2PP). *Light Sci. Appl. 2013 212* **2**, e116–e116 (2013).

17. Ge, Q. *et al.* Multimaterial 4D Printing with Tailorable Shape Memory Polymers. *Sci. Reports 2016 61* **6**, 1–11 (2016).

18. Dogan, E., Bhusal, A., Cecen, B. & Miri, A. K. 3D Printing metamaterials towards tissue engineering. *Appl. Mater. Today* **20**, 100752 (2020).

19. Zheng, X. *et al.* Multiscale metallic metamaterials. **15**, (2016).

20. Maruo, S. & Ikuta, K. Three-dimensional microfabrication by use of single-photon-absorbed polymerization. *Appl. Phys. Lett.* **76**, 2656–2658 (2000).

21. Fischer, J. & Wegener, M. Three-dimensional optical laser lithography beyond the diffraction limit. *Laser Photon. Rev.* **7**, 22–44 (2013).

22. Jain, K., Rice, S., Jose, S. & Lin, B. J. Ultrafast Deep UV Lithography Using Excimer Lasers. 1019–1021 (1983).

23. Farsari, M., Vamvakaki, M. & Chichkov, B. N. Multiphoton polymerization of hybrid materials. *J. Opt.* **12**, (2010).

24. Lee, K.-S., Yang, D.-Y., Park, S. H. & Kim, R. H. Review Recent developments in the use of two-photon polymerization in precise 2D and 3D microfabrications {. (2006) doi:10.1002/pat.664.

25. Maruo, S., Kawata, S. & Nakamura, O. Three-dimensional microfabrication with two-photon-absorbed photopolymerization. *Opt. Lett. Vol. 22, Issue 2, pp. 132-134* **22**, 132–134 (1997).

26. Juodkazis, S., Mizeikis, V. & Misawa, H. Three-dimensional microfabrication of materials by femtosecond lasers for photonics applications. *J. Appl. Phys.* **106**, (2009).

27. Sakellari, I. *et al.* Diffusion-assisted high-resolution direct femtosecond laser writing. *ACS Nano* **6**, 2302–2311 (2012).

28. Sakellari, I. *et al.* Two-photon polymerization of titanium-containing sol–gel composites for three-dimensional structure fabrication. *Appl. Phys. A* **100**, 359–364 (2010).

29. Kabouraki, E. *et al.* Redox Multiphoton Polymerization for 3D Nanofabrication. *Nano Lett* **13**, (2013).

30. Amato, L. *et al.* Integrated three-dimensional filter separates nanoscale from microscale elements in a microfluidic chip. *Lab Chip* **12**, 1135–1142 (2012).

31. Schizas, C. *et al.* On the design and fabrication by two-photon polymerization of a readily assembled micro-valve. doi:10.1007/s00170-009-2320-4.

32. Galanopoulos, S. *et al.* Design, Fabrication and Computational Characterization of a 3D Micro-Valve Built by Multi-Photon Polymerization. *Micromachines 2014, Vol. 5, Pages 505-514* **5**, 505–514 (2014).

33. Melissinaki, V. *et al.* Direct laser writing of 3D scaffolds for neural tissue engineering applications. *Biofabrication* **3**, (2011).

34. Raimondi, M. T. *et al.* Two-Photon Laser Polymerization: From Fundamentals to Biomedical Application in Tissue Engineering and Regenerative Medicine. *https://doi.org/10.5301/JABFM.2012.9278* **10**, 56–66 (2018).

35. Ovsianikov, A. *et al.* Laser fabrication of three-dimensional CAD scaffolds from photosensitive gelatin for applications in tissue engineering. *Biomacromolecules* **12**, 851–858 (2011).

36. Danilevicius, P. *et al.* The effect of porosity on cell ingrowth into accurately defined, laser-made, polylactide-based 3D scaffolds. *Appl. Surf. Sci.* **336**, 2–10 (2015).

37. Malinauskas, M. & Baltriukiene, D. 3D ARTIFICIAL POLYMERIC SCAFFOLDS FOR STEM CELL GROWTH FABRICATED BY FEMTOSECOND LASER. *Lith. J. Phys.* (2010).

38. Torgersen, J. *et al.* Photo-sensitive hydrogels for three-dimensional laser microfabrication in the presence of whole organisms. *J. Biomed. Opt.* **17**, 1 (2012).

39. König, N. *et al.* Optimization of hybrid polymer materials for 2PP and fabrication of individually designed hybrid microoptical elements thereof. *Opt. Mater. Express, Vol. 5, Issue 2, pp. 456-461* **5**, 456–461 (2015).

40. Reinhardt, C. ; *et al.* Laser-fabricated dielectric optical components for surface plasmon polaritons. *Opt. Lett.* **31**, 2023 (2006).

41. Göppert-Mayer. Elementarakte mit xwei QuantemspWwgem Von M a r i a G 6 p p e r t-M a y e r. doi:10.1002/andp.19314010303.

42. Botcherby, E. J. *et al.* Aberration-free three-dimensional multiphoton imaging of neuronal activity at kHz rates. *Proc. Natl. Acad. Sci. U. S. A.* **109**, 2919–2924 (2012).

43. Skliutas, E. *et al.* Polymerization mechanisms initiated by spatio-temporally confined light. *Nanophotonics* **10**, 1211–1242 (2021).

44. Li, L. & Fourkas, J. T. Multiphoton polymerization. *Mater. Today* **10**, 30–37 (2007).

45. Wang, H. *et al.* Two-Photon Polymerization Lithography for Optics and Photonics: Fundamentals, Materials, Technologies, and Applications. *Adv. Funct. Mater.* **2214211**, 1–51 (2023).

46. Kshetrimayum, R. S. A brief intro to metamaterials. *IEEE Potentials* **23**, 44–46 (2004).

47. Surjadi, J. U. *et al.* Mechanical Metamaterials and Their Engineering Applications. **1800864**, 1–37 (2019).

48. Kelkar, P. U. *et al.* Cellular Auxetic Structures for Mechanical Metamaterials : A Review. 1–26.

49. Drakakis, T. S. *et al.* Construction of three-dimensional biomolecule structures employing femtosecond lasers Construction of three-dimensional biomolecule structures employing femtosecond lasers. **144108**, 1–4 (2012).

50. Psycharakis, S., Tosca, A. & Melissinaki, V. Tailor-made three-dimensional hybrid scaffolds for cell cultures. **045008**,.

51. Xing, J., Zheng, M. & Duan, X. Chem Soc Rev hydrogels : an advanced 3D printing technology for tissue engineering and drug delivery. *Chem. Soc. Rev.* (2015) doi:10.1039/C5CS00278H.

52. Gru, P. A. Exchange anisotropy , interlayer exchange coupling and GMR in research and application. **91**, 153–160 (2001).

53. Niarchos, D. Magnetic MEMS : key issues and some applications ☪. **109**, 166–173 (2003).

54. Herrera-may, A. L., Aguilera-cortés, L. A., García-ramírez, P. J. & Manjarrez, E. Resonant Magnetic Field Sensors Based On MEMS Technology. 7785–7813 (2009) doi:10.3390/s91007785.

55. Myung, N. V, Park, D., Yoo, B. & Sumodjo, P. T. A. Development of electroplated magnetic materials for MEMS. **265**, 189–198 (2003).

56. Schiavone, G., Desmulliez, M. P. Y. & Walton, A. J. Integrated Magnetic MEMS Relays : Status of the Technology. 622–653 (2014) doi:10.3390/mi5030622.

57. Bolshakova, I. Magnetic rnicrosensors : technology , properties , application. **68**, 282–285 (1998).

58. Chin, T. Permanent magnet " lms for applications in microelectromechanical systems. **209**, 6–10 (2000).

59. Valdevit, L., Jacobsen, A. J., Greer, J. R. & Carter, W. B. From Hypersonics to Micro-Architected Materials. **20**, 1–20 (2011).

60. Sarlis, A. A. *et al.* Negative Stiffness Device for Seismic Protection of Structures. 1124–1133 (2013) doi:10.1061/(ASCE)ST.1943-541X.0000616.

61. Schaedler, B. T. A. *et al.* Designing Metallic Microlattices for Energy Absorber Applications **. 276–283 (2014) doi:10.1002/adem.201300206.

62. Manuscript, A. Biomaterials Science. (2020) doi:10.1039/C9BM01928F.

63. Arcaute, K., Mann, B. & Wicker, R. Acta Biomaterialia Stereolithography of spatially controlled multi-material bioactive poly (ethylene glycol) scaffolds. *Acta Biomater.* **6**, 1047–1054 (2010).

64. Kadic, M., Bückmann, T., Stenger, N., Thiel, M. & Wegener, M. On the practicability of

pentamode mechanical metamaterials On the practicability of pentamode mechanical metamaterials. **191901**, (2012).

65. Thiel, M., Kadic, M., Schittny, R. & Wegener, M. An elasto-mechanical unfeelability cloak made of pentamode metamaterials. 1–6 (2014) doi:10.1038/ncomms5130.

66. Christensen, J., Fotonik, D. T. U., Engineering, P. & Lyngby, D.-K. Vibrant times for mechanical metamaterials. **5**, 453–462 (2015).

67. Baughman, R. H., Baughman, R. H. & Stafstro, S. Materials with Negative Compressibilities in One or More Dimensions. **1522**, (2012).

68. Nicolaou, Z. G. & Motter, A. E. compressibility transitions. *Nat. Mater.* **11**, 1–6 (2012).

69. Gatt, R. & Grima, J. N. Negative compressibility pss. **238**, 236–238 (2008).

70. Zheng, X. *et al.* Ultralight, ultrastiff mechanical metamaterials. *Science (80-.).* **344**, 1373–1377 (2014).

71. Meza, L. R. No Title. **1322**, (2014).

72. Evans, K. E. Auxetic polymers: a new range of materials. *Endeavour* **15**, 170–174 (1991).

73. Kolken, H. M. A. & Zadpoor, A. A. Auxetic mechanical metamaterials. *RSC Adv.* **7**, 5111–5129 (2017).

74. Lakes, R., Variability, N., Physcss, A., Meteorolgica, W. & Symposium, O. Lakes1987-1. *Science (80-.).* **235**, 1038–1041 (1987).

75. Evans, K. E. & Alderson, A. Auxetic materials: Functional materials and structures from lateral thinking! *Adv. Mater.* **12**, 617–628 (2000).

76. Milton, G. W. Composite materials with poisson's ratios close to - 1. *J. Mech. Phys. Solids* **40**, 1105–1137 (1992).

77. Prall, D. & Lakes, R. S. Properties of chiral honeycombe with Poisson's ratio of -1. *Int. J. Mech. Sci* **39**, (1997).

78. Stents, A. (12) Patent Application Publication (10) Pub . No .: US 2011 / 0029063 A1. **1**, (2011).

79. Ali, M. N. & Ur, I. An Auxetic structure configured as oesophageal stent with potential to be used for palliative treatment of oesophageal cancer ; development and in vitro mechanical analysis. 2573–2581 (2011) doi:10.1007/s10856-011-4436-y.

80. Najabat, M., James, A. & Rehman, I. U. Auxetic oesophageal stents : structure and mechanical properties. 527–553 (2014) doi:10.1007/s10856-013-5067-2.

81. Geng, L. C., Ruan, X. L., Wu, W. W., Xia, R. & Fang, D. N. Mechanical Properties of Selective Laser Sintering (SLS) Additive Manufactured Chiral Auxetic Cylindrical Stent. (2019).

82. Mir, M., Ali, M. N., Sami, J. & Ansari, U. Review of Mechanics and Applications of

Auxetic Structures. **2014**, 1–18 (2014).

83. Zhu, Y. *et al.* Stimuli-Responsive Controlled Drug Release from a Hollow Mesoporous Silica Sphere/Polyelectrolyte Multilayer Core–Shell Structure. *Angew. Chemie Int. Ed.* **44**, 5083–5087 (2005).

84. Ren, N. *et al.* Mesoporous microcapsules with noble metal or noble metal oxide shells and their application in electrocatalysis. *J. Mater. Chem.* **14**, 3548–3552 (2004).

85. Hao, E. *et al.* Optical properties of metal nanoshells. *J. Phys. Chem. B* **108**, 1224–1229 (2004).

86. Martinez, C. J., Hockey, B., Montgomery, C. B. & Semancik, S. Porous tin oxide nanostructured microspheres for sensor applications. *Langmuir* **21**, 7937–7944 (2005).

87. Stuart RD (1963). Polyhedral and Mosaic Transformations (Student Publications of the School of Design, North Carolina State University, Raleigh, NC). https://d.lib.ncsu.edu/collections/catalog/ua110_200-003-cn0027-v12n1.

88. Joseph Clinton, A. D. Advanced structural geometry studies. Part 2: A geometric transformation concept for expanding rigid structures. (1971).

89. Verheyen, H. F. *THE COMPLETE SET OF JITTERBUG TRANSFORMERS AND THE ANALYSIS OF THEIR MOTION*. *Computers Math. Applic* vol. 17 (1989).

90. Shim, J., Perdigou, C., Chen, E. R., Bertoldi, K. & Reis, P. M. Buckling-induced encapsulation of structured elastic shells under pressure. *Proc. Natl. Acad. Sci. U. S. A.* **109**, 5978–5983 (2012).

91. Babaee, S. *et al.* 3D soft metamaterials with negative poisson's ratio. *Adv. Mater.* **25**, 5044–5049 (2013).

92. Li, Y., Shen, Y., Cao, S., Zhang, X. & Meng, Y. Thermally triggered tunable vibration mitigation in Hoberman spherical lattice metamaterials. *Appl. Phys. Lett.* **114**, (2019).

93. Li, Y., Cao, S., Shen, Y. & Meng, Y. Phononic band-gaps of Hoberman spherical metamaterials in low frequencies. *Mater. Des.* **181**, 107935 (2019).

94. Lu, X. *et al.* Triple tunability of phononic bandgaps for three-dimensional printed hollow sphere lattice metamaterials. *Int. J. Mech. Sci.* **221**, 107166 (2022).

95. Turek, V. A. *et al.* Self-Assembled Spherical Supercluster Metamaterials from Nanoscale Building Blocks. *ACS Photonics* **3**, 35–42 (2016).

96. Fomby, P. *et al.* Stem cells and cell therapies in lung biology and diseases: Conference report. *Ann. Am. Thorac. Soc.* **12**, 181–204 (2010).

97. Mason, C. & Dunnill, P. A brief definition of regenerative medicine. *Regen. Med.* **3**, 1–5 (2008).

98. Berg, J. M., Tymoczko, J. L., Gatto, G. J. & Stryer, L. *Βιοχημεία*. (Πανεπιστημιακές Εκδόσεις Κρήτης, 2015).

99. *Janeway's Immunobiology*. (Garland Science, 2007).

100. Green, J. J. Immunoengineering has arrived. *J. Biomed. Mater. Res. - Part A* **109**, 397–403 (2021).

101. Jiang, N. Immune engineering: From systems immunology to engineering immunity. *Curr. Opin. Biomed. Eng.* **1**, 54–62 (2017).

102. Langer, R. & Vacanti, J. P. Tissue Engineering. *Science (80-.).* **260**, 920–926 (1993).

103. Gaharwar, A. K., Singh, I. & Khademhosseini, A. Engineered biomaterials for in situ tissue regeneration. *Nat. Rev. Mater. 2020 59* **5**, 686–705 (2020).

104. Engler, A. J., Sen, S., Sweeney, H. L. & Discher, D. E. Matrix Elasticity Directs Stem Cell Lineage Specification. *Cell* **126**, 677–689 (2006).

105. Reilly, G. C. & Engler, A. J. Intrinsic extracellular matrix properties regulate stem cell differentiation. *J. Biomech.* **43**, 55–62 (2010).

106. Griffin, D. R., Weaver, W. M., Scumpia, P. O., Di Carlo, D. & Segura, T. Accelerated wound healing by injectable microporous gel scaffolds assembled from annealed building blocks. *Nat. Mater. 2014 147* **14**, 737–744 (2015).

107. Viswanathan, P. *et al.* 3D surface topology guides stem cell adhesion and differentiation. *Biomaterials* **52**, 140–147 (2015).

108. Ovsianikov, A. *et al.* Ultra-low shrinkage hybrid photosensitive material for two-photon polymerization microfabrication. *ACS Nano* **2**, 2257–2262 (2008).

109. Farsari, M. & Chichkov, B. N. Two-photon fabrication. *Nat. Photonics 2009 38* **3**, 450–452 (2009).

110. Colombani, D. Chain-growth control in free radical polymerization. *Prog. Polym. Sci.* **22**, 1649–1720 (1997).

111. Ladika, D. *et al.* Synthesis and application of triphenylamine-based aldehydes as photo-initiators for multi-photon lithography. *ApPhA* **128**, 745 (2022).

112. Scheps, R. & Myers, J. F. Performance of a diode-pumped laser repetitively Q-switched with a mechanical shutte DistributionI Availability Codes Avail and/or. 663–2680.

113. PAPAMAKARIOS, S. Fabrication of 3D low THz metamaterials via 2-Photon Polymerization. *Master Thesis* (2023).

114. Caplan, A. I. Mesenchymal Stem Cells: Time to Change the Name! *Stem Cells Transl. Med.* **6**, 1445–1451 (2017).

115. Ullah, I., Subbarao, R. B. & Rho, G. J. Human mesenchymal stem cells - Current trends and future prospective. *Biosci. Rep.* **35**, 191 (2015).

116. Hass, R., Kasper, C., Böhm, S. & Jacobs, R. Different populations and sources of human mesenchymal stem cells (MSC): A comparison of adult and neonatal tissue-derived MSC. *Cell Commun. Signal.* **9**, 1–14 (2011).

117. Witwer, K. W. *et al.* Defining mesenchymal stromal cell (MSC)-derived small extracellular vesicles for therapeutic applications. *J. Extracell. Vesicles* **8**, 1609206 (2019).

118. Braet, F., De Zanger, R. & Wisse, E. Drying cells for SEM, AFM and TEM by hexamethyldisilazane: A study on hepatic endothelial cells. *J. Microsc.* **186**, 84–87 (1997).

7. Appendix

Appendix A

```
latS = OpenModelFile(C:\Users\Stavros\Documents\dxf\bowtie1-15.dxf);

latS = SetRadius(LatS, 0.5);

geoSphere = OpenModelFile(C:\Users\Stavros\Documents\Έγγραφα\Διπλωματική\sphere.stl);
geoSphere = SetScale(geoSphere, vector(0.49,0.49,0.49));
denSphere = Voxelize(geoSphere);

//latSphere = LatticeFill(latS, denSphere, 1);
latSphere = LatticeFillAdaptive(latS, denSphere, 2,1,true);
latSphere = SetRadius(latSphere, 0.3);
PreviewGeometry(latCube, false, false, KIWI);

denSphere = Voxelize(latSphere);
Return(0, denSphere);
```

Figure 43: Example code that have been used for the design of the spheres.

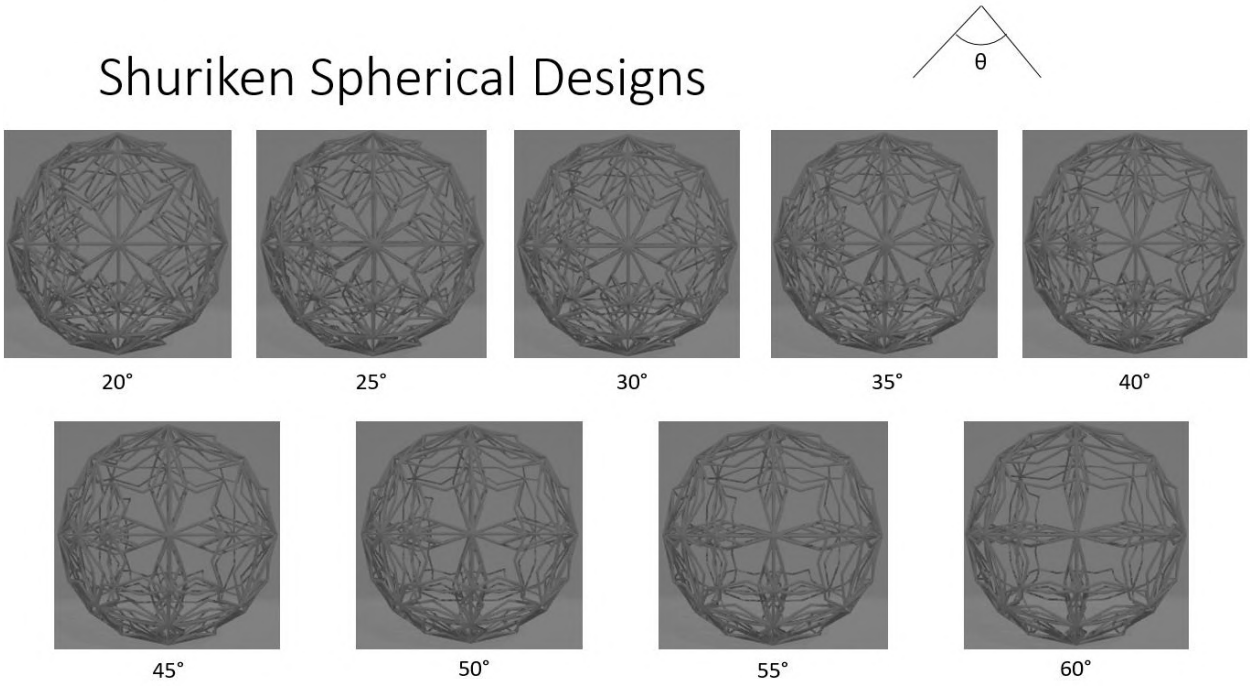

Figure 44: Various designs of Shuriken sphere.

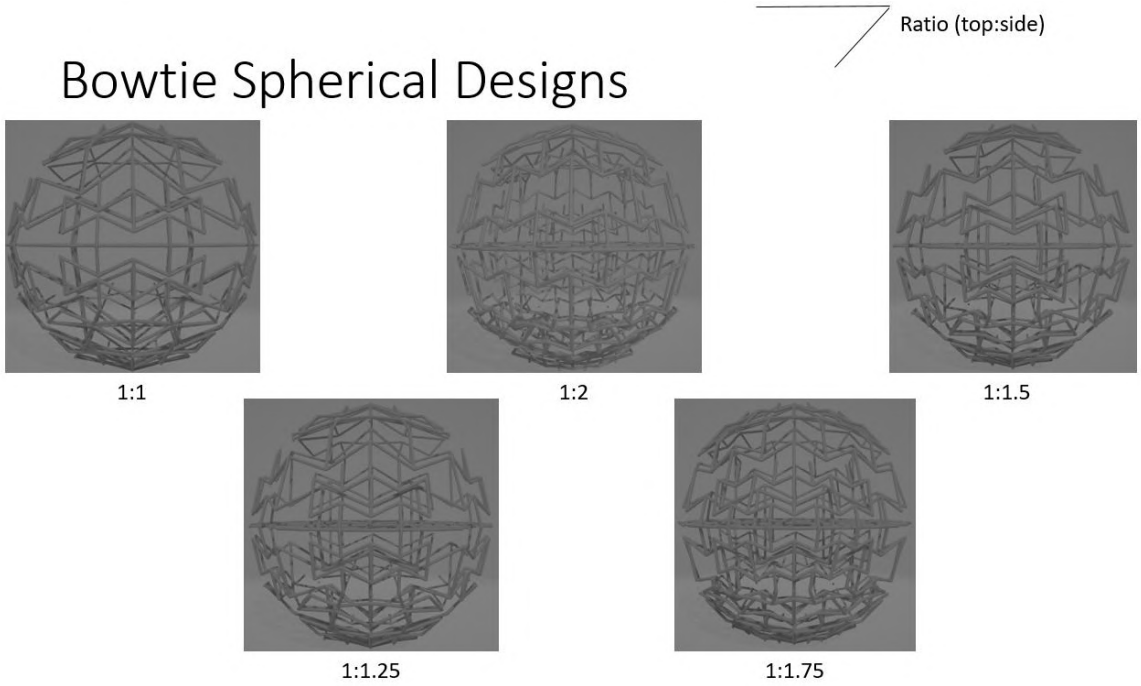

Figure 45: Various designs of Bowtie sphere.

Appendix B

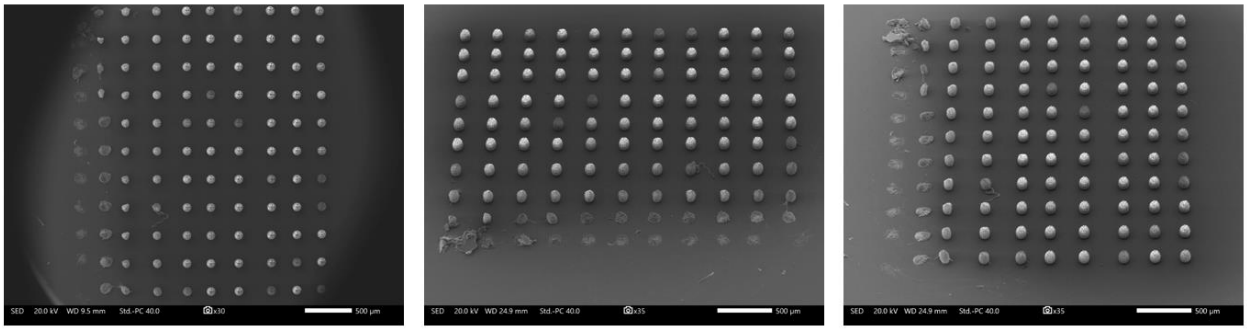

Figure 46: General view

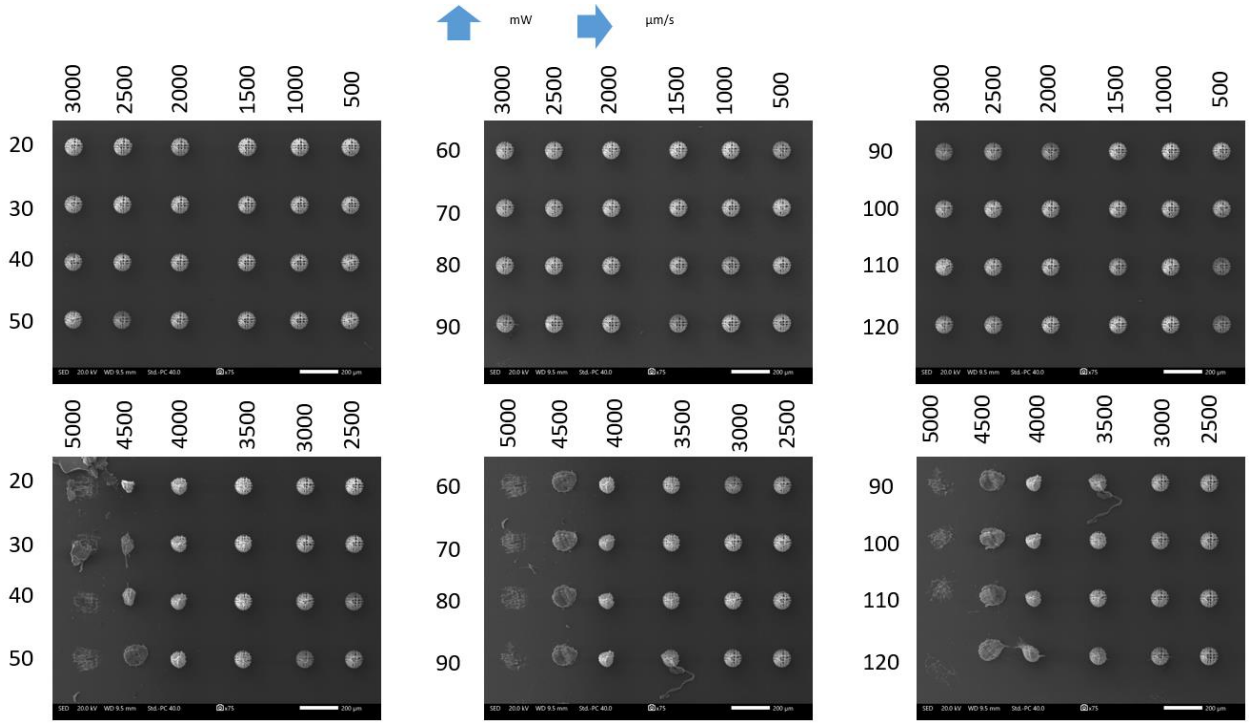

Figure 47: Closer view with each sphere's parameters.

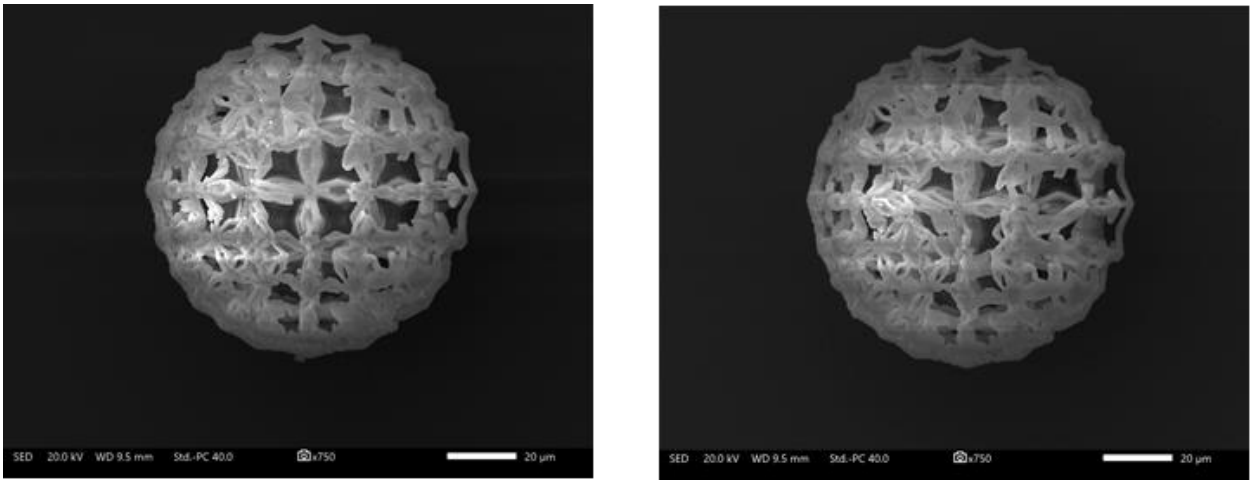

FIGURE 48: CLOSE VIEW TO 100UM SPHERES.

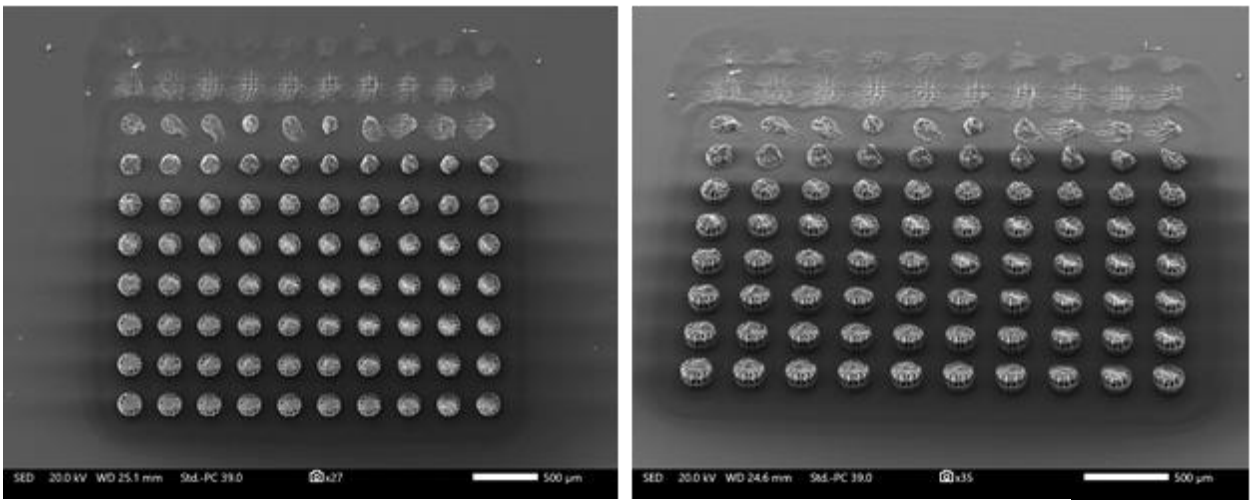

FIGURE 49: UNSUCCESSFUL FABRICATION OF SPHERES DUE TO A LACK OF PROPER DROPLET HEIGHT

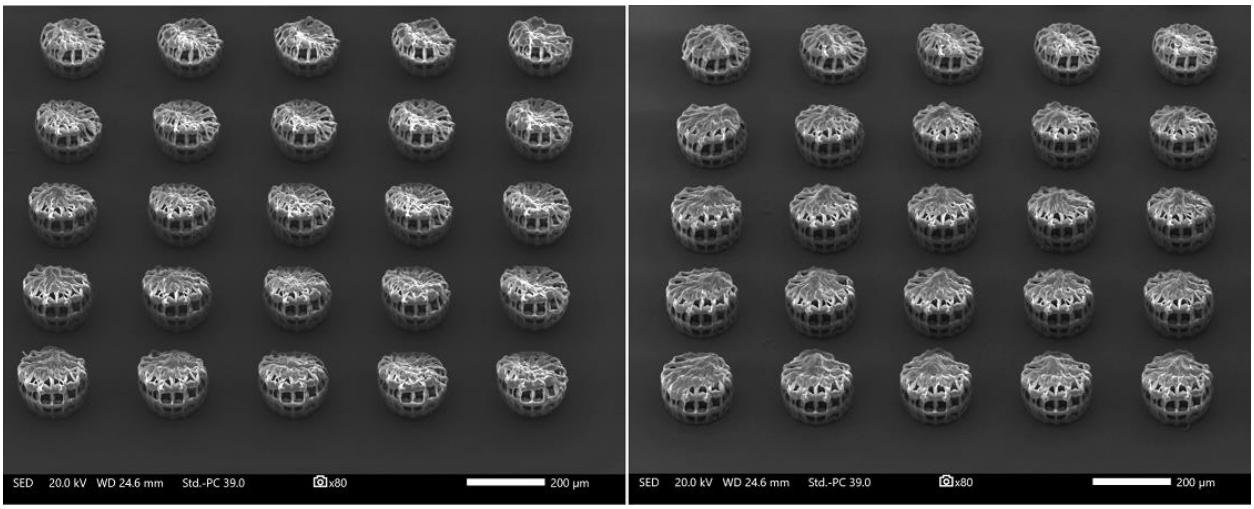

Figure 50: Closer view to unsuccessful fabrication of spheres due to a lack of proper droplet height.

Appendix C

Properties of Outline Row 3: Resin Epoxy

	A	B	C
1	Property	Value	Unit
2	Density	1160	kg m^-3
3	Isotropic Elasticity		
4	Derive from	Young's ...	
5	Young's Modulus	3.78E+09	Pa
6	Poisson's Ratio	0.35	
7	Bulk Modulus	4.2E+09	Pa
8	Shear Modulus	1.4E+09	Pa
9	Tensile Yield Strength	5.46E+07	Pa

Figure 51: Mechanical properties of Resin Epoxy.

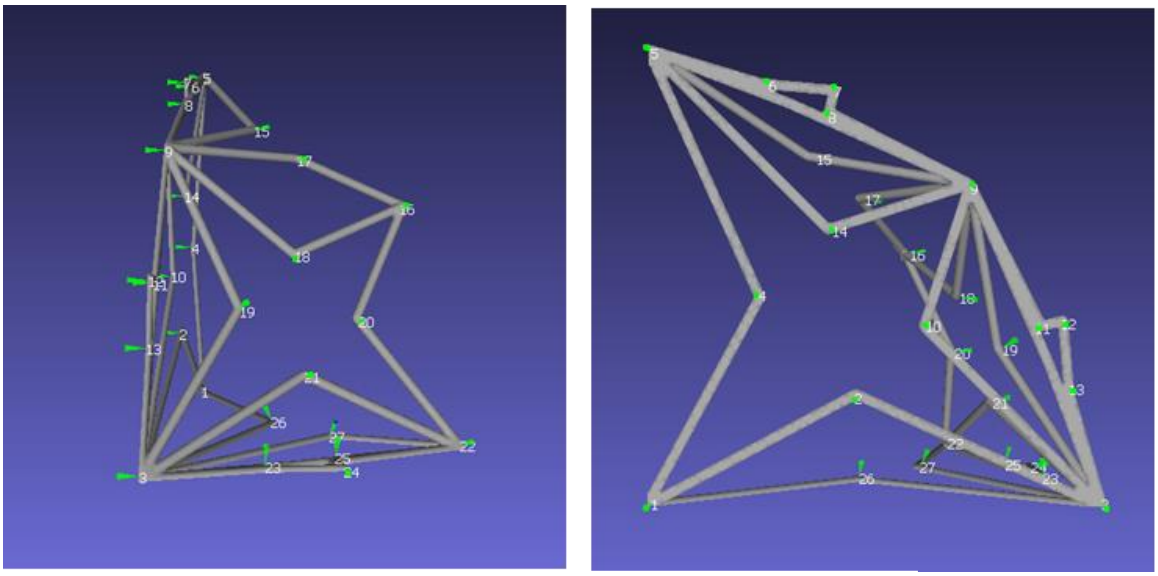

Figure 52: Numbered junction points on Shuriken30 scaffold

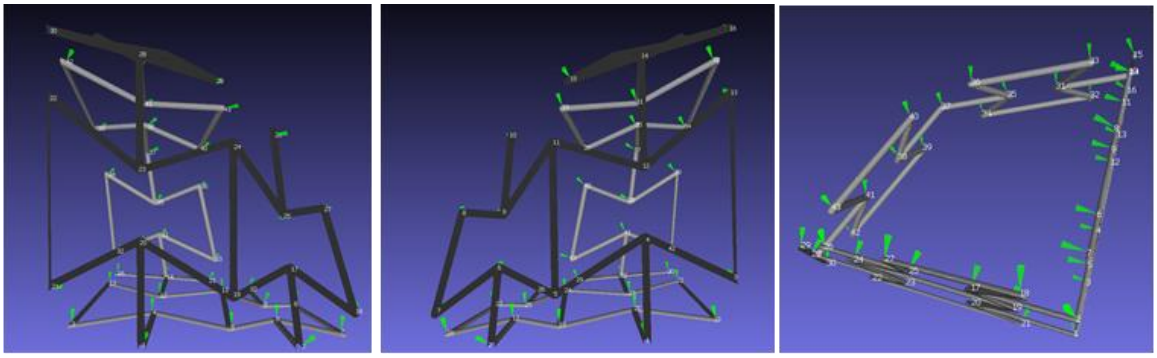

FIGURE 53: NUMBERED JUNCTION POINTS ON BOWTIE1:1.5 TRUSS

Appendix D

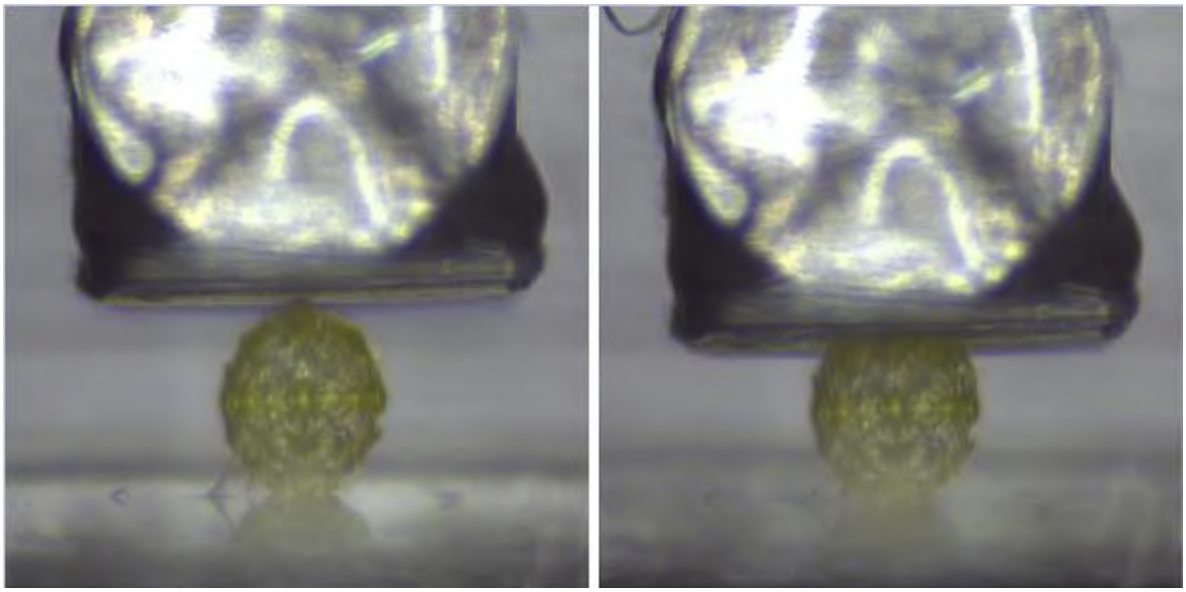

Figure 54: Shuriken sphere compressed by 25% or 100µm.

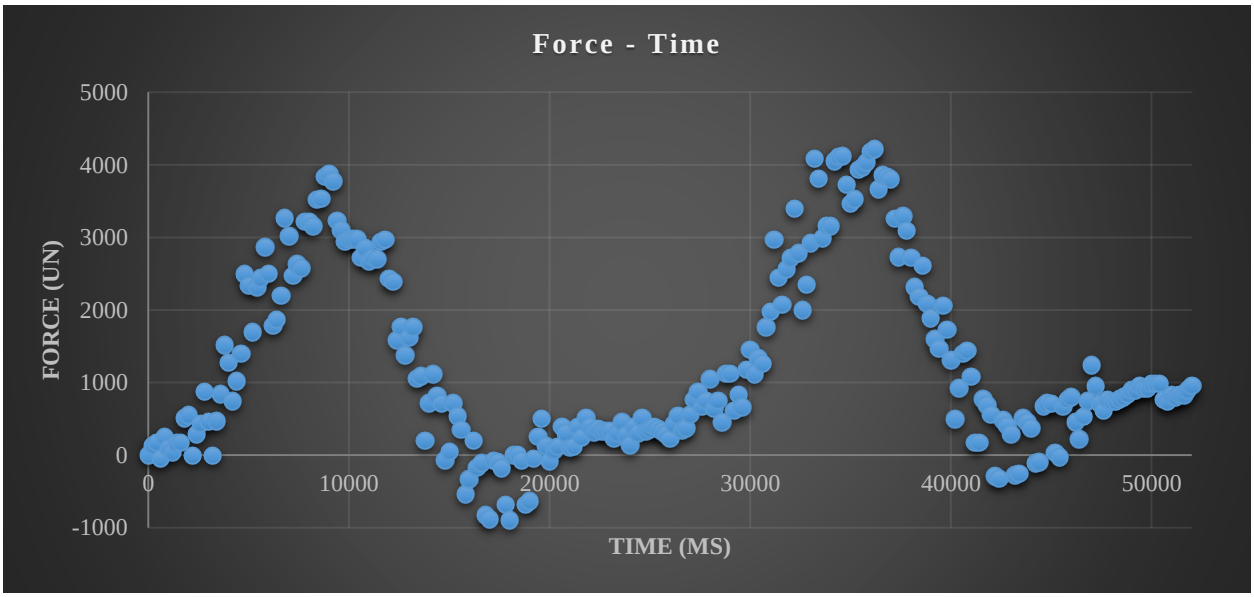

Figure 55: Force – Time plot on Shuriken sphere compressed by 25% or 100µm.

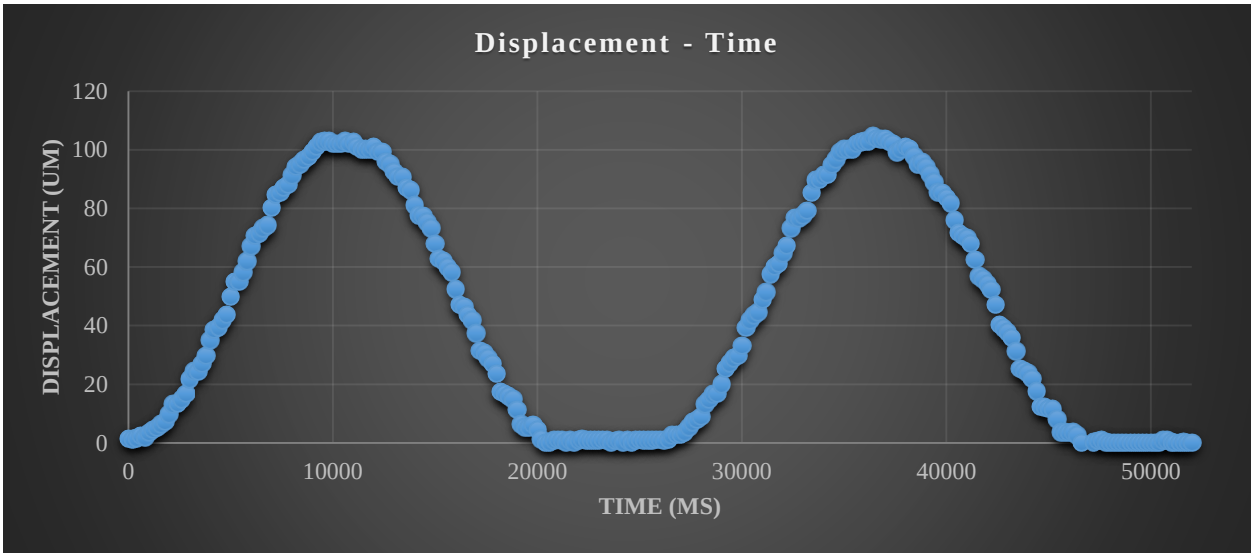

Figure 56: Displacement – Time plot on Shuriken sphere compressed by 25% or 100μm.

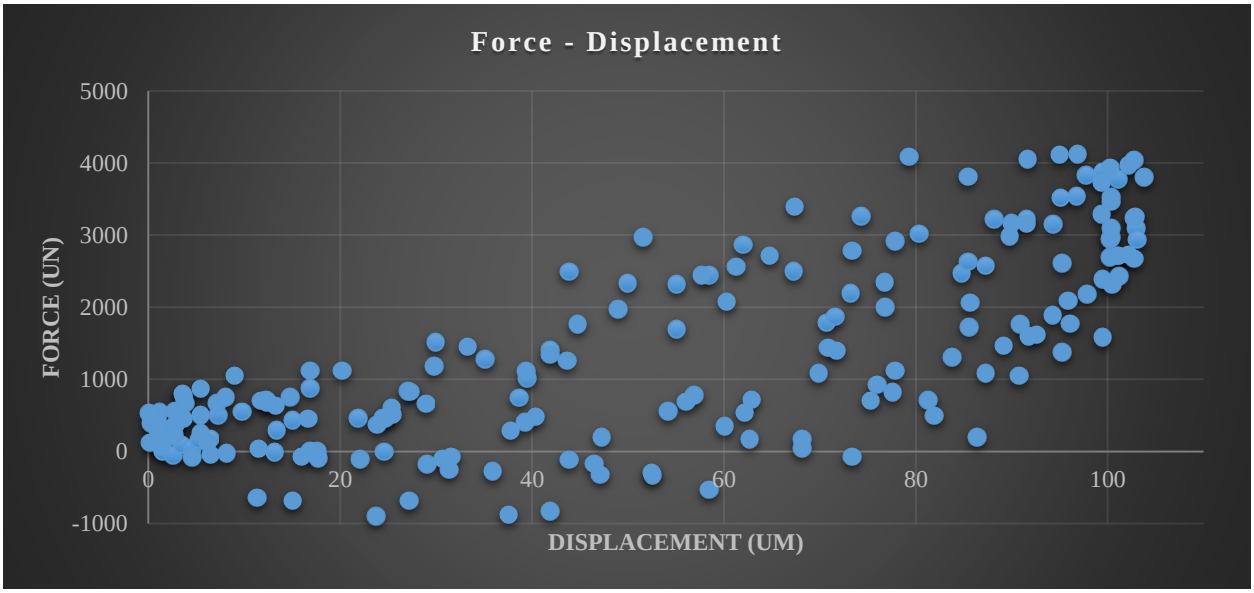

Figure 57: Force – Displacement plot on Shuriken sphere compressed by 25% or 100μm.

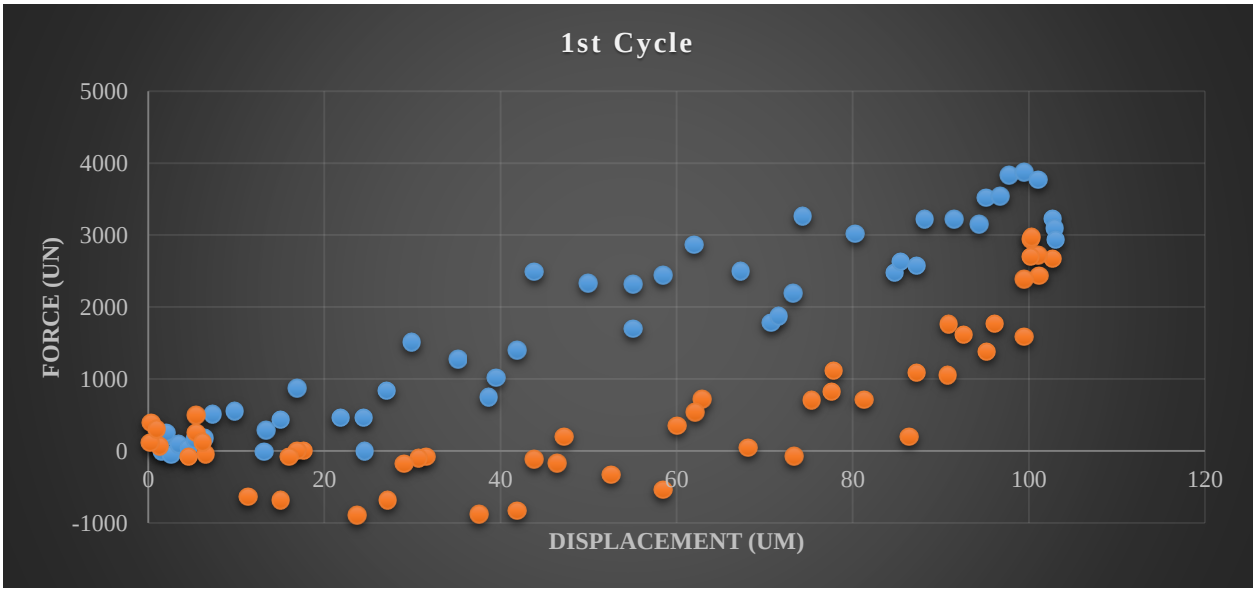

Figure 58: Force – Displacement plot on Shuriken sphere compressed by 25% or 100µm; 1st cycle, the compression phase was represented in blue, while the recovery phase was indicated in orange on the plot.

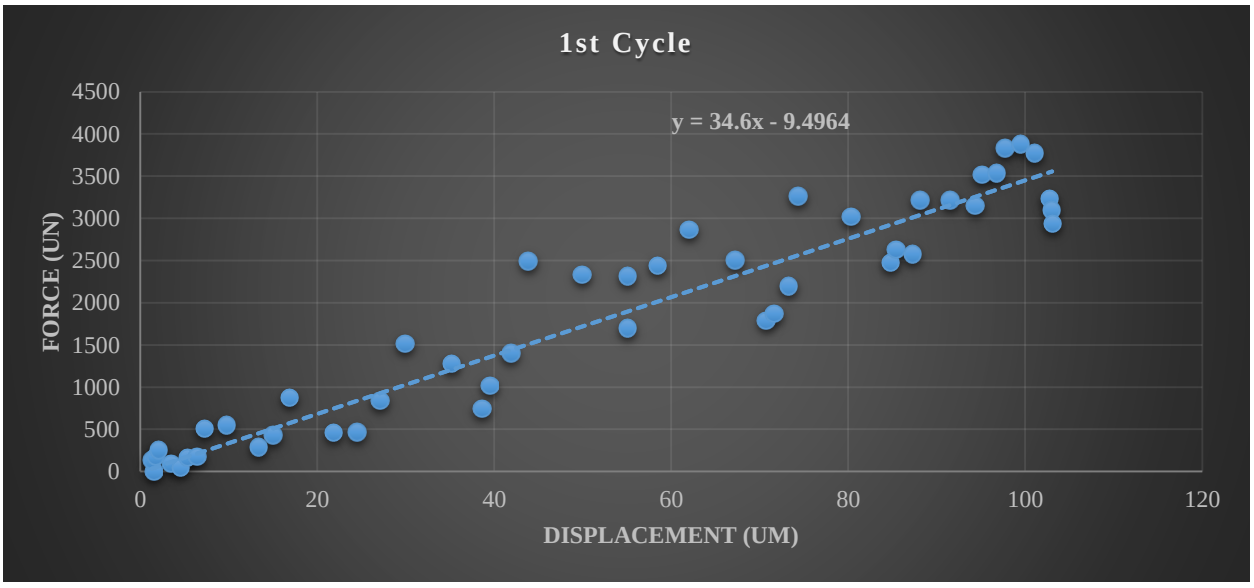

Figure 59: Force – Displacement plot on Shuriken sphere compressed by 25% or 100µm; 1st cycle, only the compression phase was depicted, and the slope of the line on the plot represented the stiffness.

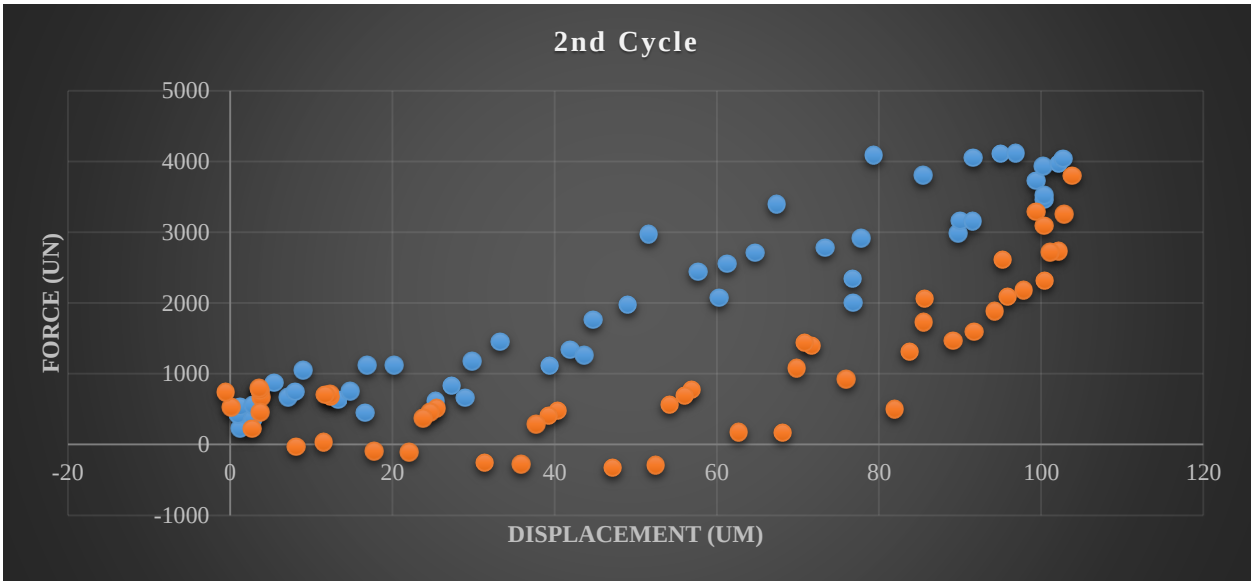

Figure 60: Force – Displacement plot on Shuriken sphere compressed by 25% or 100μm; 2nd cycle, the compression phase was represented in blue, while the recovery phase was indicated in orange on the plot.

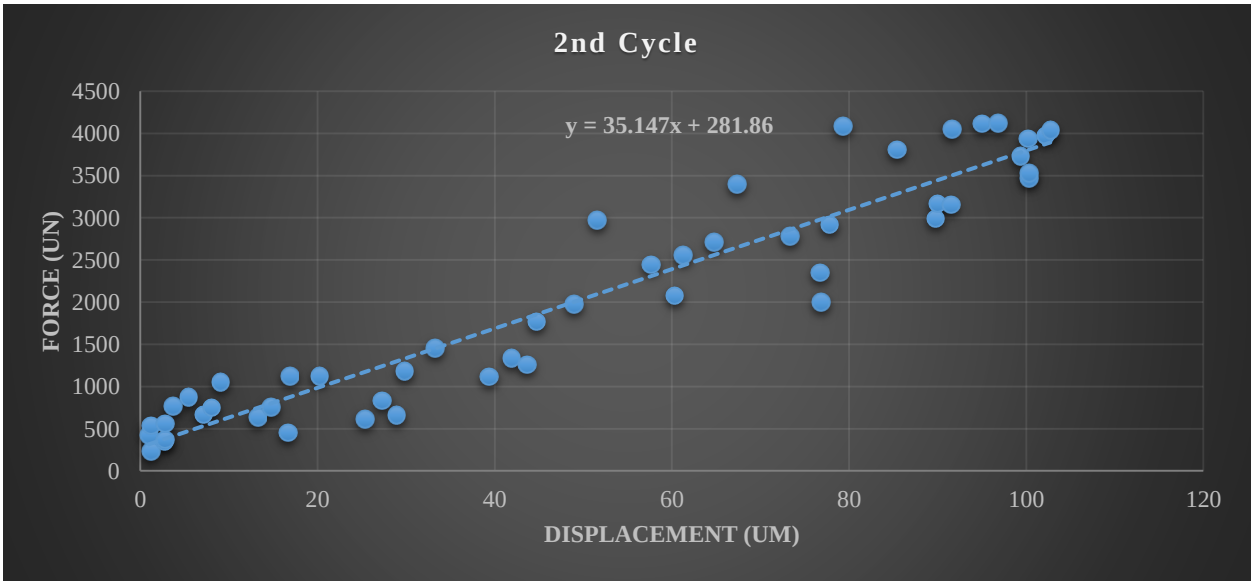

Figure 61: Force – Displacement plot on Shuriken sphere compressed by 25% or 100μm; 2nd cycle, only the compression phase was depicted, and the slope of the line on the plot represented the stiffness.

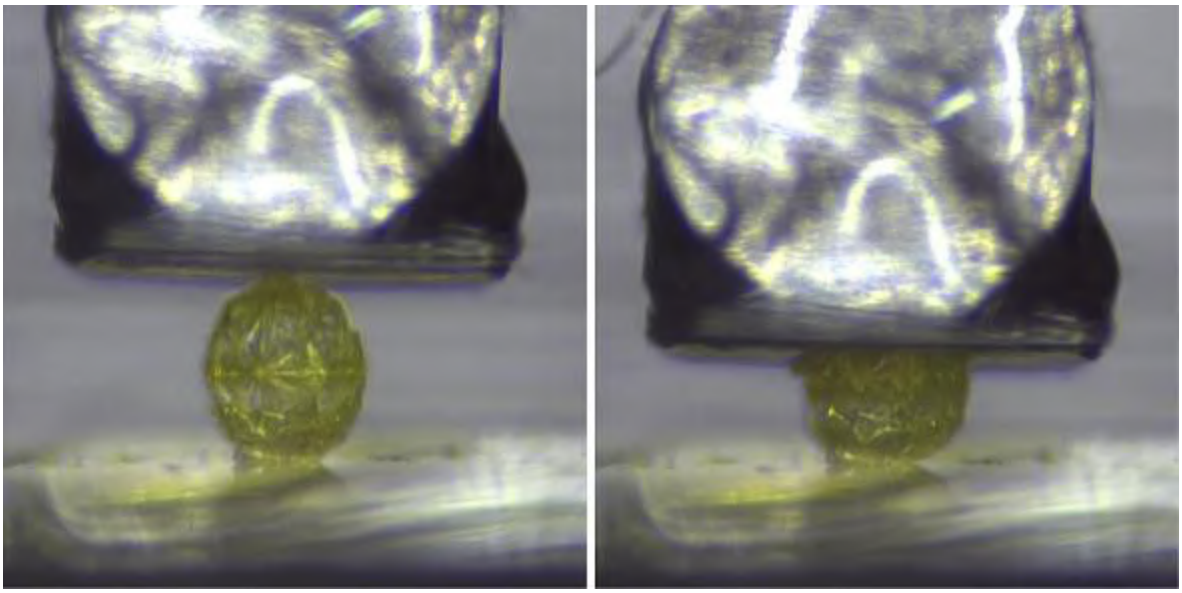

Figure 62: Shuriken sphere compressed by 50% or 200µm.

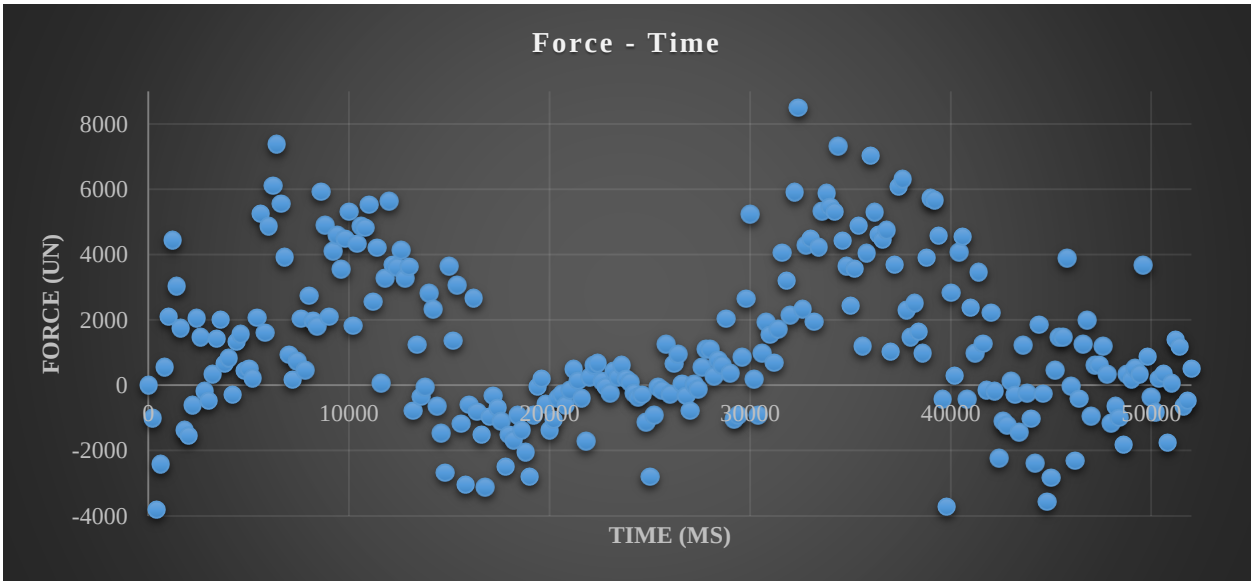

Figure 63: Force – Time plot on Shuriken sphere compressed by 50% or 200µm

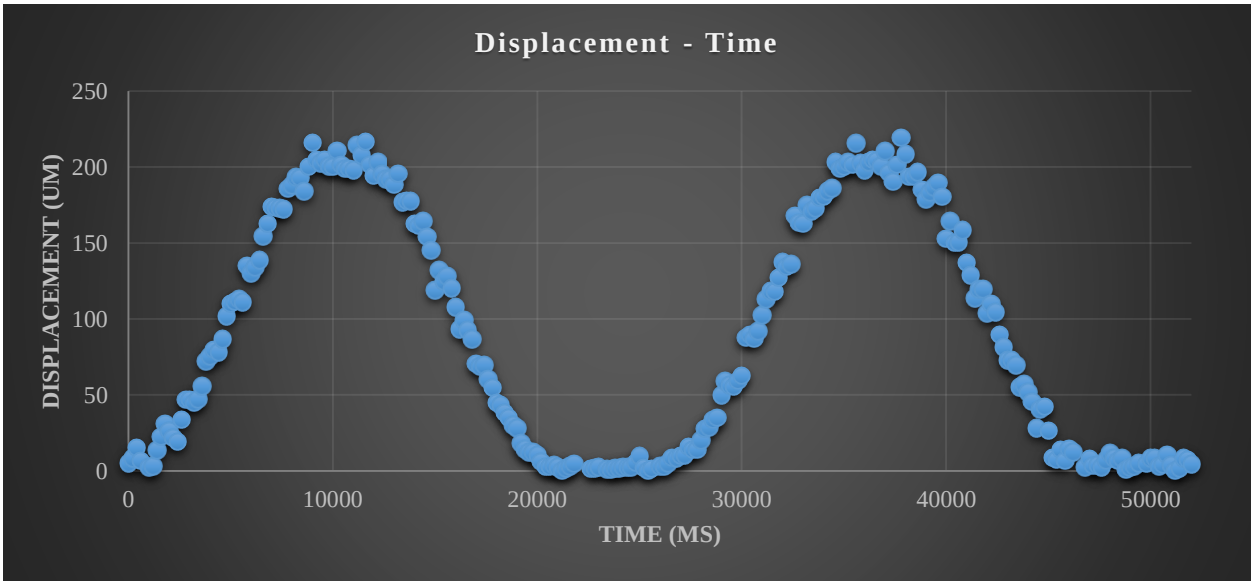

Figure 64: Displacement – Time plot on Shuriken sphere compressed by 50% or 200µm.

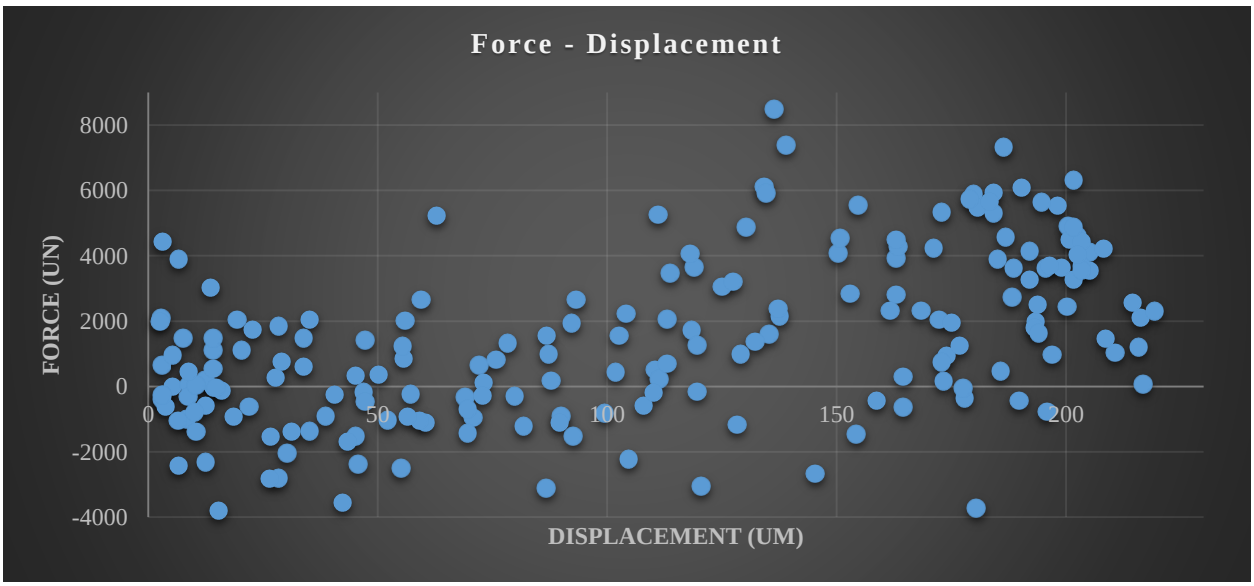

Figure 65: Force – Displacement plot on Shuriken sphere compressed by 50% or 200µm.

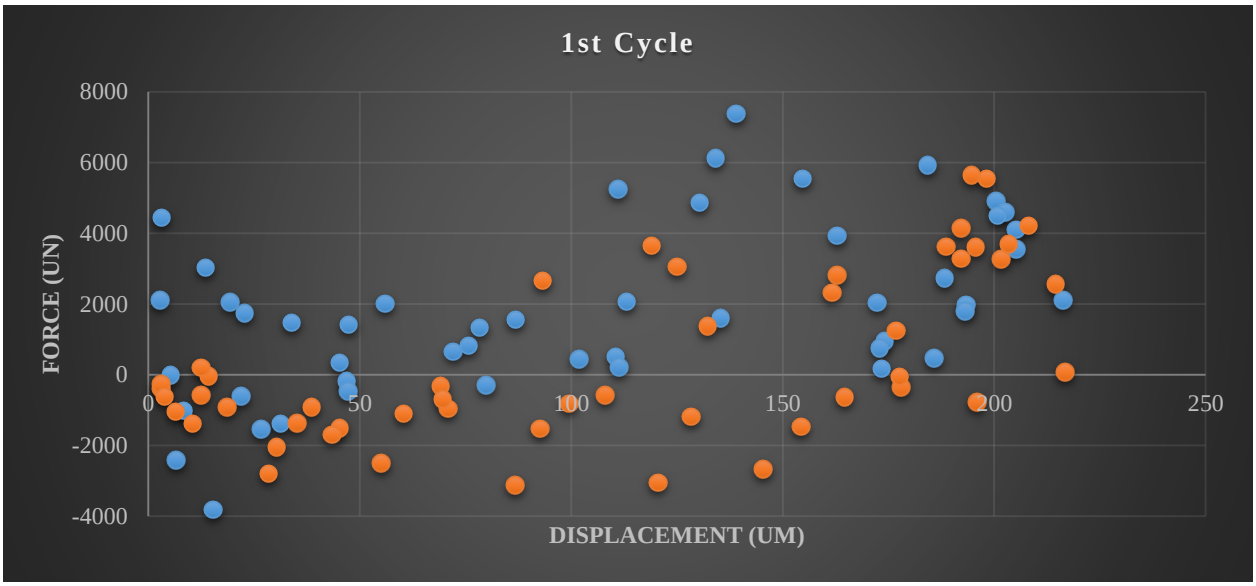

Figure 66: Force – Displacement plot on Shuriken sphere compressed by 50% or 200µm; 1st cycle, the compression phase was represented in blue, while the recovery phase was indicated in orange on the plot.

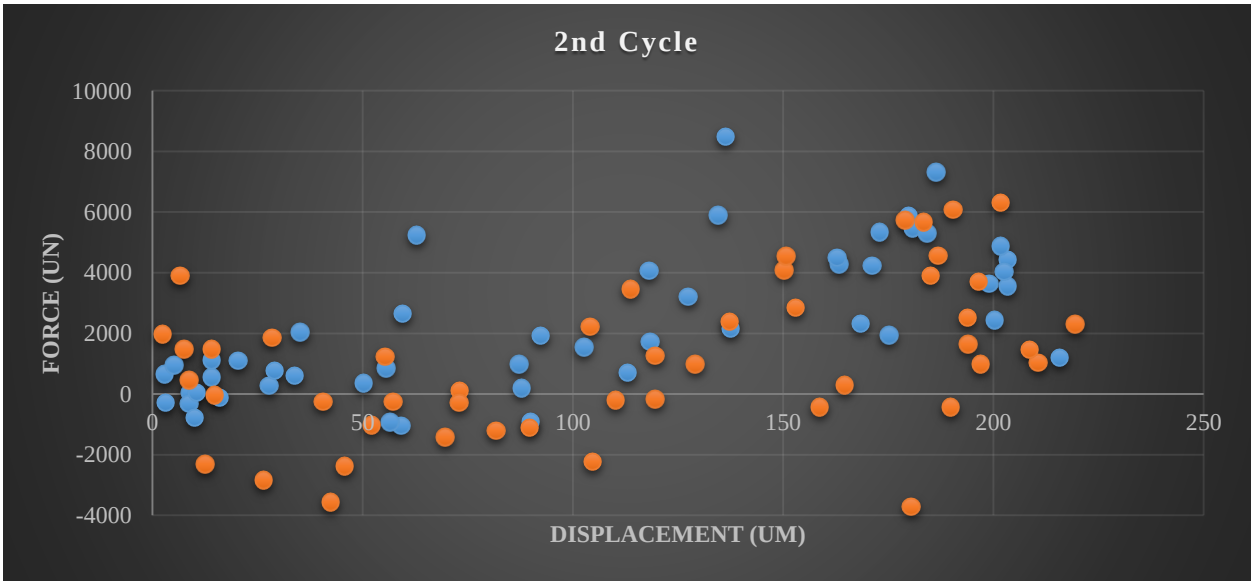

Figure 67: Force – Displacement plot on Shuriken sphere compressed by 50% or 200µm; 2nd cycle, the compression phase was represented in blue, while the recovery phase was indicated in orange on the plot.

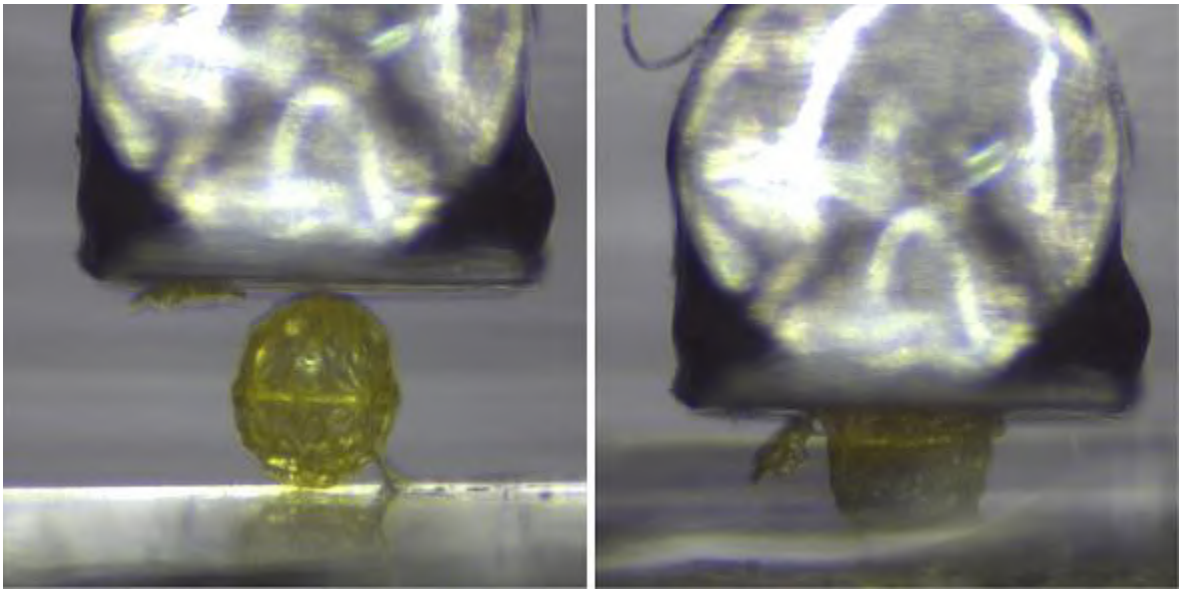

Figure 68: Shuriken sphere compressed by 75% or 300µm.

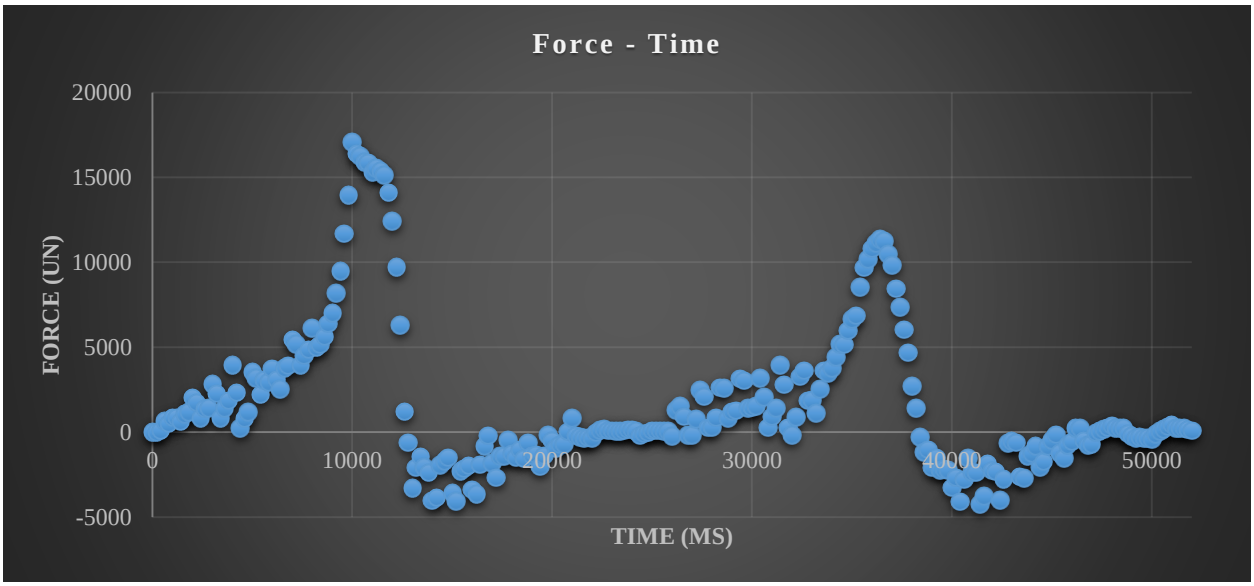

Figure 69: Force – Time plot on Shuriken sphere compressed by 75% or 300µm.

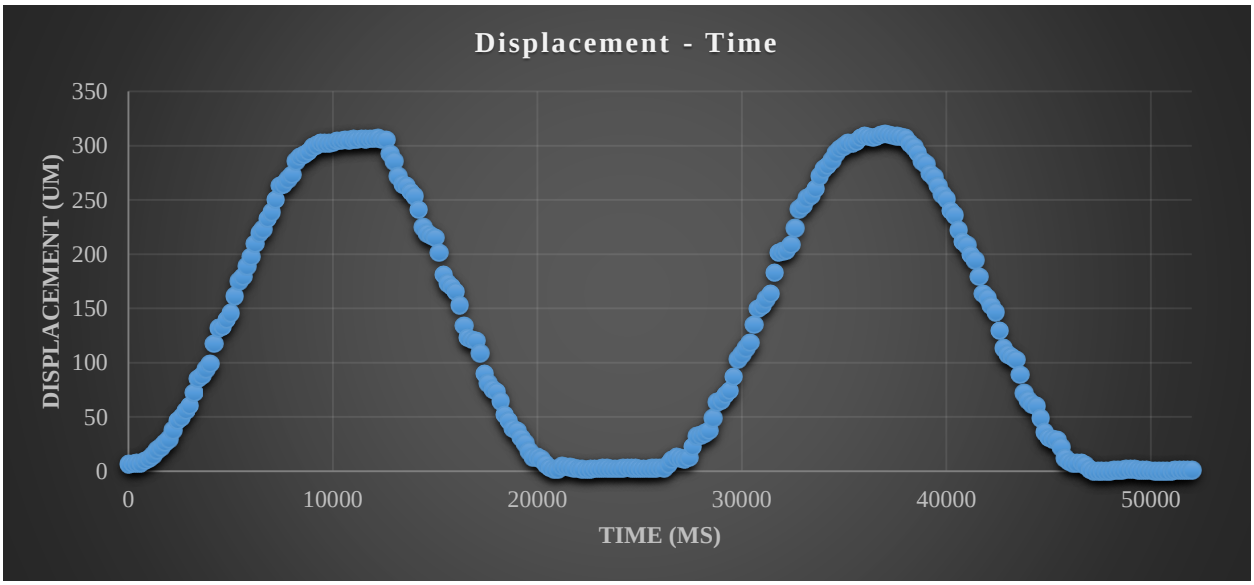

Figure 70: Displacement – Time plot on Shuriken sphere compressed by 75% or 300µm.

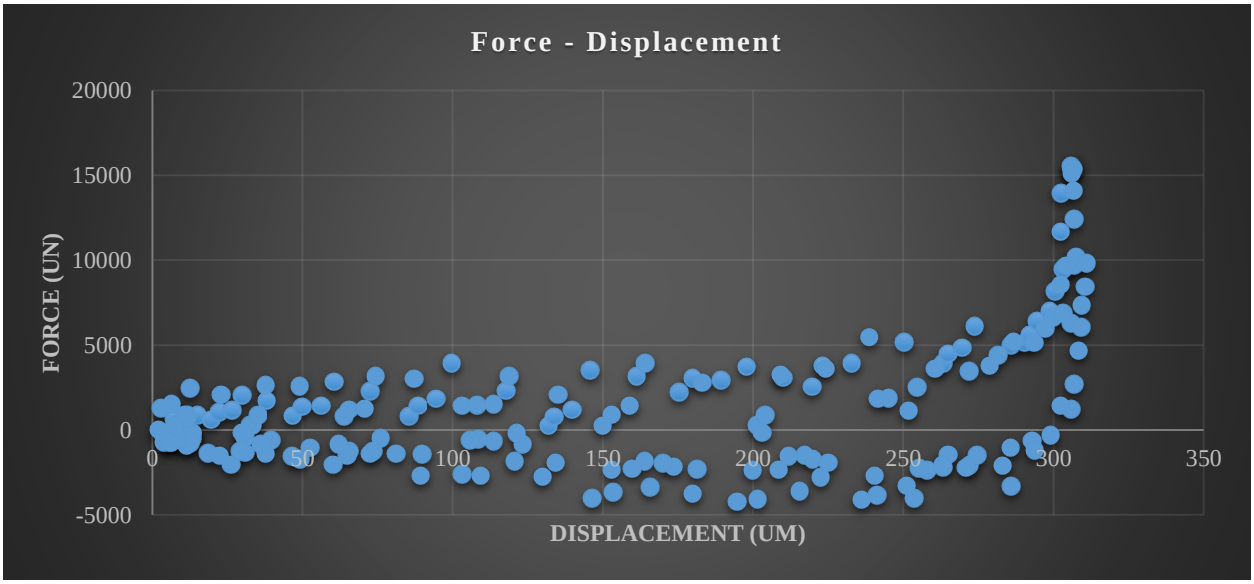

Figure 71: Force – Displacement plot on Shuriken sphere compressed by 75% or 300µm.

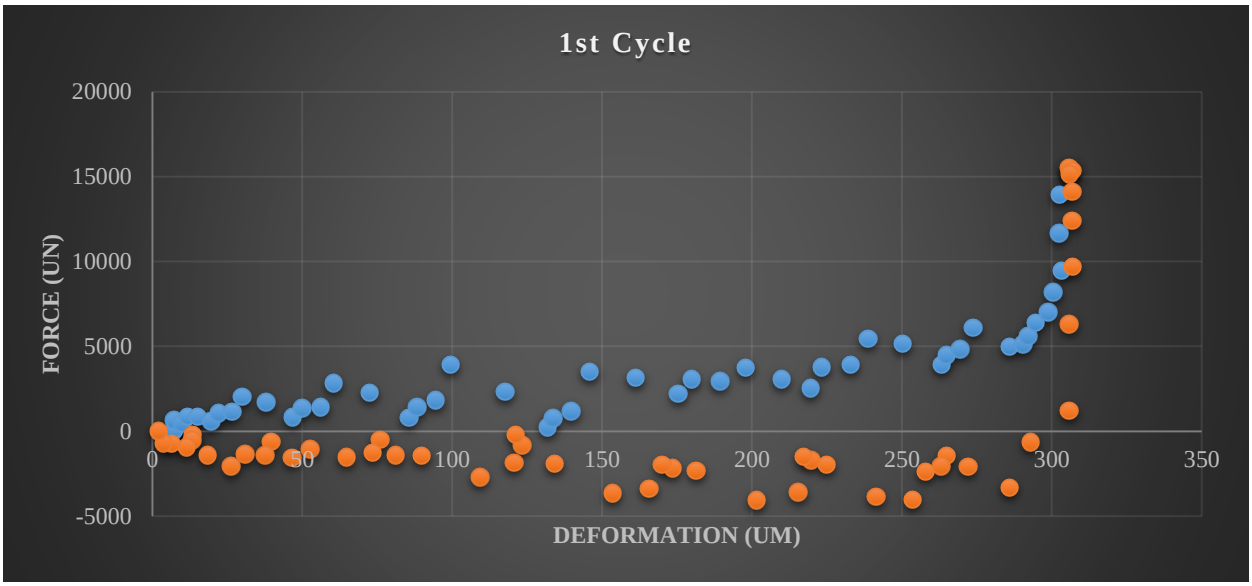

Figure 72: Force – Displacement plot on Shuriken sphere compressed by 75% or 300µm; 1st cycle, the compression phase was represented in blue, while the recovery phase was indicated in orange on the plot.

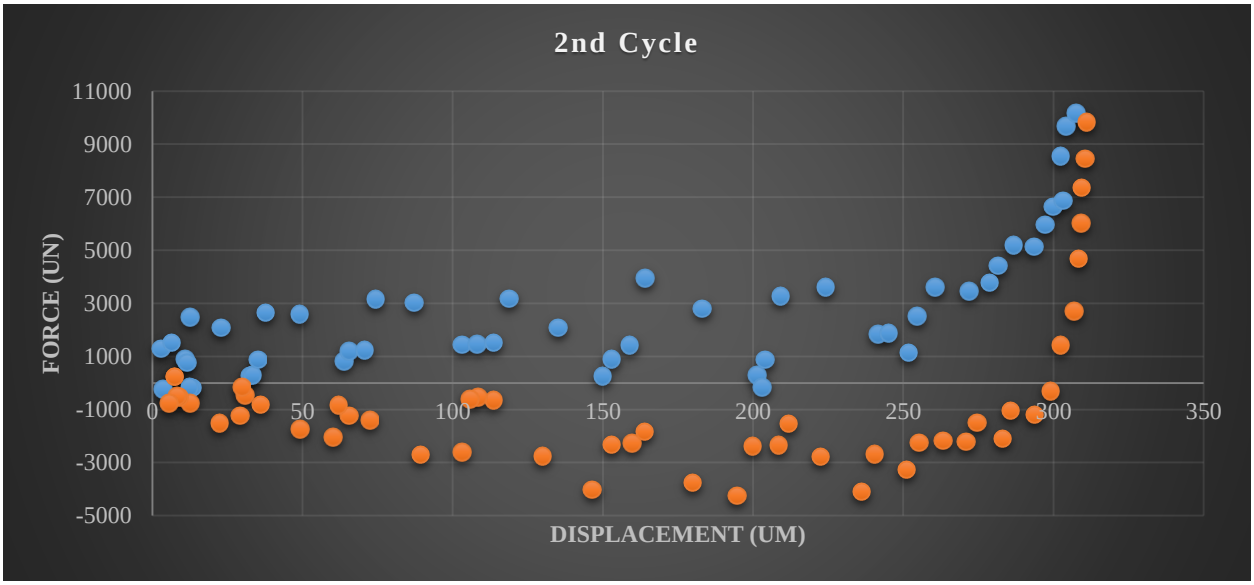

Figure 73: Force – Displacement plot on Shuriken sphere compressed by 75% or 300µm; 2nd cycle, the compression phase was represented in blue, while the recovery phase was indicated in orange on the plot.

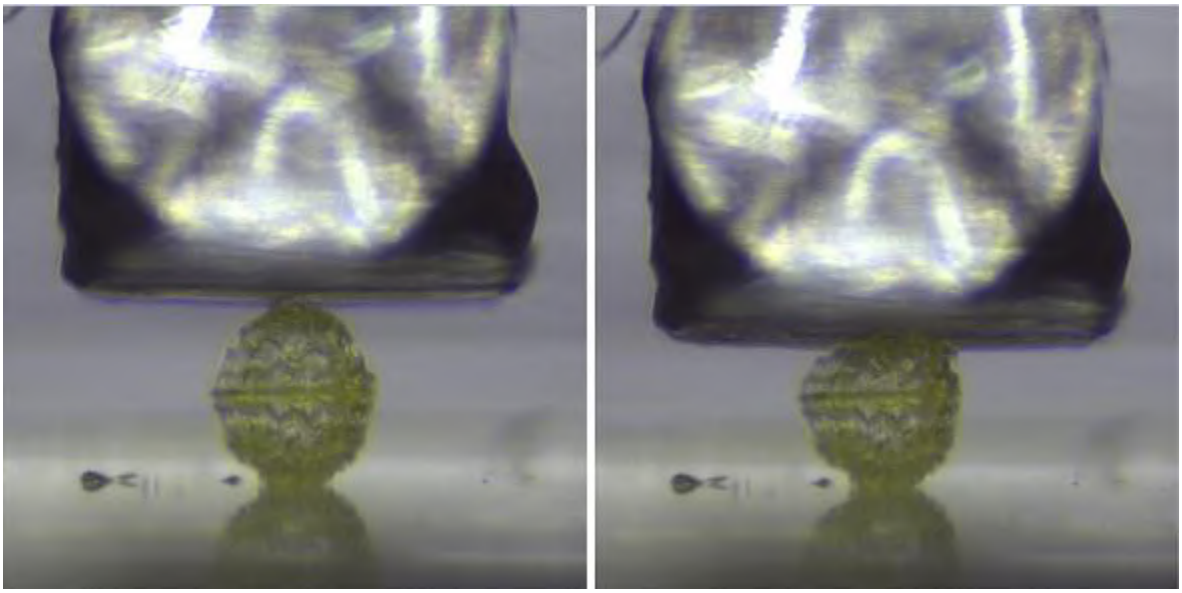

Figure 74: Bowtie sphere compressed by 25% or 100µm.

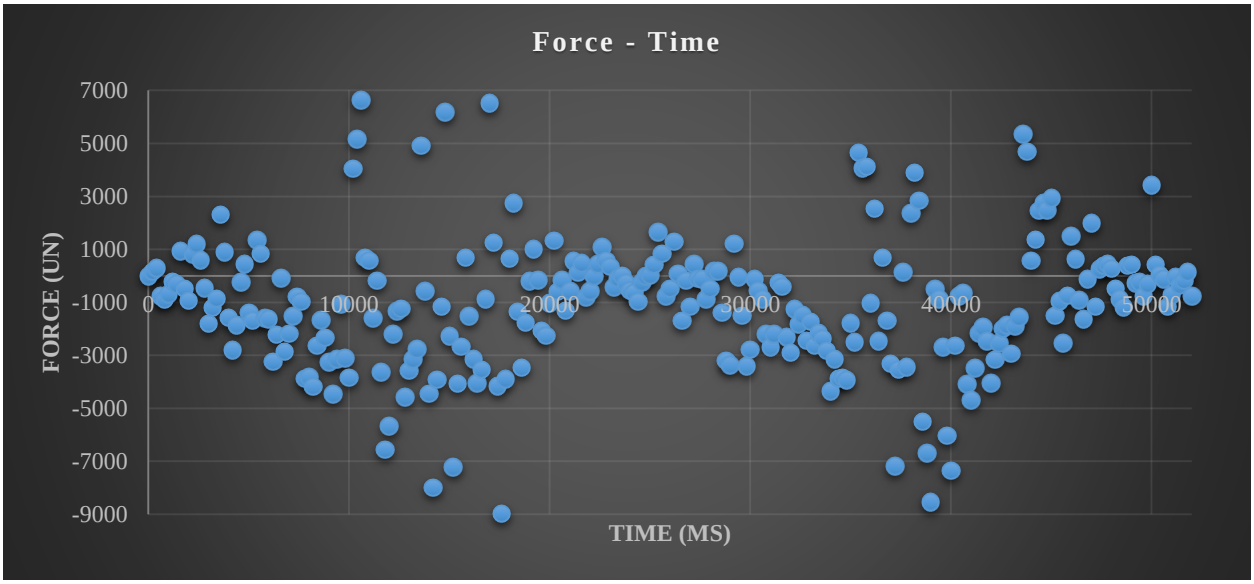

Figure 75: Force – Time plot on Bowtie sphere compressed by 25% or 100µm.

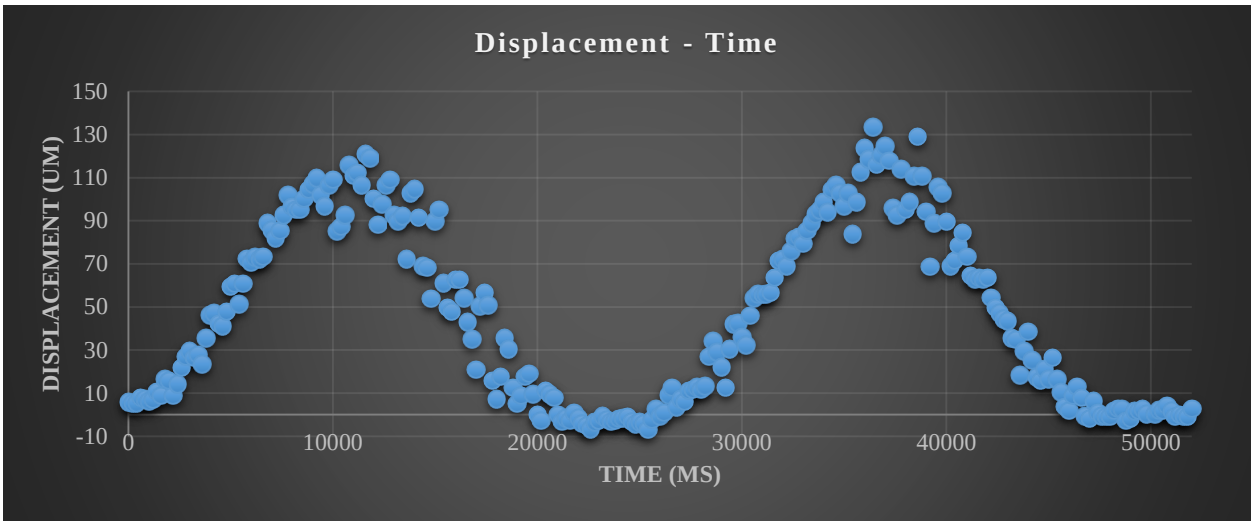

Figure 76: Displacement – Time plot on Bowtie sphere compressed by 25% or 100µm.

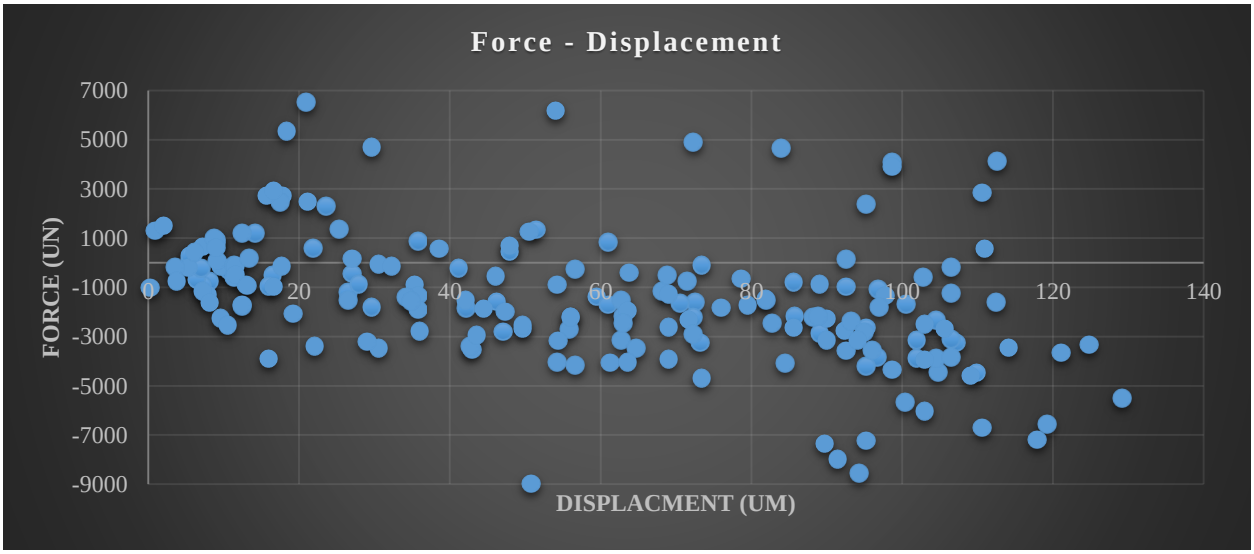

Figure 77: Force – Displacement plot on Bowtie sphere compressed by 25% or 100µm.

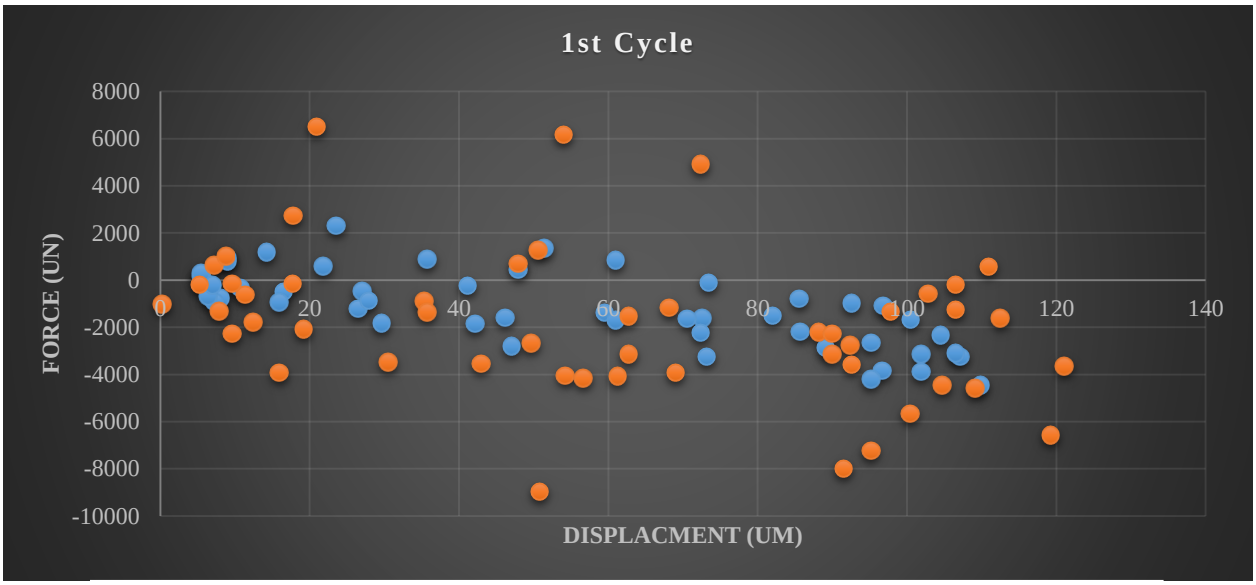

Figure 78: Force – Displacement plot on Bowtie sphere compressed by 25% or 100µm; 1st cycle, the compression phase was represented in blue, while the recovery phase was indicated in orange on the plot.

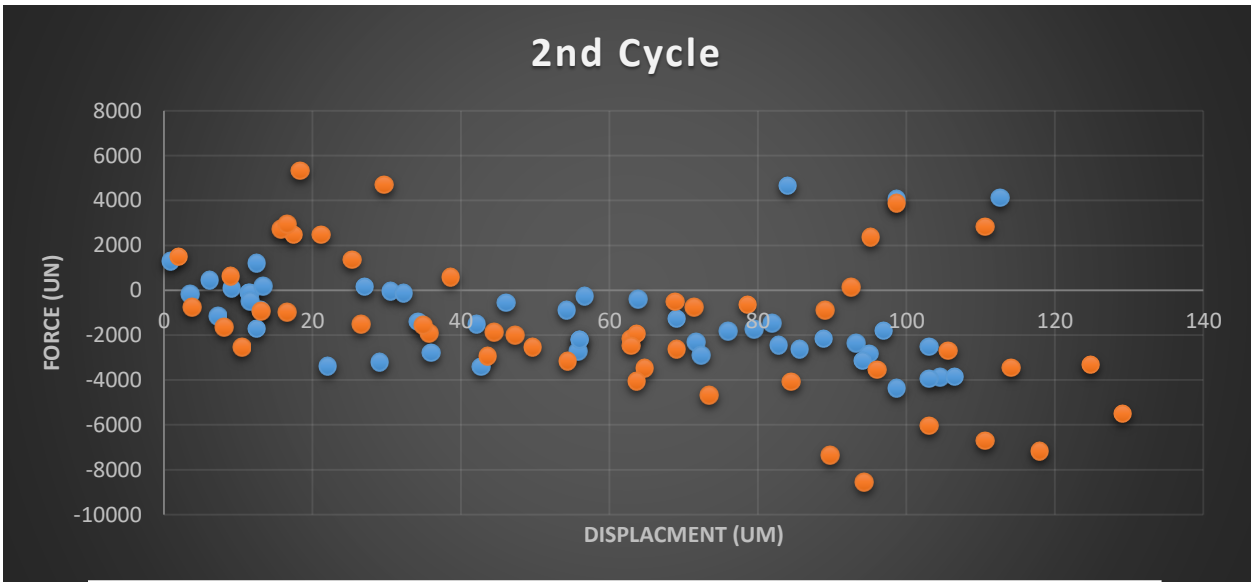

Figure 79: Force – Displacement plot on Bowtie sphere compressed by 25% or 100µm; 1st cycle, the compression phase was represented in blue, while the recovery phase was indicated in orange on the plot.

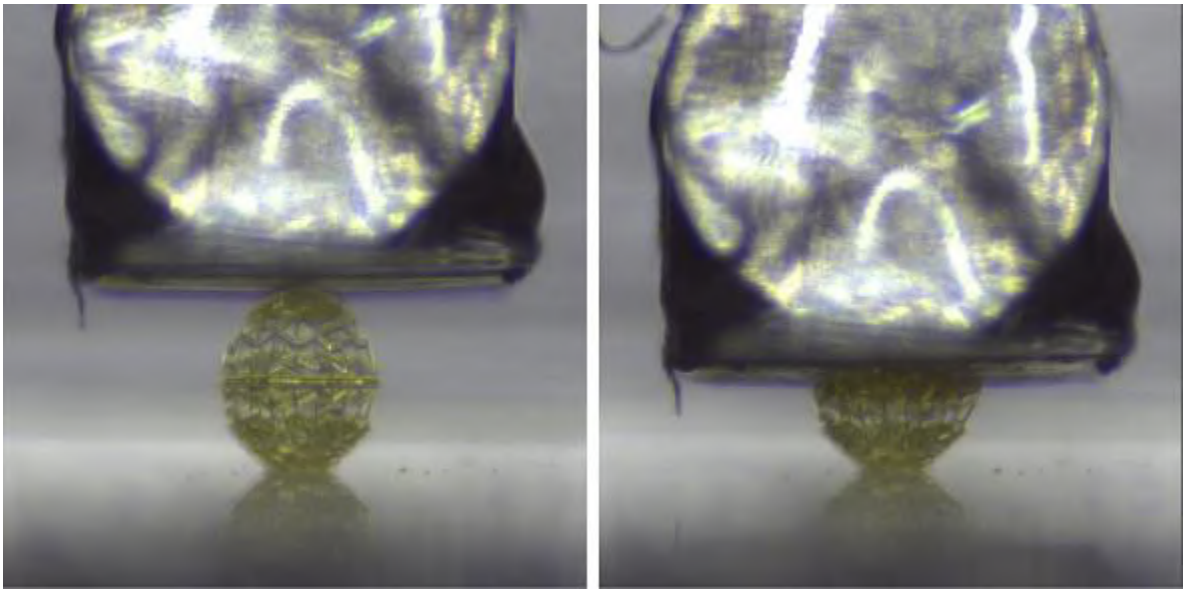

Figure 80: Bowtie sphere compressed by 50% or 200µm.

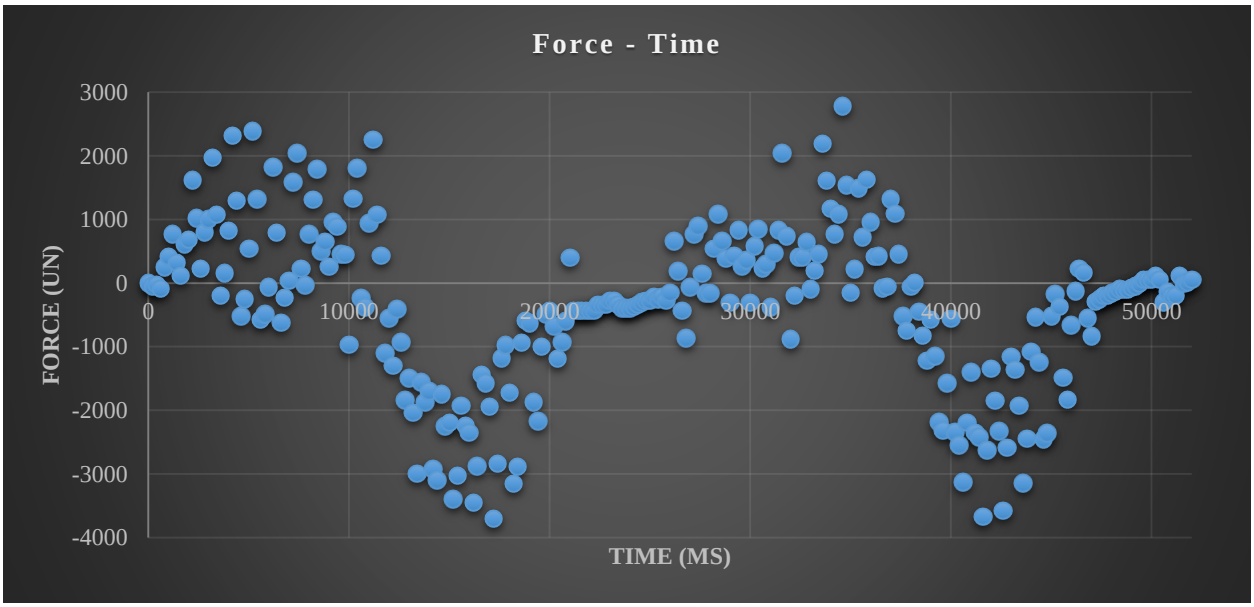

Figure 81: Force – Time plot on Bowtie sphere compressed by 50% or 200µm.

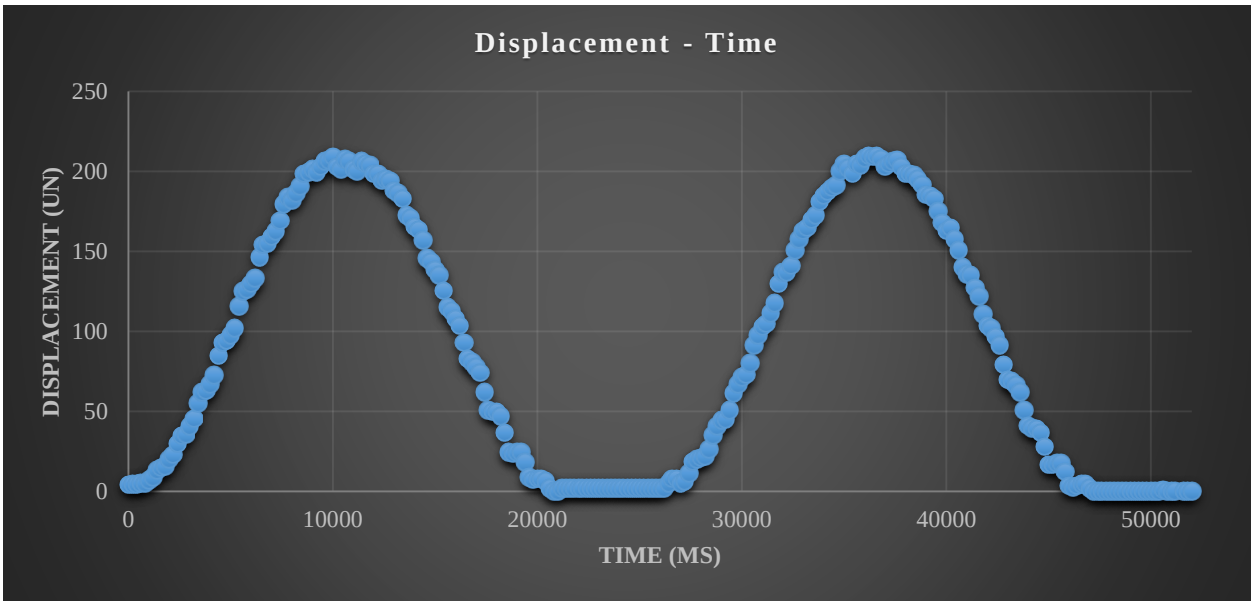

Figure 82: Displacement – Time plot on Bowtie sphere compressed by 50% or 200µm.

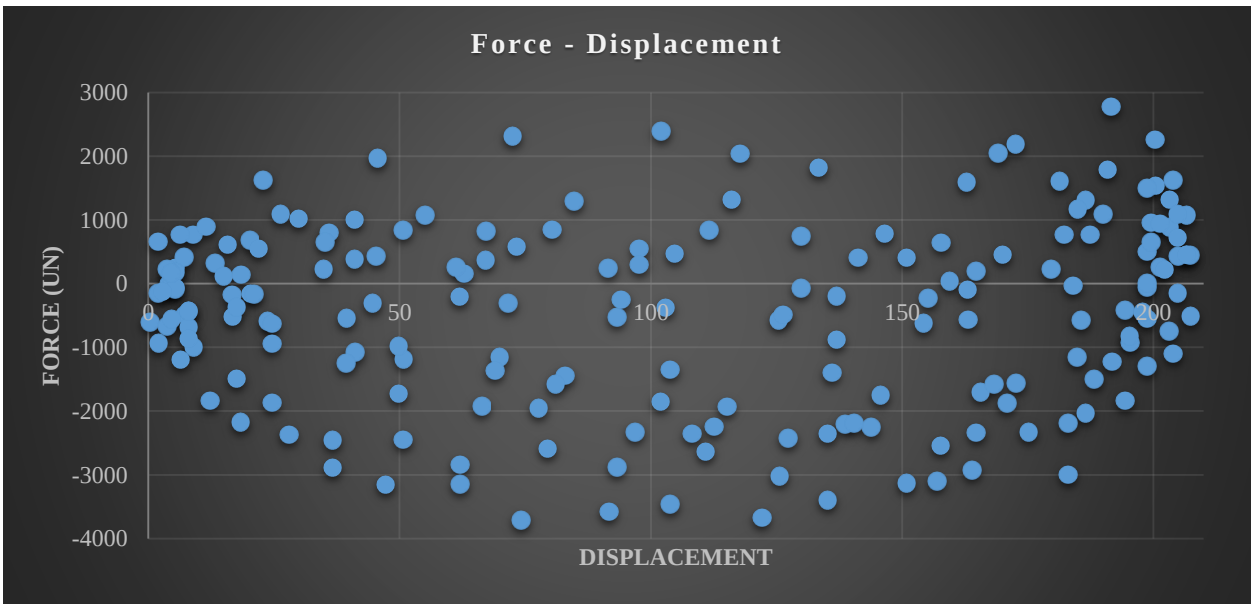

Figure 83: Force – Displacement chart on Bowtie sphere compressed by 50% or 200µm.

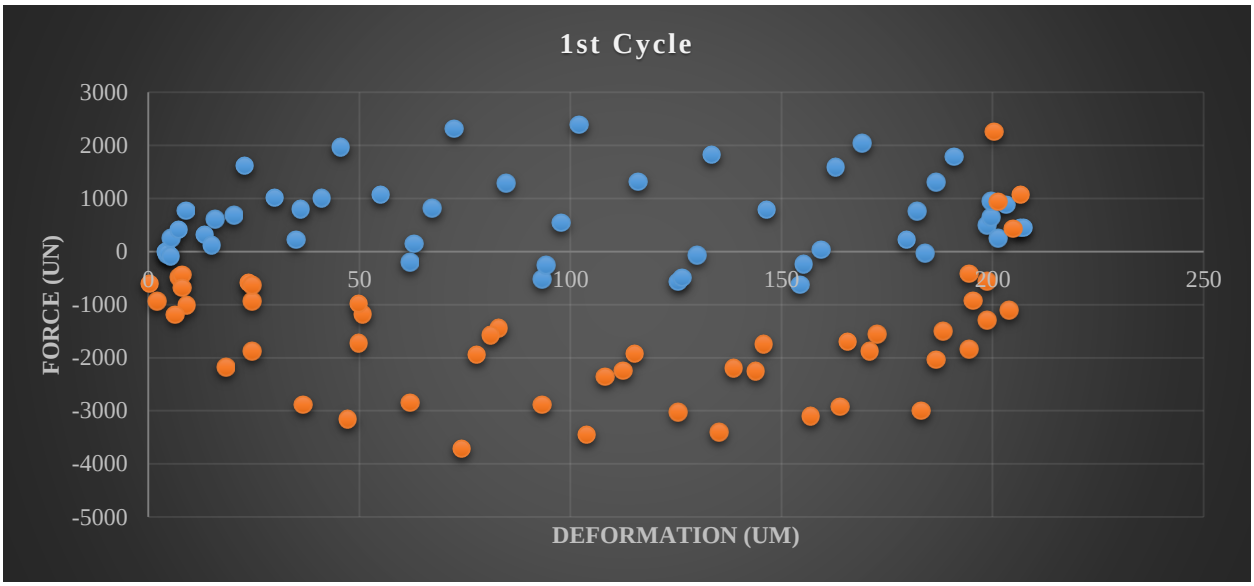

Figure 84: Force – Displacement plot on Bowtie sphere compressed by 50% or 200µm; 1st cycle, the compression phase was represented in blue, while the recovery phase was indicated in orange on the plot.

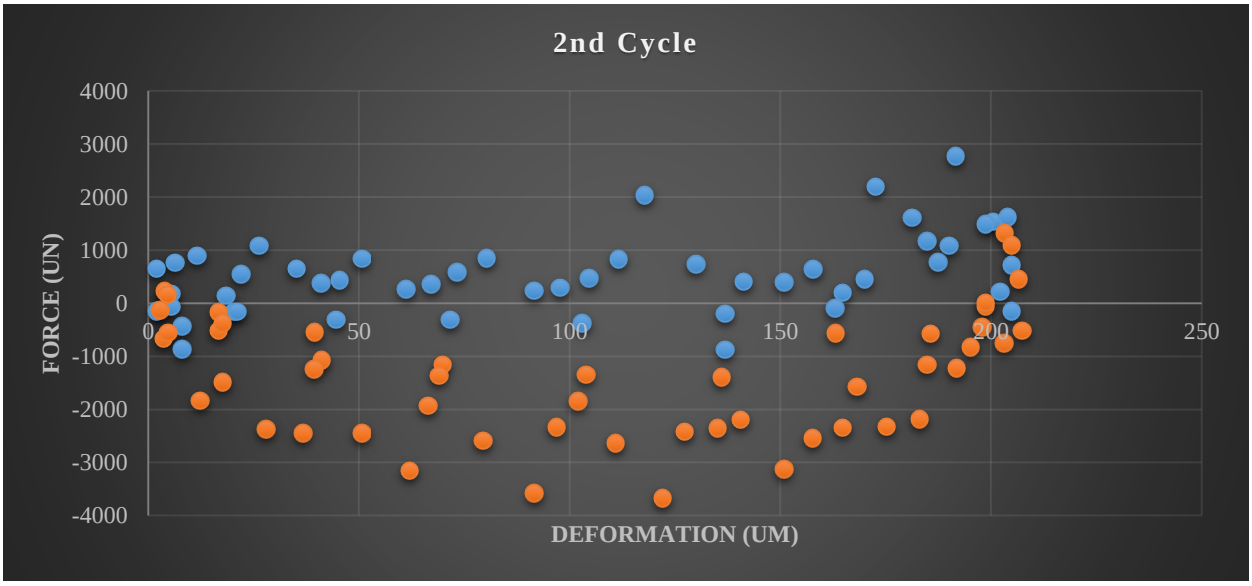

Figure 85: Force – Displacement plot on Bowtie sphere compressed by 50% or 200µm; 2nd cycle, the compression phase was represented in blue, while the recovery phase was indicated in orange on the plot.

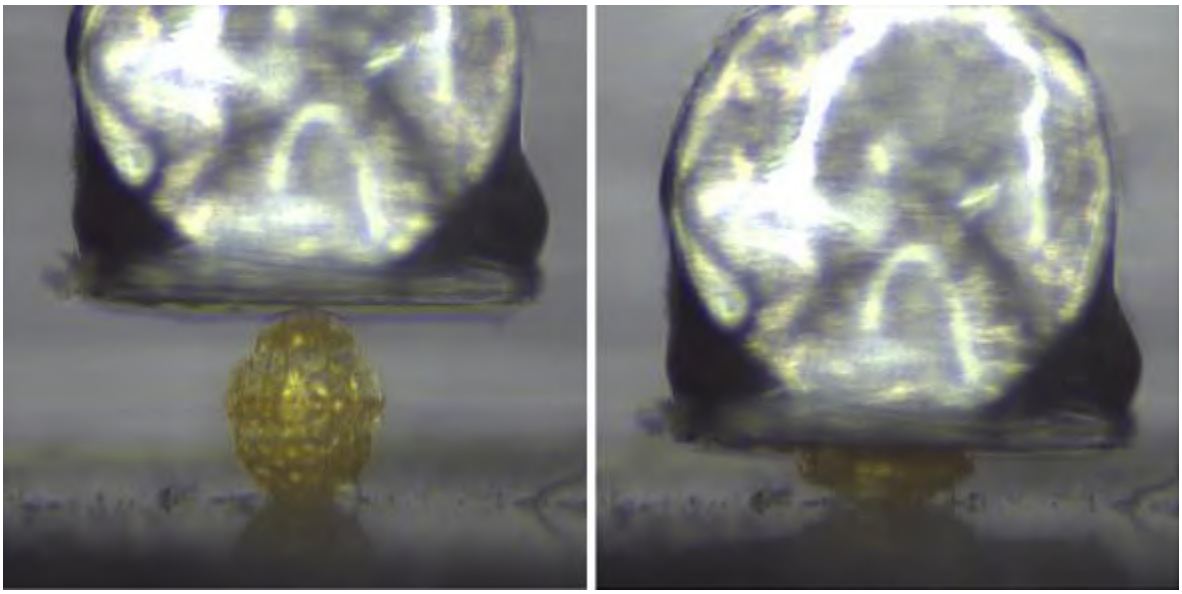

Figure 86: Bowtie sphere compressed by 75% or 300µm.

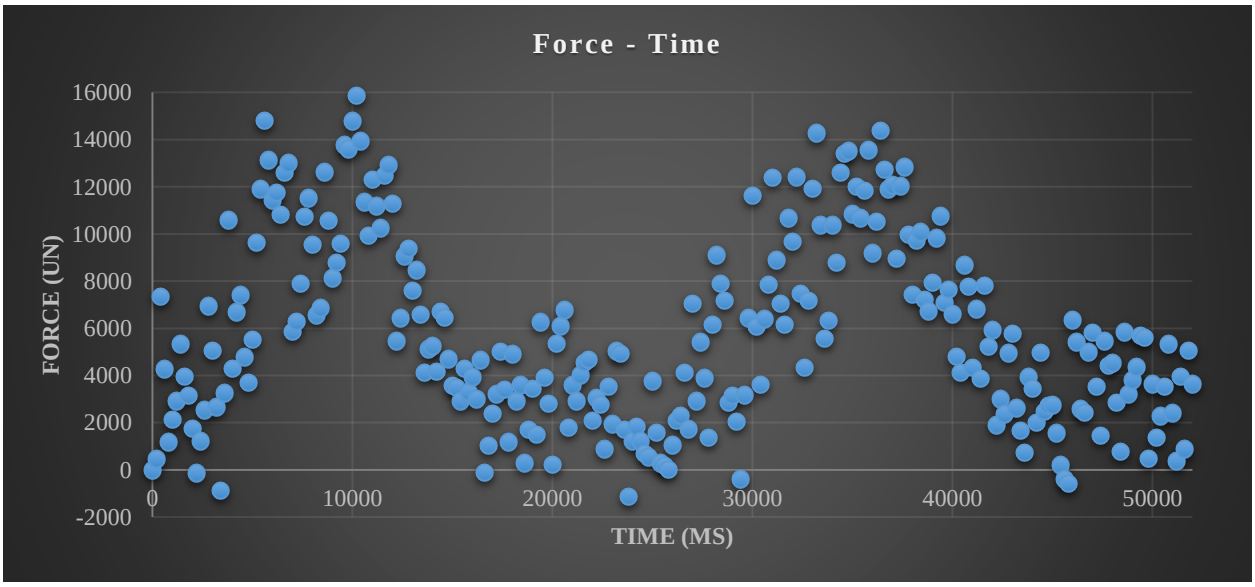

Figure 87: Force – Time plot on Bowtie sphere compressed by 75% or 300µm.

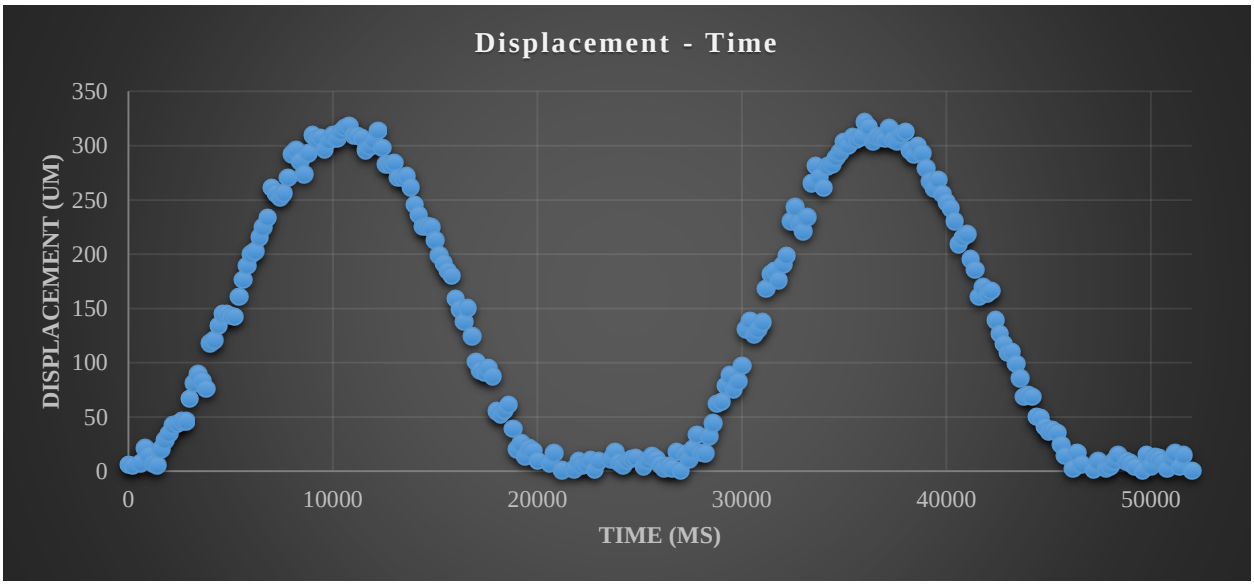

Figure 88: Displacement – Time plot on Bowtie sphere compressed by 75% or 300µm.

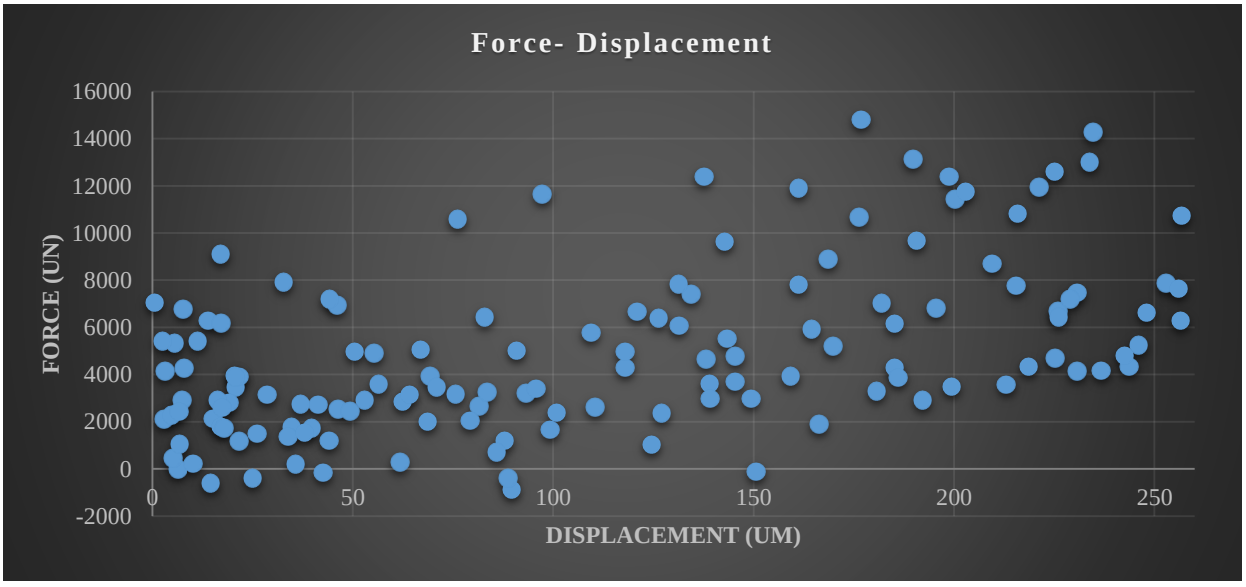

Figure 89: Force – Displacement plot on Bowtie sphere compressed by 75% or 300µm.

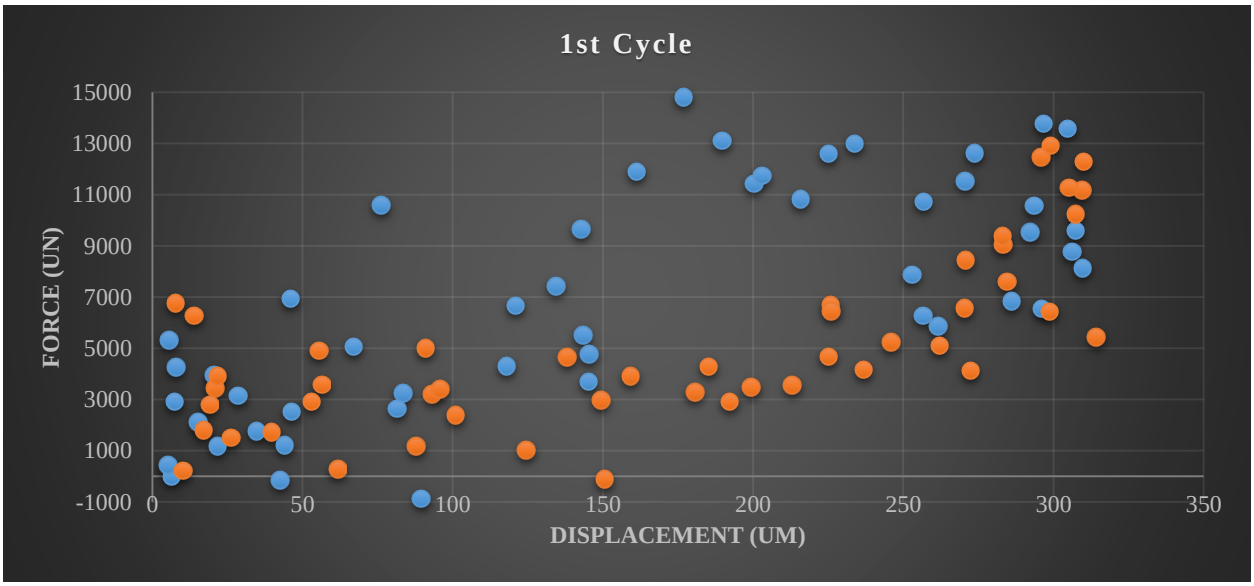

Figure 90: Force – Displacement plot on Bowtie sphere compressed by 75% or 300µm; 1st cycle, the compression phase was represented in blue, while the recovery phase was indicated in orange on the plot.

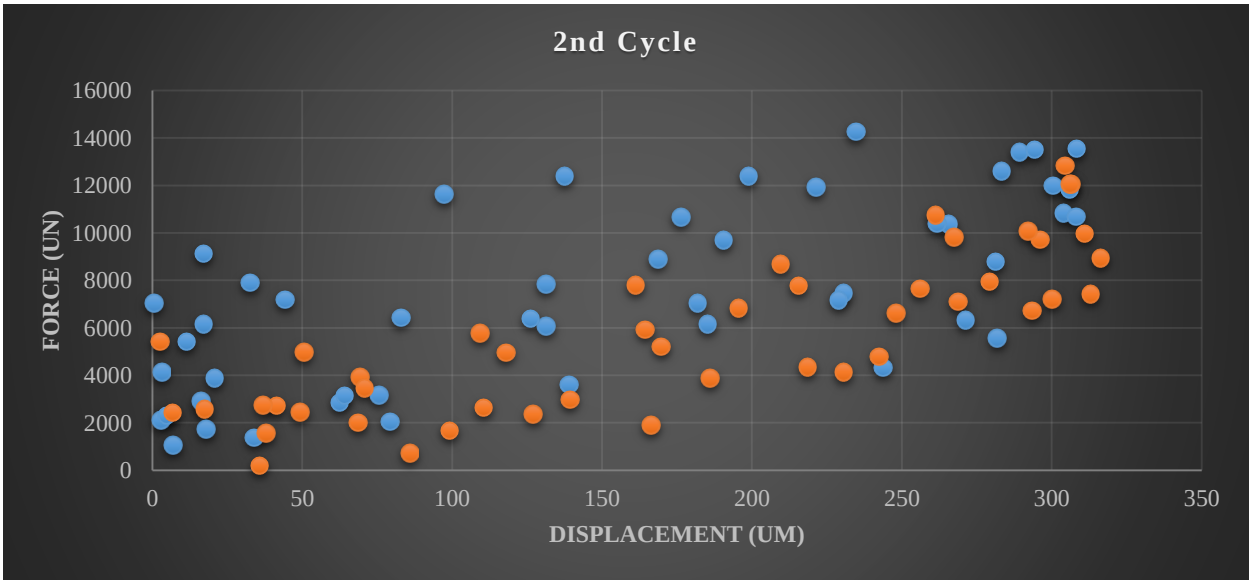

Figure 91: Force – Displacement plot on Bowtie sphere compressed by 75% or 300µm; 2nd cycle, the compression phase was represented in blue, while the recovery phase was indicated in orange on the plot.

Appendix E

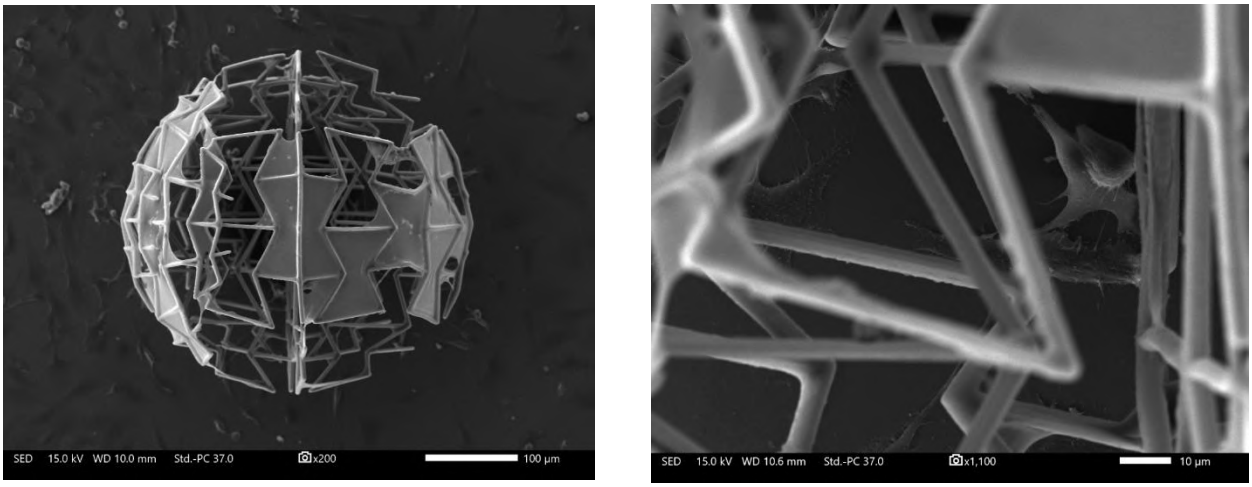

Figure 92: Top view of Bowtie at 3 days of culture.

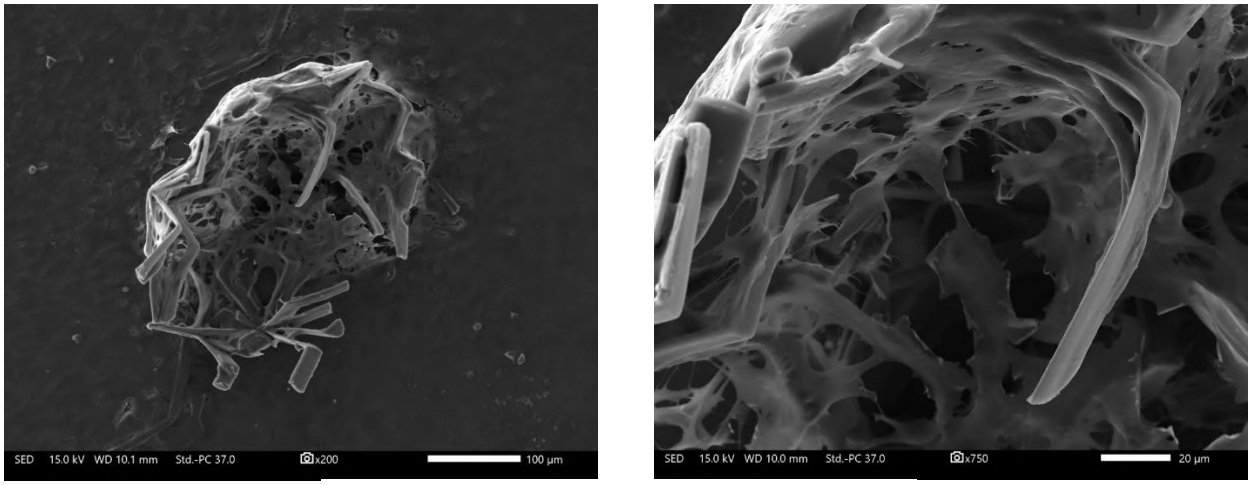

Figure 93: Top view of Shuriken at 3 days of culture.

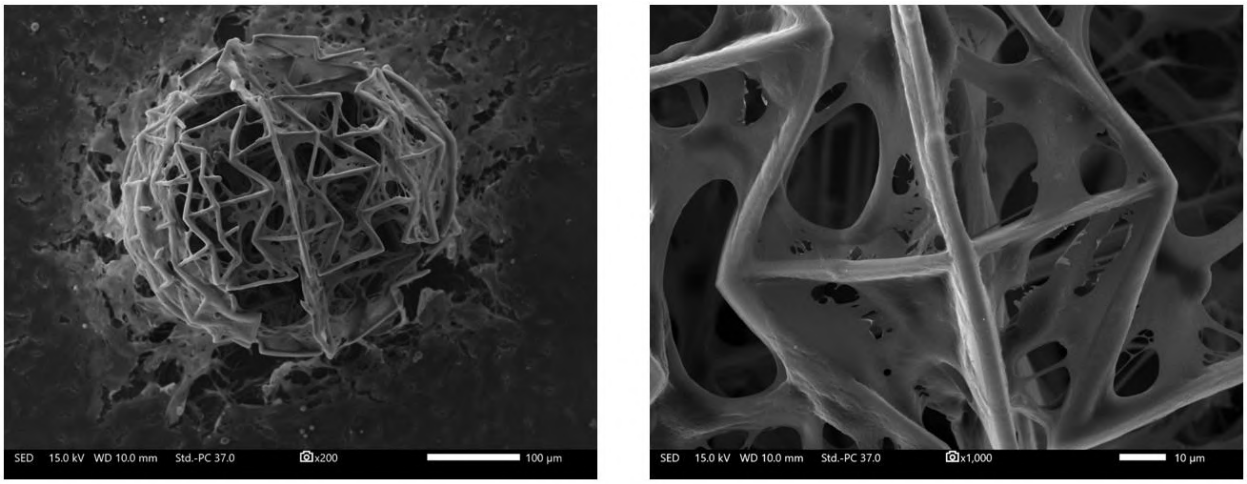

Figure 94: Top view of Bowtie at 5 days of culture.

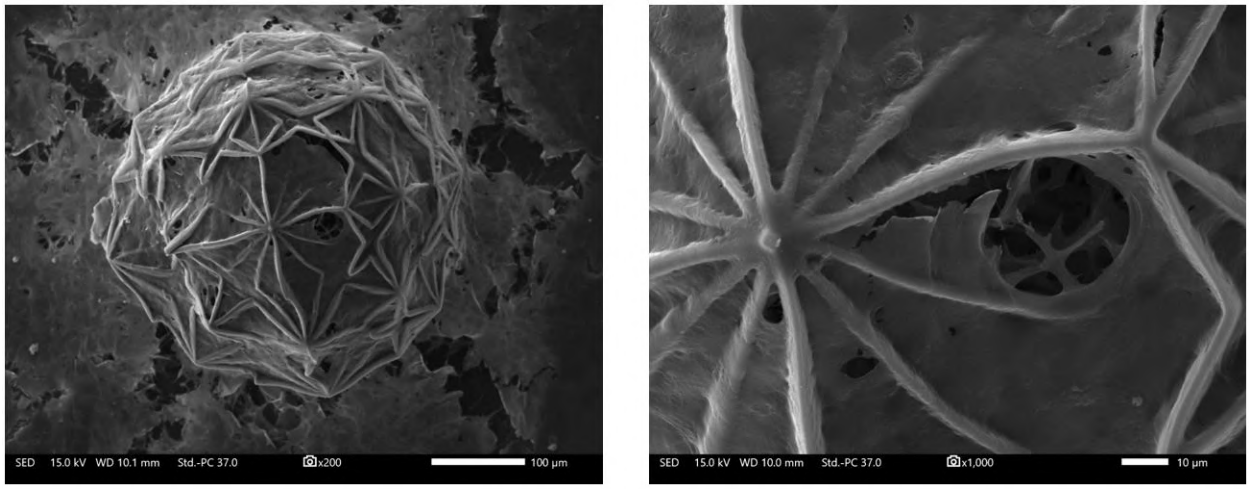

Figure 95: Top view of Shuriken at 5 days of culture.

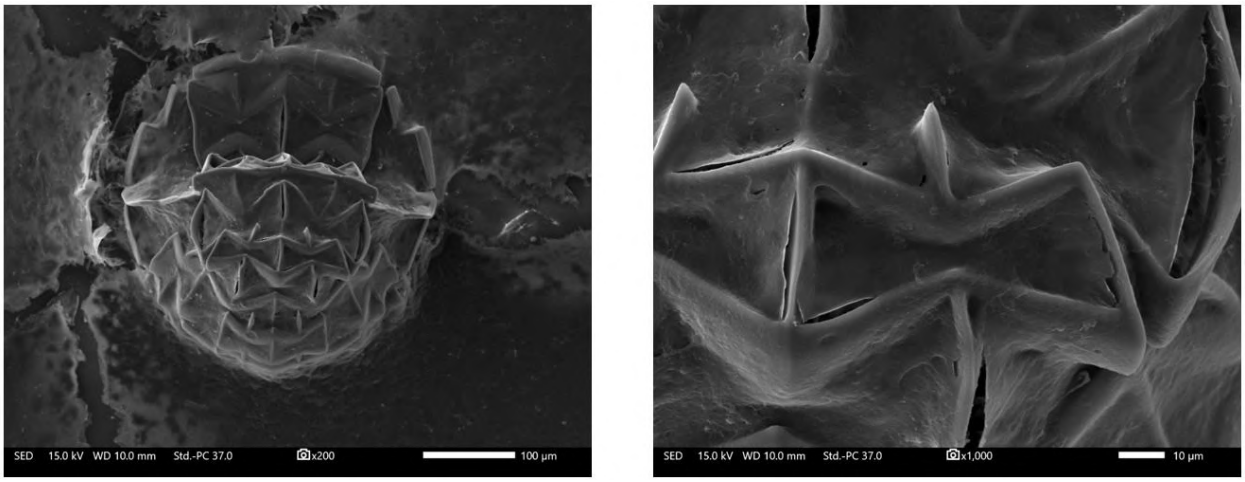

Figure 96: Top view of Bowtie at 7 days of culture.

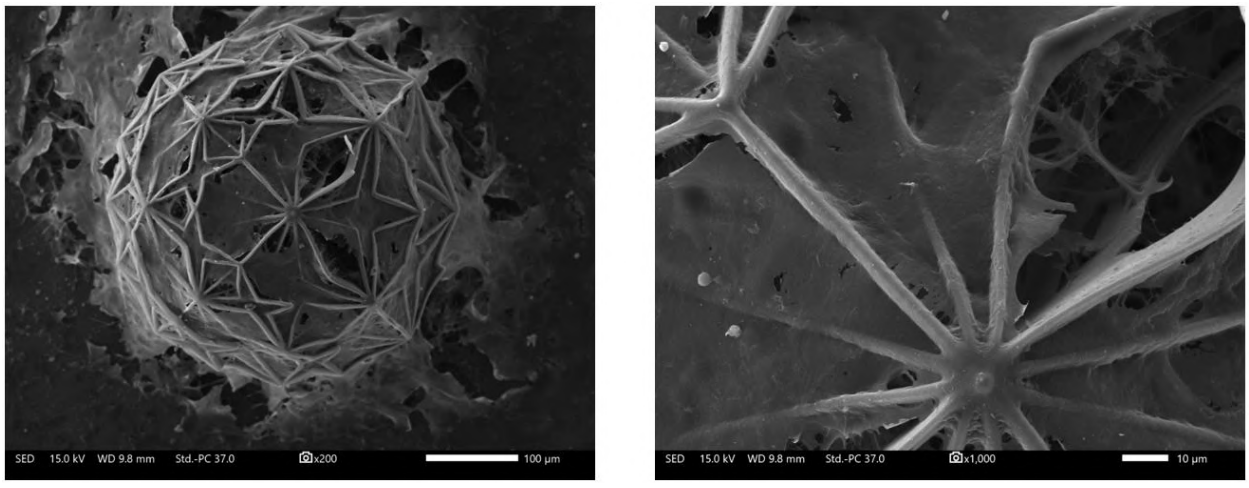

Figure 97: Top view of Shuriken at 7 days of culture.

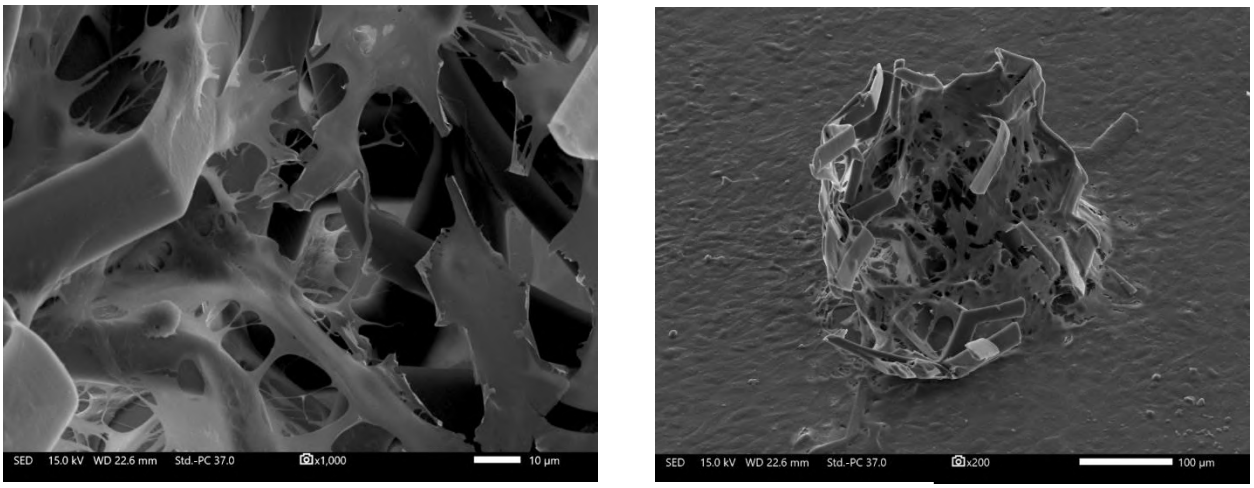

Figure 98: Tilted view of Shuriken at 3 days of culture.

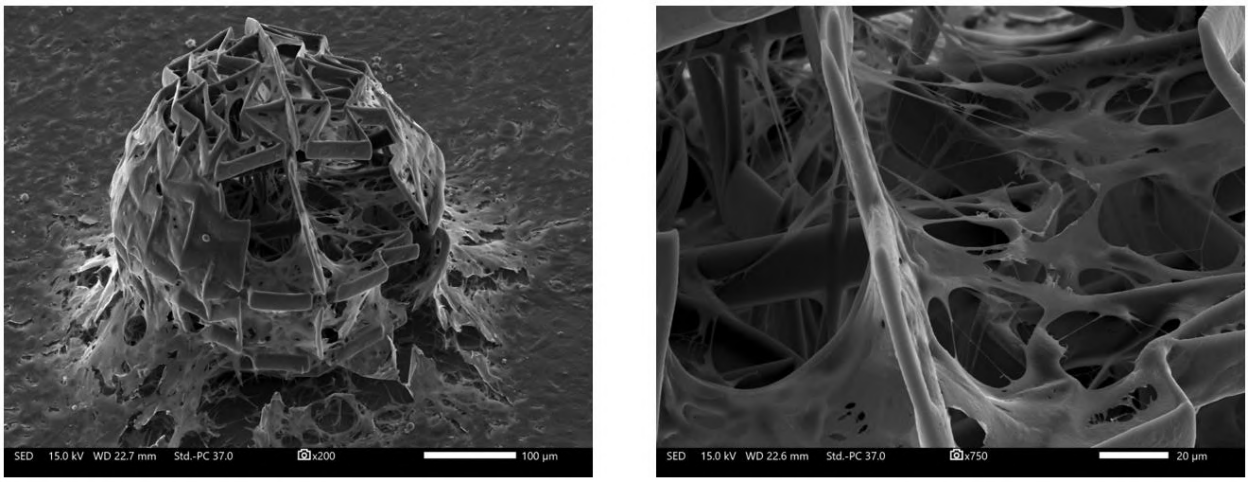

Figure 99: Tilted view of Bowtie at 5 days of culture.

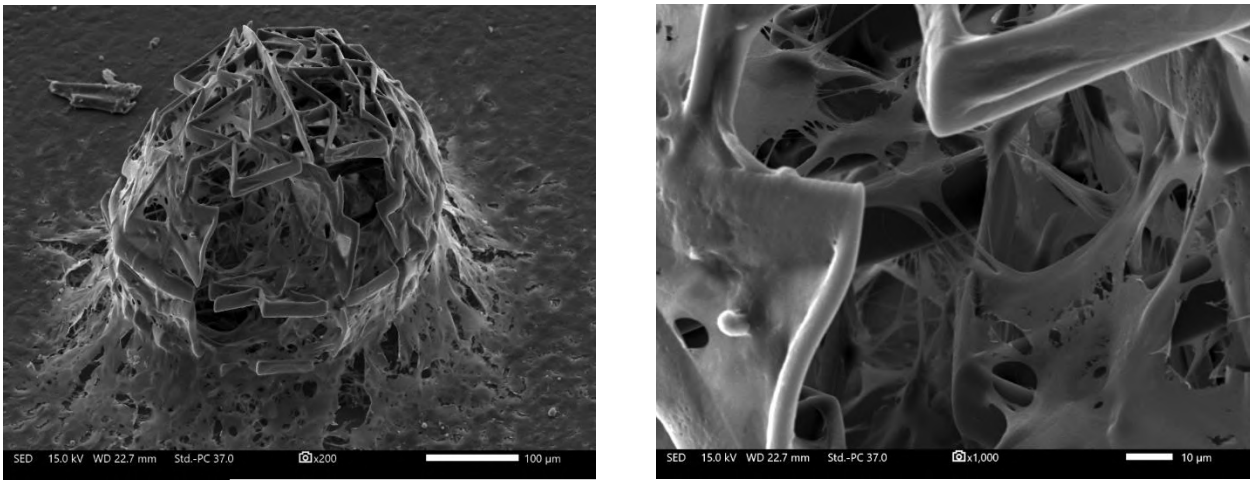

Figure 100: Tilted view of Bowtie at 5 days of culture from the other side.

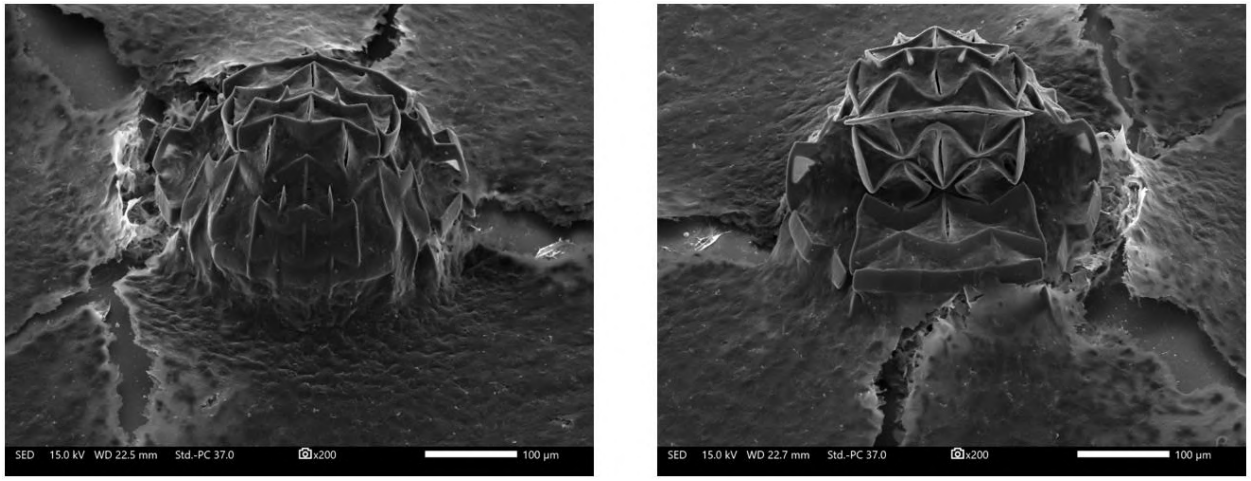

Figure 101: Tilted view of Bowtie at 7 days of culture.

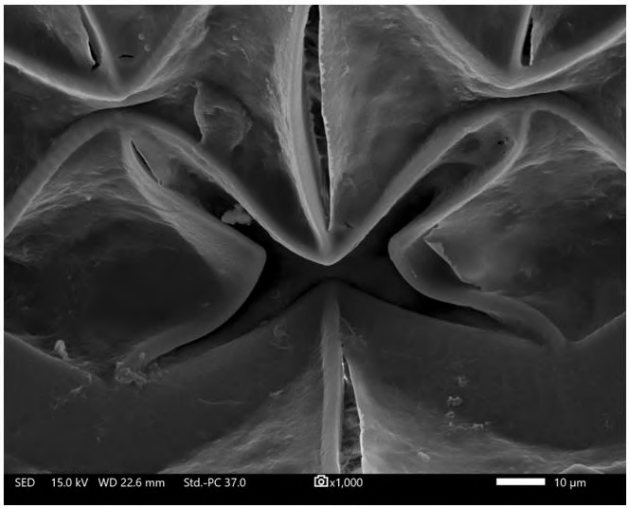

Figure 102: Closer view of the tilted Bowtie sphere. Here is a highlight of the mechanical properties of the scaffold; it is folded and stressed but not broken.

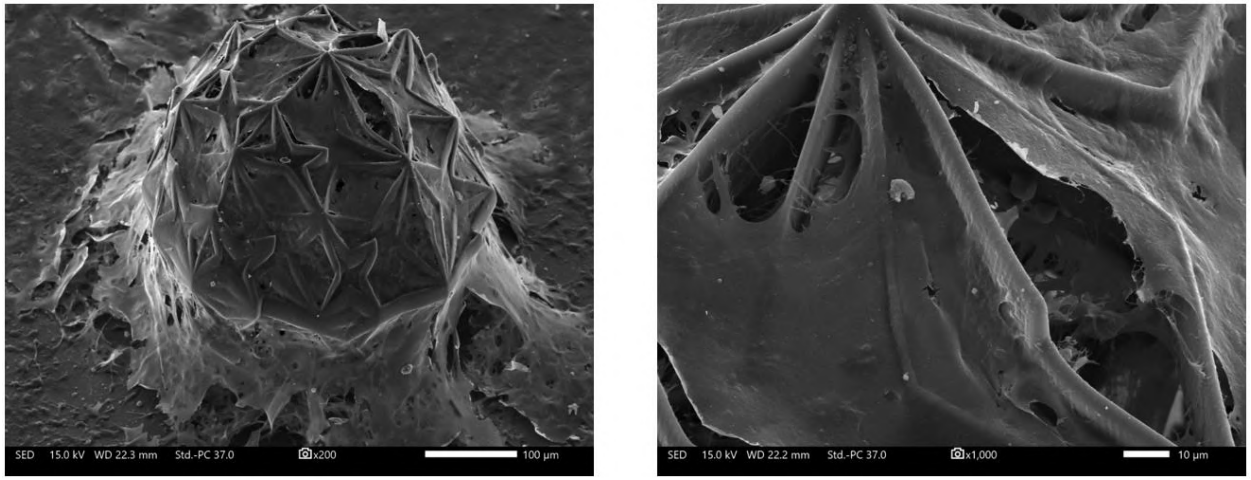

Figure 103: Tilted view of Shuriken at 7 days of culture.

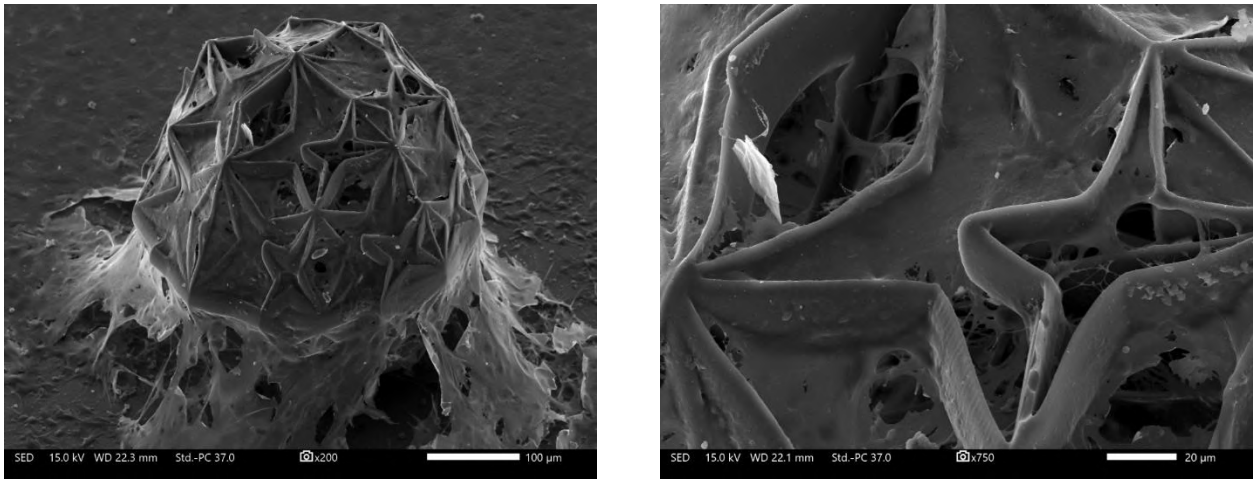

Figure 104: Tilted view of Shuriken at 7 days of culture from the other side.

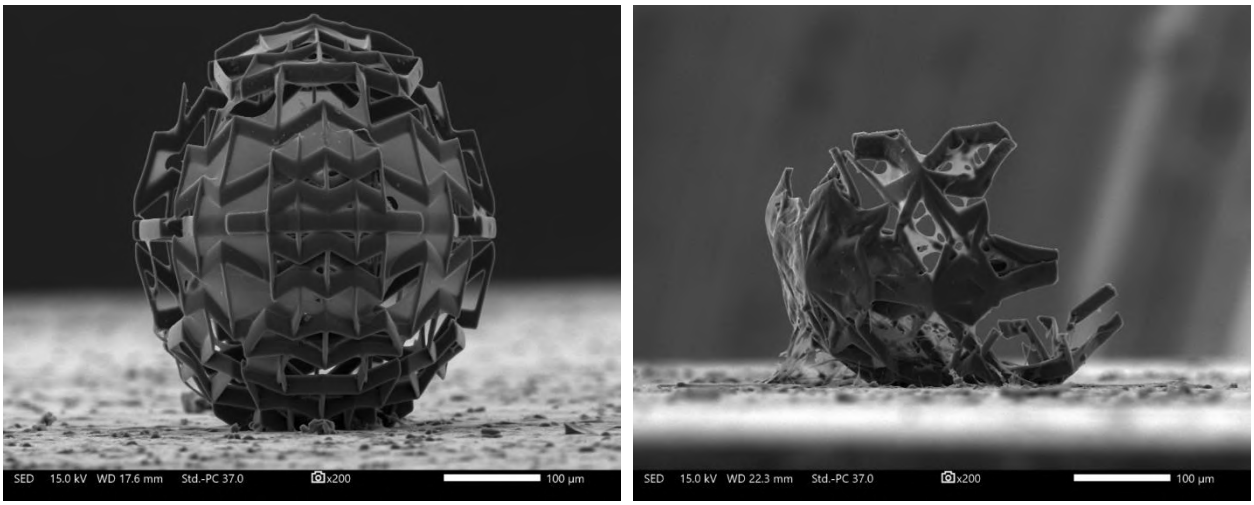

Figure 105: Side view at 3 days of culture. Left is the Bowtie and right is the Shuriken.

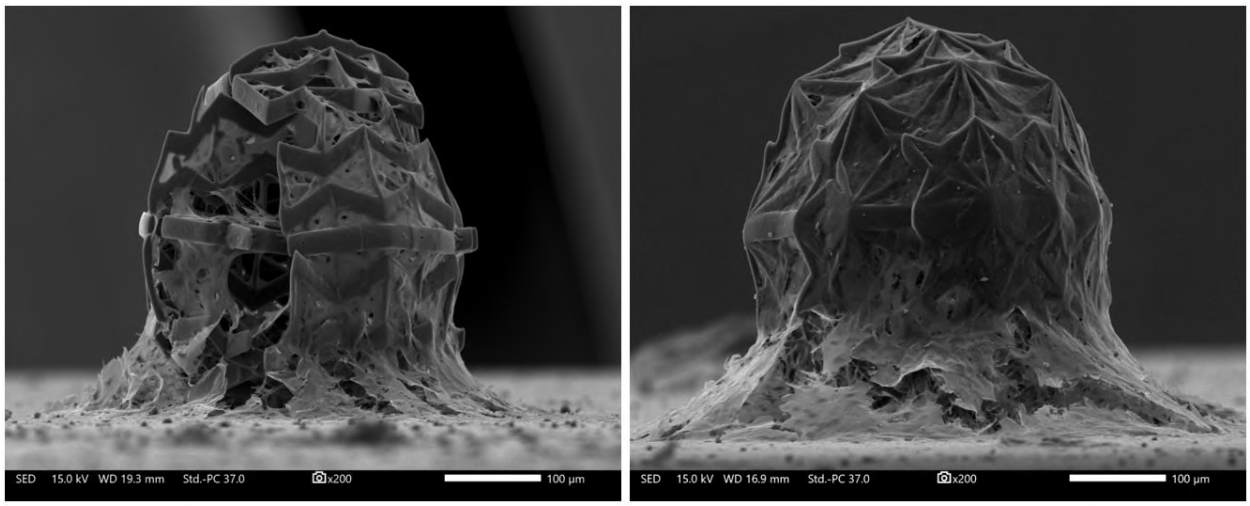

Figure 106: Side view at 5 days of culture. Left is the Bowtie and right is the Shuriken.

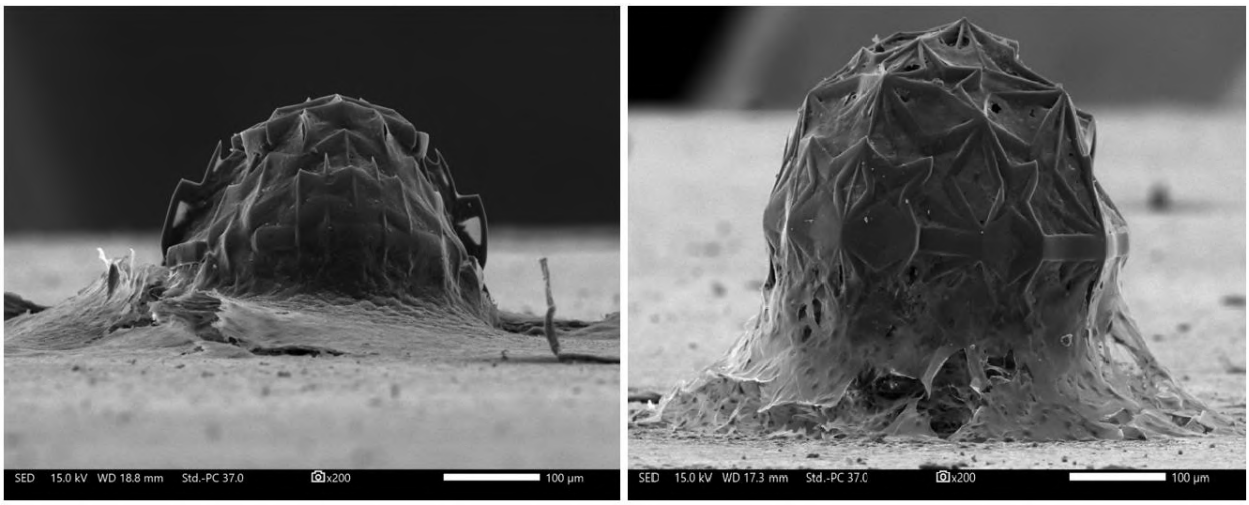

Figure 107: Side view at 7 days of culture. Left is the Bowtie and right is the Shuriken.